ASTROPHYSICAL SIMULATIONS OF HIGH VELOCITY CLOUDS, DARK MATTER MINIHALOS, AND NON-EQUILIBRIUM COOLING

by

ERIC HENRY GOETZ

(Under the Direction of Robin Shelton)

High velocity clouds (HVCs) are clouds of gas moving at high relative speeds through galaxies, including our own. They play an important role in the evolution of the galaxies with which they interact. This work explores several important topics related to HVCs. We determine how mixing between an HVC and the ambient environment affects the HVC's distribution of ionization states. We then use those results to develop a new prescription for estimating the mass of HVCs from observables. We also perform hydrodynamic and magnetohydrodynamic simulations of HVCs colliding with the Galactic disk, to analyze the survivability of such a collision for the HVC and the effects of the collision on the disk. The HVCs in these simulations are modeled by a dark matter minihalo, with most of the clouds also including a baryonic component. We also develop a new algorithm for calculating the radiative losses due to the actual populations of ions present in the gas, rather than using the typical approximation that the ions are in collisional ionization equilibrium (CIE). We test our algorithm against two CIE radiative cooling algorithms, one developed here which uses the same elements as our NEI algorithm, and the other the existing FLASH radiative cooling module which includes contributions from a larger number of elements. Finally, we apply our new radiative cooling algorithm to simulations of HVCs.

INDEX WORDS: High-velocity clouds, Hydrodynamic simulations, Dark Matter,

Magnetohydrodynamic simulations, Intergalactic Clouds

Astrophysical Simulations of High Velocity Clouds, Dark Matter Minihalos, and Non-Equilibrium Cooling

by

ERIC HENRY GOETZ

B.S., University of Richmond, 2019

A Dissertation Submitted to the Graduate Faculty of the University of Georgia in Partial Fulfillment of the Requirements for the Degree.

Doctor of Philosophy

ATHENS, GEORGIA

©2025

Eric Henry Goetz

All Rights Reserved

Astrophysical Simulations of High Velocity Clouds, Dark Matter Minihalos, and Non-Equilibrium Cooling

by

ERIC HENRY GOETZ

Major Professor: Robin Shelton

Committee: Phillip Stancil

Loris Magnani

Electronic Version Approved:

Ron Walcott

Dean of the Graduate School

The University of Georgia

May 2025

DEDICATION

This dissertation is dedicated to my family and friends. This would not have been possible without your support.

ACKNOWLEDGMENTS

I would like to thank all of the people who have been involved in the work presented here. Primarily, I would like to thank Dr. Robin Shelton for her support and invaluable guidance during my time at the University of Georgia. I would also like to thank the other members of my committee, Dr. Phillip Stancil and Dr. Loris Magnani, for their support.

I would like to thank Chen Wang for his help and great discussions. I would also like to acknowledge Sydney Whilden for our interesting discussions regarding our first project. I would like to thank M. Elliott Williams for his help with running some of the simulations presented here and Ashton Rutkowski for her help with running some of the analysis.

I would like to thank Dr. Shan-ho Tsai for her help with utilizing the GACRC computing cluster.

The FLASH software used in this work was developed in part by the DOE NNSA and DOE Office of Science supported Flash Center for Computational Science at the University of Chicago and the University of Rochester.

Finally, I am grateful to the University of Georgia graduate school and physics department for providing funding to present the work described here at numerous conferences.

Contents

A	cknow	vledgments	v
Li	st of l	Figures	vii
Li	st of	Tables	xvi
I	Intr	oduction	1
2	The	Observed O VIis Just the Tip of the Iceberg: Estimating the Hidden Material in	l
	Circ	rumgalactic and Intergalactic Clouds	7
	2. I	Introduction	9
	2.2	Methods	11
	2.3	Results	15
	2.4	Discussion	26
	2.5	Author Contributions	31
3	Coll	isions Between Dark Matter Confined High Velocity Clouds and Magnetized Galactic	;
	Disk	xs: The Smith Cloud	32
	3. I	Introduction	34
	3.2	Simulations	37
	3.3	Results	41
	3.4	Discussion	56

Bi	bliog	raphy	II2					
5	Conclusion							
	4.5	Author Contributions	108					
	4.4	Discussion	106					
	4.3	Results	69					
	4.2	Methods	66					
	4. I	Introduction	64					
4	Cooling in Non-Collisional Equilibrium Environments							
	3.5	Author Contributions	61					

LIST OF FIGURES

2.I	Hydrogen number density plots for Run 1 at 5 epochs (0, 50, 100, 150, and 200 Myr).	
	The ambient gas moves to the right, interacting with the cloud gas. The resulting tail	
	formation and hydrodynamic instabilities are apparent in this figure	16
2.2	Hydrogen number density plots for Run 1 at 5 epochs (0, 50, 100, 150, and 200 Myr) for	
	material whose velocity in the \hat{z} direction differs by more than 100 km s $^{-1}$ from that of	
	the ambient material. At late times, part of the cloud's tail has slowed too much to be	
	considered part of the cloud. This can be seen by comparing Figure 2.2 with Figure 2.1.	17
2.3	The $f_{ m OVI}$ and temperature are plotted with a blue dot for every sight line through the	
	cloud. The sight lines are oriented parallel to the \boldsymbol{x} axis and the temperature is the mass-	
	weighted average temperature along the line of sight. The plot was made from Run 1	
	at 100 Myr. Only the material that met the cloud's velocity criterion was used to make	
	these plots. For comparison, the $f_{ m OVI}$ vs T curve for static gas is plotted in red. It was	
	calculated from Chianti (Dere et al., 1997; Del Zanna et al., 2021). O VIis confined to a	
	narrower range of temperatures in the static curve than in our simulations, which include	
	dynamic mixing of warm and hot gas	18
2.4	Plot of the cloud-averaged $f_{ m OVI}$ for each simulation as a function of time. Generally,	
	$f_{ m OVI}$ increases with time as the cloud mixes with the ambient material	19
2.5	Plots of H I/O VIfor each simulation as a function of time. Generally, H I/O VIdecreases	
	with time as hydrogen is ionized and $f_{ m OVI}$ increases (see Figure 2.4). Also shown is the	
	average observed H I/O VI ratios for the MS (Fox et al., 2010)	20

2.6	Plot of $f_{ m OVI}$ for Run 1 for a variety of cloud and ambient metallicities. Changing the	
	ambient metallicity has little effect on the curve. Changing the cloud metallicity has a	
	more noticeable but still insignificant effect	26
2.7	Plots of H I/O VIfor Run 1 for a variety of cloud and ambient metallicities. As for	
	$f_{ m OVI}$, changing the ambient metallicity has little effect on the curve. Changing the cloud	
	metallicity has a more noticeable, but still small effect.	27
2.8	$f_{ m OVI}$ vs H I/O VIratio for the cloud material at each epoch of the simulations. Differ-	
	ent colors represent different simulations. A non-linear fit of the form $Ae^{-bx}+C$ was	
	performed for each simulation, where x = H I/O VI $\times 10^{-5}$, and the best fit values for	
	A, b, and C were averaged. The curve with those values (i.e., $0.03e^{-0.17x} + 0.007$) is	
	plotted with a black solid line. The shaded region depicts the 1 sigma uncertainty on the	
	fit parameters. This empirical relationship between f_{OVI} and H I/O VIcan be used to	
	estimate a reasonable value of f_{OVI} from an observed H I/O VIratio. Our plot extends	
	past the typical range of observed H I/O VIvalues, into a region where the fit slightly	
	diverges from the simulation results	30
3.1	Hydrogen number densities for Run Mo at 4 epochs (35, 40, 45, and 50 Myr) along a	
	vertical slice in the $x=0$ plane through the central portion of the domain. The white	
	imes and black circle represent the center of mass and half-mass radius of the dark matter	
	minihalo, respectively. The contours depict the magnetic field strength. This figure	
	shows that the dark matter minihalo does not accrete gas during its passage through the	
	disk	4 I
3.2	Hydrogen number densities for Run M5 at 4 epochs (0, 30, 50, and 70 Myr) along a	
	vertical slice in the $x=0$ plane. The white \times and black circle represent the center of	
	mass and half-mass radius of the dark matter minihalo, respectively. The contours depict	
	the magnetic field strength.	42

3.3	Top panel: Physical distance between dark matter minihalo center of mass and cloud	
	center of mass as a function of time. Second panel: Total mass of the cloud material	
	moving with the dark matter minihalo, based on the criteria set forth in Section 4.2.	
	Henceforth, this material is referred to as the cloud. Third panel: Metallicity of the	
	cloud. Fourth panel: Temperature of the cloud. Fifth panel: Bulk velocity of the cloud.	
	The orange curve shows the velocity of the dark matter minihalo	43
3.4	Average metallicity of the gas found within 100 pc of the dark matter minihalo center of	
	mass	47
3.5	Plots of physical characteristics at 50 Myr for Run R5. The first four plots show hydrogen	
	number density, temperature, metallicity, and \hat{z} velocity along a vertical slice in the $x=0$	
	plane. The last two plots show the hydrogen column density and C IV column density	48
3.6	Hydrogen number density and temperature along a vertical slice in the $x=0$ plane at	
	50 Myr for Run M5. The contours depict the magnetic field strength. In comparison	
	with Figure 3.5, Run M5 creates slightly smaller and warmer bubbles	49
3.7	Clockwise from the upper left, the plots show the average hydrogen number density,	
	metallicity, temperature, and velocity in the \hat{z} direction as functions of z at 30 Myr. The	
	cloud is still ~ 2.5 kpc above the disk and will collide at 37 Myr	50
3.8	Same as Figure 3.7, but for 50 Myr.	51
3.9	Same as Figure 3.7, but for 70 Myr	52
3.10	Disk hydrogen column densities for Run M5 from a face on view of the disk at 40, 50,	
	and 70 Myr. The halo and cloud material are not shown in these panels. The first panel	
	is shortly after the cloud hit the disk (which occurred at 37 Myr) and the hole was formed.	
	The later panels show that the hole in the disk decreases in size as time goes by	53
3.II	Same as Figure 3.10 but for Run R5	54

3.12	Hydrogen column density along vertical sight lines through the disk at $y=0~{ m kpc}$ and	
	various values of x are shown for Runs Lo, Mo-M5, and R1-R5 at 40 Myr. The holes	
	in Runs M1-M5 and R1-R5 can be identified by the precipitous drop in column density	
	near $x=0\mathrm{kpc}$. Their sizes depend on both the density of the cloud and the presence of	
	a magnetic field. The dark matter minihalos in Runs Lo and Mo pull disk gas inwards,	
	creating the pileups of disk gas at $x=0\mathrm{kpc}$. These runs only contain dark matter clouds,	
	which our simulations find incapable of creating holes	55
3.13	Same as Figure 3.12 but for 50 Myr	55
3.14	Same as Figure 3.12 but at 70 Myr. The holes still exist at 70 Myr in the higher density	
	cloud simulations, but have already healed in the lower density cloud simulations. For	
	runs Lo and Mo, the pileup of disk gas at the center of the disk grows over time, creating	
	the large peaks.	56
4. I	Cooling curves for our CIE cooling model and the default FLASH cooling model from	
	Sutherland & Dopita (1993). The black curve is from Sutherland & Dopita (1993) and	
	includes contributions from both H and He. The blue and green curves are the contri-	
	butions to our CIE cooling curve from H IIand all ions of He, respectively. The red line	
	is the combination of the CIE H and He curves.	70
4.2	Cooling curves for the individual species in our H and He simulations. These are used in	
	our NEI cooling algorithm. Each curve is multiplied by the electron number density and	
	the corresponding ion's number density to get the cooling rate per volume associated	
	with that ion	71
4.3	Gas temperature as a function of time for the three different cooling models. At early	
	times, the curves overlap. As time evolves and the gas becomes more out of equilibrium,	
	the curves begin to diverge.	72

4.4	Cooling rates per volume for hydrogen and helium in our CIE radiative cooling model	
	for the simulation with an initial temperature of 2×10^5 K. At each epoch, we use the	
	temperature of the gas to select the correct cooling coefficients from the cooling curves	
	shown in Figure 4.1. We then multiply by the electron number density, hydrogen number	
	density, and the element's solar abundance to get the cooling rate per volume shown here.	73
4.5	Cooling rates per volume for hydrogen and all ions of helium, calculated from our NEI	
	radiative cooling model for the simulation with an initial temperature of 2×10^5 K. At	
	each epoch, we use the temperature of the gas to select the correct cooling coefficients	
	from the cooling curves shown in Figure 4.2. We then multiply by the electron number	
	density and the ion's number density to get the cooling rate per volume shown here	74
4.6	Same as Figure 4.3, but for the simulation with an initial gas temperature of 2×10^6 K.	75
4.7	Same as Figure 4.4, but for the simulation with an initial gas temperature of 2×10^6 K.	76
4.8	Same as Figure 4.5, but for the simulation with an initial gas temperature of 2×10^6 K.	77
4.9	Same as Figure 4.3, but with an initial gas temperature of 2×10^4 K	78
4.10	Same as Figure 4.4, but for the simulation with an initial gas temperature of 2×10^4 K.	79
4. II	Same as Figure 4.5, but for a simulation with an initial gas temperature of $2\times10^4~\mathrm{K}.$.	80
4.12	Cooling curves for our CIE cooling model and the default FLASH cooling model from	
	Sutherland & Dopita (1993). The black curve is from Sutherland & Dopita (1993) and	
	includes contributions from H, He, and 14 other elements. The dark and light blue	
	curves are the contributions to our CIE cooling curve from H IIand all ions of He,	
	respectively. The yellow line is the contribution to the CIE cooling curve from all ions	
	of O. The maroon line is the combination of the CIE H, He, and O curves	80
4.13	Cooling curves for some the individual species in our H, He, and O simulations. We	
	combine the cooling curves for the three helium ions into one curve (shown in blue).	
	The individual cooling curves for each of the oxygen ions are included. These curves are	
	used in our NEI cooling algorithm.	81

4.I4	Same as Figure 4.3, but our CIE and NEI models shown here include H, He, and O. The	
	Sutherland & Dopita (1993) model used here includes contributions from 16 elements	82
4.15	Same as Figure 4.4, but for a simulation with H, He, and O	82
4.16	Same as Figure 4.5, but for a simulation with H, He, and O. The curves for O VIIIand	
	O IXare not shown here because they are too low.	83
4.17	Same as Figure 4.14, but for a simulation with an initial temperature of 2×10^6 K	84
4.18	Same as Figure 4.15, but for a simulation with an initial temperature of $2\times 10^6~{\rm K.}$	84
4.19	Same as Figure 4.16, but for a simulation with an initial temperature of 2×10^6 K	89
4.20	Same as Figure 4.14, but for a simulation with an initial temperature of 2×10^4 K	89
4.21	Same as Figure 4.15, but for a simulation with an initial temperature of $2\times 10^4~{\rm K.}$	86
4.22	Same as Figure 4.16, but for a simulation with an initial temperature of 2×10^4 K. The	
	curves for oxygen ions above O IIIare not shown here because they are too small to fit	
	on the plot.	86
4.23	Cooling curves for our CIE cooling model and the default FLASH cooling model from	
	Sutherland & Dopita (1993). The black curve is from Sutherland & Dopita (1993) and	
	includes contributions from H, He, and 14 other elements. The dark and light blue	
	curves are the contributions to our CIE cooling curve from H IIand all ions of He,	
	respectively. The green and orange lines are the contribution to the CIE cooling curve	
	from all ions of C and O, respectively. The maroon line is the combination of the CIE	
	H, He, C, and O curves	87
4.24	Cooling curves for the individual species in our H, He, C, and O simulations. To high-	
	light the effect of the carbon ions, we combine the individual cooling curves for the three	
	helium ions and the nine oxygen ions. These curves are shown in different shades of blue.	
	These curves are used in our NEI cooling algorithm.	88
4.25	Same as Figure 4.3, but our CIE and NEI models shown here include H, He, C and O.	
	The Sutherland & Dopita (1993) model is the same as in Figure 4.14	88
126	Same as Figure 4.4, but for a simulation with H. He. C. and O.	80

4.27	Same as Figure 4.5, but for a simulation with H, He, C, and O. The curve for C VIIIs	
	not shown here because it is too low.	89
4.28	Same as Figure 4.25, but for a simulation with an initial temperature of 2×10^6 K	90
4.29	Same as Figure 4.26, but for a simulation with an initial temperature of $2\times 10^6~{\rm K.}$	91
4.30	Same as Figure 4.27, but for a simulation with an initial temperature of 2×10^6 K. The	
	cooling rates for C Iand C IIare not shown here because their values are too small	91
4.31	Same as Figure 4.25, but for a simulation with an initial temperature of 2×10^4 K	92
4.32	Same as Figure 4.26, but for a simulation with an initial temperature of $2\times 10^4~{\rm K.}$ $\;$	92
4.33	Same as Figure 4.27, but for a simulation with an initial temperature of 2×10^4 K. The	
	curves for carbon ions above C IIIare not shown here because they are too small to fit	
	on the plot.	93
4.34	Cooling curves for our CIE cooling model and the default FLASH cooling model from	
	Sutherland & Dopita (1993). The black curve is from Sutherland & Dopita (1993) and	
	includes contributions from H, He, and 14 other elements. The dark blue and blue curves	
	are the contributions to our CIE cooling curve from H IIand all ions of He, respectively.	
	The aqua, green, and orange lines are the contribution to the CIE cooling curve from all	
	ions of C, O, and Ne, respectively. The maroon line is the combination of the CIE H,	
	He, C, O, and Ne curves.	93
4.35	Cooling curves for the individual species in our H, He, C, O, and Ne simulations. We	
	combine the contributions of the individual ions for He, C, and O. These curves are	
	shown in different shades of blue. These curves are used in our NEI cooling algorithm.	94
4.36	Same as Figure 4.3, but our CIE and NEI models shown here include H, He, C, O, and	
	Ne. The Sutherland & Dopita (1993) model is the same as in Figure 4.14	94
4.37	Same as Figure 4.4, but for a simulation with H, He, C, O, and Ne	95
4.38	Same as Figure 4.5, but for a simulation with H, He, C, O, and Ne. The curves for Ne IX,	
	Ne X, and Ne XIare not shown here because they are too low	95
4.39	Same as Figure 4.36, but for a simulation with an initial temperature of 2×10^6 K	96

4.40	Same as Figure 4.37, but for a simulation with an initial temperature of $2\times 10^6~{\rm K}.$	96
4.4I	Same as Figure 4.38, but for a simulation with an initial temperature of 2×10^6 K. The	
	cooling rates for Ne Ithrough Ne IVare not shown here because their values are too small.	97
4.42	Same as Figure 4.36, but for a simulation with an initial temperature of 2×10^4 K	97
4.43	Same as Figure 4.37, but for a simulation with an initial temperature of 2×10^4 K	98
4.44	Same as Figure 4.38, but for a simulation with an initial temperature of 2×10^4 K. The	
	curves for neon ions above Ne IIIare not shown here because they are too small to fit on	
	the plot	98
4.45	Cooling curves for our CIE cooling model and the default FLASH cooling model from	
	Sutherland & Dopita (1993). The black curve is from Sutherland & Dopita (1993) and	
	includes contributions from H, He, and 14 other elements. The dark blue and blue curves	
	are the contributions to our CIE cooling curve from H IIand all ions of He, respectively.	
	The aqua, green, yellow, and red lines are the contribution to the CIE cooling curve from	
	all ions of C, N, O, and Ne, respectively. The maroon line is the combination of the CIE	
	H, He, C, N, O, and Ne curves	99
4.46	Cooling curves for the individual species in our H, He, C, N, O, and Ne simulations. We	
	combine the contributions of the individual ions for He, C, O, and Ne. These curves	
	are shown in different shades of blue. These curves are used in our NEI cooling algorithm.	99
4.47	Same as Figure 4.3, but our CIE and NEI models shown here include H, He, C, N, O,	
	and Ne. The Sutherland & Dopita (1993) model is the same as in Figure 4.14	100
4.48	Same as Figure 4.4, but for a simulation with H, He, C, N, O, and Ne	00
4.49	Same as Figure 4.5, but for a simulation with H, He, C, N, O, and Ne. The curves for	
	N VIIand N VIIIare not shown here because they are too low	IOI
4.50	Same as Figure 4.6, but our CIE and NEI models shown here include H, He, C, N, O,	
	and Ne. The Sutherland & Dopita (1993) model is the same as in Figure 4.14	IOI
4.5I	Same as Figure 4.7, but for a simulation with H, He, C, N, O, and Ne	102

4.52	Same as Figure 4.8, but for a simulation with H, He, C, N, O, and Ne. The curves for	
	N Iand N IIare not shown here because they are too low	102
4.53	Same as Figure 4.9, but our CIE and NEI models shown here include H, He, C, N, O,	
	and Ne. The Sutherland & Dopita (1993) model is the same as in Figure 4.14	103
4.54	Same as Figure 4.10, but for a simulation with H, He, C, N, O, and Ne	103
4.55	Same as Figure 4.11, but for a simulation with H, He, C, N, O, and Ne. The curves for	
	nitrogen ions above N IIIare not shown here because they are too low	104
4.56	Mass-weighted average temperature of the material that is considered to be a part of the	
	HVC, based on the velocity cut described in Section 4.2.2	104
4.57	Average log O VIionization fraction as a function of time for both simulations	109
4.58	Log of the ratio of H Ito O VIas a function of time for both simulations	106

LIST OF TABLES

2.I	Simulation Parameters	13
2.2	$f_{ m OVI}$	20
2.3	Magellanic Stream Log Column Densities	24
3 . I	Simulation Parameters. Note that initial cloud density, presence of the Galactic mag-	
	netic field, and minimum cell size vary between the runs. Table 3.2 shows the chosen	
	parameters for individual simulations	40
3.2	Set of Simulations.	40
3.3	Fate of the progenitor cloud. The second column is the ratio of surviving progenitor	
	cloud mass in the post-collision cloud to the original progenitor cloud mass. The third	
	column is the ratio of accreted material to surviving progenitor material in the post-	
	collision cloud. The fourth column is the ratio of post-collision cloud mass to original	
	progenitor cloud mass. The tabulated results are for 50 Myr	46
3.4	Same as Table 3.3 but for 70 Myr	46
3.5	Dimensions and area of the holes formed for each run. Blank rows signify epochs where	
	a hole was not present. Dimensions are given as the maximum extent of the hole in each	
	direction	57

CHAPTERI

Introduction

Clouds of gas exist in a wide range of environments throughout the Universe, from nebulae in the interstellar medium to O VI absorbers in the intergalactic medium. One particular type of gas cloud that has important effects on galaxy evolution, star formation, and other astrophysical processes is the high velocity cloud (HVC). HVCs are clouds of gas in the Galactic halo that move at a high speed relative to the local standard of rest (LSR) - the velocity of the material around the Sun as it orbits the center of the Milky Way.

There are several different criteria that have been used to distinguish HVCs from other clouds moving at slower speeds relative to the LSR, namely that $|v_{LSR}| \ge 70 \text{ km s}^{-1}$ (Oort, 1966). As the study of HVCs has evolved, the definition has shifted to $|v_{LSR}| \ge 90 \text{ km s}^{-1}$ (Wakker & van Woerden, 1997) or $|v_{LSR}| \ge 100 \text{ km s}^{-1}$ (Richter, 2017), to distinguish HVCs from intermediate velocity clouds (IVCs).

HVCs were first observed in 1963 with the Dwingeloo radio telescope (Muller et al., 1963). They detected high velocity gas along four sight lines. Since then, there have been detections of HVCs across the entire sky (Wakker et al., 2003; Putman et al., 2012). High velocity H I has a covering fraction of 37% (Putman et al. (2012) and references therein). High velocity O VI covers an even larger fraction of the sky -60% to 85% (Sembach et al., 2003).

HVCs are multi-phase structures. They can contain both neutral gas such as neutral hydrogen (H I) and oxygen (O I) and ionized gas at a range of ionization levels, from C II (singly ionized carbon, or

C⁺¹) and O III to Si IV and O VI. O VI is a particularly important ion for the study of HVCs. This is because of oxygen's high abundance, as well as because it has a large oscillator strength, making for easier observations (Morton, 1991). As a result, O VI is commonly observed in HVCs.

Because they contain neutral material, HVCs are often thought of as a cold ($T=10^{2-3}$ K), dense core of mostly neutral gas surrounded by a warm ($T=10^{4-5}$ K) halo with ionized gas. HVCs can also contain molecules, although detections are rare. Molecular hydrogen has been detected in the Magellanic Stream, an HVC containing gas stripped off of two dwarf galaxies, the Large Magellanic Cloud and Small Magellanic Cloud (Sembach et al., 2001). Recent observations of another well-known HVC, Complex C, revealed low abundances of several elements (Fe, Al, and Si) (Fox et al., 2023). This may be evidence of dust, since those elements would have been depleted into dust.

The metallicity of HVCs varies from cloud to cloud, and even within a single cloud (Sembach et al., 2003; Fox et al., 2013b). The metallicity is defined as the ratio of the abundance of an element to the abundance of hydrogen. It is often measured relative to the solar value. Most HVCs are subsolar, with metallicities ranging from 10-30% of solar metallicity (Sembach et al., 2003; Fox et al., 2010, 2013a; Howk et al., 2017). However, some observations have identified sight lines with potentially super-solar metallicities (Yao et al., 2011). The most abundant metal in HVCs is oxygen.

Some HVCs move through the halo of our Galaxy (and other galaxies). Our Galactic halo is the gas that extends beyond the disk. It contains hot, low-density gas and is traced primarily by high ions such as O VII and O VIII, suggesting a temperature of $\sim 1-2\times 10^6 {\rm K}$ (Henley et al., 2010; Miller & Bregman, 2013). The metallicity of the halo has been measured in a variety of ways, resulting in values ranging from 0.3 to 0.7 solar. These measurements were done with O VII and O VIII emission lines (Miller & Bregman, 2015), O VII absorption lines and pulsar dispersion measures (Miller et al., 2016), and simulations (Henley et al., 2017). The density of the halo is not uniform, but is mostly between 10^{-4} and 10^{-3} cm⁻³ (Bregman & Lloyd-Davies, 2007; Gaensler et al., 2008).

Because HVCs move at high speed through a medium with different density, temperature, and metallicity, there are interesting hydrodynamic effects that occur. As the clouds move, some material is ablated. This causes deformations in the cloud, causing it spread out. Eventually, some cloud material will slow

down and be separated from the cloud. There can also be Rayleigh-Taylor and Kelvin-Helmholtz instabilities. Rayleigh-Taylor instabilities occur when two fluids with different densities are accelerated into each other (Drazin, 2002). In this case, the acceleration is due to ram pressure. These instabilities can occur at the head of the cloud as it moves through the halo. Kelvin-Helmholtz instabilities occur when there is a velocity shear at the interface between two fluids. These occur at the boundaries of the cloud (Drazin, 2002). The hydrodynamic instabilities that form during the cloud's motion have important consequences for the evolution of the cloud. These features can strip material from the cloud, as well as entrain halo gas into the cloud. This mixing between the cloud and halo gas provides a mechanism for hot, highly ionized gas to become a part of the HVC. Once the hot gas joins the cloud, the hot gas cools, and the high ions begin to recombine. Through this process, HVCs can contain ions at a wide range of ionization states.

The dynamic mixing between an HVC and the halo and the hydrodynamic instabilities present in the HVC indicate that HVCs are likely out of collisional ionization equilibrium (CIE). Collisional ionization is a process in which an atom collides with another particle (atom or electron) and loses an electron. The reverse process is recombination, in which an ion gains a free electron. In CIE, the collisional ionization and recombination rates for each ion are balanced, resulting in stable ionization fractions - the fraction of an element's atoms that are in a particular ionization state. However, in the case of HVCs, this approximation does not accurately reflect their dynamic nature. As a result, non-equilibrium ionization (NEI) calculations provide a more accurate picture of the ionization fractions of HVCs. Chen Wang, Robin Shelton, and I discussed the effects of NEI calculations and hydrodynamic mixing on the ionization fraction of O VI in HVCs and the temperature at which O VI is found in Goetz et al. (2024). We found that O VI is found at a wide range of temperatures, which is much different than what is expected from a static CIE model (see also Wang et al. (2025, submitted to ApJ)). I explain the results in Chapter 2.

The ionization fraction of certain ions, such as O VI, is important for the study of HVCs because it is often used to calculate the mass of HVCs. Ionized hydrogen is often difficult to observe directly, so instead, observations of metal ions can be used. By taking a column density of a metal ion such as O VI and dividing it by that ion's ionization fraction and the metallicity, a column density of hydrogen can be found. Dividing an ion's column density by the ionization fraction results in the column density for

that element, since the ionization fraction is the fraction of that element in that particular ionization state. Then, dividing an element's column density by the metallicity results in a hydrogen column density. Historically, papers using this method have assumed that because O VI is highly ionized, the associated hydrogen is ionized and hot (Sembach et al., 2003; Fox et al., 2010). So, to get the total cloud mass, the observed neutral hydrogen column density would be added to the calculated ionized hydrogen density. If other ions are observed for a particular sight line, this same procedure can be done for those, and the results added to the total column density for that sight line (Fox et al., 2010).

An issue with this method is that the ionization fractions used for these calculations are often the maximum value from a CIE model. That assumes that all of the O VI rich gas has the same temperature. In reality, there is a range of temperatures in the cloud. In addition, because of their dynamic nature, HVCs are not in CIE. As a result, using ionization fraction values from CIE models does not accurately reflect the true nature of HVCs. In Goetz et al. (2024), we explored the impact of using a more accurate ionization fraction on existing estimates of HVC masses. We also provided a new interpretation of the method for calculating the total mass of HVCs discussed above. Finally, we provided a prescription for use of our ionization fractions based on quantities an observer would obtain.

We performed these analyses (and the others discussed later) using the FLASH hydrodynamics simulation code (Fryxell et al., 2000). FLASH is an Eulerian grid-based code, meaning the grid is fixed and material flows through the domain, instead of the grid moving with the moving material. FLASH also incorporates adaptive mesh refinement (AMR). This allows the grid to be refined to higher levels (more cells, higher resolution) in regions of interest, while regions without much variation are kept at lower refinement levels. One of the most important features of FLASH is the non-equilibrium ionization module. This calculates the ionization levels of the different species in the simulation in a time-dependent manner. It also allows us to track the populations of each ion present in the simulation. FLASH also includes a number of other physics modules that can be used when applicable. These include radiative cooling (to be discussed at length later in this Chapter and in Chapter 4), gravity, and magnetic fields.

HVCs play an important role in the evolution of galaxies. HVCs are a source of fresh material that can be used for star formation. This supply of material is critical in keeping the star formation rate of the

Galaxy at approximately 1-2 M_{\odot} yr⁻¹ (Robitaille & Whitney, 2010; Chomiuk & Povich, 2011; Putman et al., 2012). Additionally, HVCs can collide with the Galactic disk. This collision can trigger star formation (Comeron & Torra, 1994; Alig et al., 2018; Bekki & Chiba, 2006), as well as create shells of gas emanating from the disk (Mirabel, 1982; Heiles, 1984; Vorobyov & Basu, 2005; Galyardt & Shelton, 2016) and holes in the disk itself (Mirabel, 1982; Bekki & Chiba, 2006; Kannan et al., 2012; Galyardt & Shelton, 2016; Shah et al., 2019). An important question regards the survivability of the collision for an HVC. Robin Shelton, Jason Galyardt, and I explored this topic in Shelton et al. (2024). We also determined characteristics of the holes and shells that are formed by the collision. This work is reproduced in Chapter 3.

An important physical process that occurs in HVCs (and many other astrophysical objects) is radiative cooling. This is a process by which an object loses heat through the emission of radiation. There are several different processes by which this occurs. Four are discussed here. The first is radiative recombination (free-bound emission), which is when an ion captures a free electron. This process releases a photon. The second process is bremsstrahlung (free-free emission). In this case, a free electron is decelerated by an atom. The electron loses kinetic energy, which is released as a photon. Both radiative recombination and bremsstrahlung are continuum processes, meaning the photon energy can take a broad range of values instead of discrete values. The third radiative cooling process is bound-bound emission, which occurs when an electron bound to a nucleus moves to a lower energy level, releasing a photon. The energy of the photon depends on the difference between energy levels, and so can only take discrete values. The final process discussed here is two photon emission. This is similar to bound-bound emission, but instead of emitting a single photon, the atom emits two photons. The combined energy of the two photons depends on the energy level difference, but the individual photon energies are not set. Therefore, this is also a continuum process. The strength of each of these cooling processes depends on the temperature of the gas and the specific ion.

The total cooling coefficient, or the rate at which energy is radiated, for a given species can be calculated by summing the contributions of each radiative cooling process. For computational ease, the total cooling coefficients for a set of species (assumed to be in CIE) are often summed together. Then, in a simulation, the total cooling coefficient can be taken from a look-up table based on the temperature. This is done in

FLASH and other astrophysical simulation codes. However, as discussed above, the CIE approximation is not good for HVCs. This raises the questions of whether a radiative cooling algorithm based on the actual ion populations in a simulation calculated using NEI methods would result in different amounts of cooling, and if so, whether that would have an impact on the results of the simulation. I discuss this in Chapter 4.

CHAPTER 2

THE OBSERVED O VI IS JUST THE TIP

OF THE ICEBERG: ESTIMATING THE

HIDDEN MATERIAL IN

CIRCUMGALACTIC AND

INTERGALACTIC CLOUDS I

¹Goetz, E., Wang, C., & Shelton, R. L. 2024, ApJ, 960, 66,389 doi: 10.3847/1538-4357/adodf7390. Reproduced with permission from the Astrophysical Journal. This chapter has been modified to reflect my individual contributions.

Abstract

This paper proposes a new method for estimating the total quantity of material in moving circumgalactic and intergalactic clouds from O VI measurements. We simulate high-velocity clouds (HVCs) with the FLASH hydrodynamic code and track the ionization and recombination of all ionization levels of oxygen as a function of time. We calculate the O VI/oxygen ratio ($f_{\rm OVI}$) in our dynamic NEI clouds, finding that it differs significantly from that in static gas. We find that O VI exists in cool, medium, and hot gas in the clouds. As such, it traces all of the hydrogen rather than merely the ionized hydrogen. The total quantity of hydrogen along a typical observed line of sight through a cloud can be estimated from the observed O VI column density, metallicity, and our f_{OVI} . We provide the simulations' f_{OVI} , a prescription for finding f_{OVI} for observed dynamic clouds, and a methodology for calculating the total hydrogen column density from this f_{OVI} and an observed O VI column density. As examples, we use our f_{OVI} to estimate the total hydrogen column densities along various observed sight lines through two HVCs, Complex C and the Magellanic Stream, finding that these clouds contain more material than the previous lower limits. We also extend this analysis to low-redshift intergalactic O VI clouds, finding that they contain several times more baryonic material than previously thought and therefore may account for a significant fraction of the Universe's baryons.

2.1 Introduction

High velocity clouds (HVCs) are gaseous clouds moving in and around galaxies at high speeds relative to the local standard of rest. HVCs are important because they impact the evolution of galaxies. They provide a source of material that can be used for star formation. The common criteria for distinguishing HVCs is that they have $v_{LSR} \ge 90$ or 100 km s⁻¹ Wakker & van Woerden (1997); Richter (2017).

HVCs can contain neutral material as well as ionized material in various ionization states. These states include low ions such as C II and O III and high ions such as C IV and O VI. The wide range of ionization states observed in these clouds suggests that they may be out of collisional ionization equilibrium (CIE). This is further supported by observations of absorption feature line widths. The width of an absorption feature contains information about the temperature of the gas. Many HVC absorption features of high ions have been observed to have much smaller line widths than expected from CIE models (Yao et al., 2011; Tripp, 2022). This indicates that those ions are found in cooler gas than expected.

There are several different proposed explanations for observations of cool high ions such as O VI in HVCs. One of these is photoionization. However, the ionizing photon flux experienced by HVCs at 114 eV (the ionization potential for O VI) is often thought to be too small to photoionize significant amounts of O VI (Tripp et al., 2003; Sembach et al., 2003; Ganguly et al., 2005; Fox et al., 2010). An alternative explanation comes from Kwak & Shelton (2010), who showed that the mixing between the HVC and the ambient environment can also result in high ions at temperatures lower than what would be expected from static CIE models.

O VI is an important ion in HVCs because it is commonly observed. This is due to its large oscillator strength (Morton, 1991) and the high abundance of oxygen in HVCs relative to other metals. As a result, O VI is often chosen to be a tracer of hot gas in HVCs (Sembach et al., 2003; Fox et al., 2006, 2010; Cashman et al., 2023). O VI is also important because the O VI column density can be used to approximate the hydrogen column density. However, this requires the oxygen metallicity (the ratio of oxygen to hydrogen) and the O VI ionization fraction (the fraction of oxygen in the O VI ionization state, $f_{\rm OVI}$). Static CIE and NEI ionization models predict that the highest percentage O VI is found at $\sim 10^5$ K. As a result, the

hydrogen associated with O VI has historically been considered hot (Sembach et al., 2003, 2004; Fox et al., 2010). Because of this, observers will often add the observed H I column density to the hydrogen column density calculated from O VI (Sembach et al., 2003; Fox et al., 2010). In some cases, observers will also do a similar calculation for a different ion than O VI, with the assumption that the ion traces different gas than O VI (Fox et al., 2010). It is important to note that until now, the $f_{\rm OVI}$ used in these calculations is the maximum value from static gas models such as (Sutherland & Dopita, 1993; Gnat & Sternberg, 2007). In these models, the maximum $f_{\rm OVI}$ value is ~ 0.2 , which occurs at a gas temperature of $\sim 10^{5.2}$ K. Because the maximum $f_{\rm OVI}$ was used, the resulting hydrogen column density was considered to be a lower limit. We aim to determine a more accurate $f_{\rm OVI}$ value that incorporates the dynamic value of HVCs.

In this work, we run simulations of HVCs interacting with the ambient environment, using the FLASH simulation code (Fryxell et al., 2000). FLASH is an Eulerian hydrodynamic code that has been used to simulate HVCs in a number of cases (Kwak et al., 2011; Plöckinger & Hensler, 2012; Gritton et al., 2014; Galyardt & Shelton, 2016; Gritton et al., 2017; Sander & Hensler, 2021). We run a total of ten simulations, varying the initial temperatures and densities of the HVC and ambient medium, as well as the size and velocity of the HVC. We are able to see how the HVCs evolve as they mix with the ambient environment. We are also able to track characteristics of the HVCs, such as the location and temperature of the O VI.

We find that after sufficient time has elapsed, O VI is spread throughout the HVC, overlapping with both ionized and neutral gas. Therefore, we calculate the total $f_{\rm OVI}$ of the cloud considering all of the material in the cloud. A consequence of this is that instead of O VI being associated with hot, ionized material, as had commonly been assumed, our O VI is associated with all of the material in the cloud.

We also calculate the ratio of H I to O VI. This ratio decreases over time as the neutral material initially present in the cloud ionizes and ionized ambient material is entrained in the cloud. We find a relationship between this ratio and $f_{\rm OVI}$. This relationship allows observers to determine an accurate $f_{\rm OVI}$ for a given sight line, given observations of H I and O VI.

We develop a new methodology for calculating the total column density of hydrogen, given an observation of O VI. This methodology uses our calculated average f_{OVI} .

In Section 2.2, we discuss the details of the ten simulations we ran using the FLASH code (Fryxell et al., 2000). In Section 2.3, we show the results of our ten simulations. We also introduce our new methodology for calculating the mass of HVCs. We then apply that methodology to the Magellanic Stream (MS). In Section 2.4, we introduce our prescription that observers can use to apply our methodology to their observed sight lines. We also discuss the applications of these results to intergalactic O VI absorbers.

2.2 Methods

We run our simulations with FLASH version 4.6.2 (Fryxell et al., 2000). We use FLASH's hydrodynamic and NEI modules to calculate the time-dependent ionization levels of oxygen and we use a lookup table to calculate the radiative cooling of the materials. For the latter, we use the CIE cooling curve table with [Fe/H]=-0.5 from Sutherland & Dopita (1993).

The simulations are done in 3D cartesian coordinates with adaptive mesh refinement. In each simulation, the domain is a rectangular cuboid box with dimensions of 2.4 kpc \times 1.2 kpc \times 10.8 kpc in the \hat{x} , \hat{y} , and \hat{z} directions, respectively. The domain is segmented into 18 identical square blocks in a 2 \times 1 \times 9 layout. The maximum resolution of each cell is 9.375 pc in each direction.

We run the simulations in a wind tunnel fashion, with the ambient material flowing in through the lower z boundary and out through the upper z boundary. Material can also leave the domain through the lower and upper x boundaries and upper y boundary. In order to capitalize on the assumed symmetry of the cloud, we place the center of the cloud along the lower y boundary, simulate half of the cloud inside the domain, and make the lower y boundary a reflecting boundary. The center of the cloud is initially located 1.2 kpc above the lower z boundary. This location is at (x=0 kpc, y=0 kpc, z=0 kpc) in the domain. From the perspective of the domain, the cloud is stationary at the beginning of the simulation. However, from the perspective of the ambient gas, the cloud is moving toward the $-\hat{z}$ direction with a velocity equaling the wind speed.

In this project, we use O VI as a tracer of hydrogen in highly ionized gas, so it is important to use a reasonable estimate of the oxygen metallicity in our calculations. We want to choose a metallicity that

is similar to those of our comparison clouds, the MS and Complex C. The oxygen metallicity varies throughout the MS and Complex C (Fox et al. 2013b; Sembach et al. 2003) and different observers find somewhat different values. A metallicity value of 0.1 solar was adopted for calculations by both Fox et al. (2010) for the MS and Sembach et al. (2003) for Complex C. Fox et al. (2010) used the Asplund et al. (2009) abundance table in which there are 4.89×10^{-4} oxygen atoms per hydrogen atom. Sembach et al. (2003) used the Holweger (2001) abundance table in which there are 5.45×10^{-4} oxygen atoms per hydrogen atom, but they calculate the total hydrogen mass of the cloud instead of hydrogen column densities along sight lines. To be consistent with the calculations of Fox et al. (2010), we adopt the same metallicity value and abundance table that they used. This resulting value of O/H is similar to those of Fox et al. (2013a) and Howk et al. (2017) for the MS and Collins et al. (2007) for Complex C. Although Wakker et al. (1999) and Richter et al. (2001) also found a 0.1 solar metallicity, they used the Anders & Grevesse (1989) abundance table in which there are ~ 1.6 times more oxygen atoms per hydrogen atom. Other observations of Complex C suggest a higher metallicity, up to 0.3 solar (Tripp et al., 2003; Shull et al., 2011), using Holweger (2001) and Asplund et al. (2009), respectively. Considering this, we also examine the effect of using alternate cloud metallicities.

A wide range of values for the metallicity of the ambient medium have been deduced. Miller & Bregman (2015) used O VIII emission lines to calculate a metallicity of the circumgalactic medium that was ≥ 0.3 solar assuming Anders & Grevesse (1989) abundances. Troitsky (2017) modeled the density of the circumgalactic gas, finding the best fit metallicity at a height of 10 kpc to be roughly 0.5 solar, with significant uncertainties. They appear to have relied on Miller & Bregman (2015), which uses Anders & Grevesse (1989) abundances. Miller et al. (2016) examined O VII absorption lines and pulsar dispersion measures and found the value of the halo gas metallicity to be ≥ 0.6 solar. They used Holweger (2001) abundances. Comparisons of observations of the halo with simulations suggest that the metallicity of the halo is around 0.7 solar (Henley et al., 2017). They used FLASH, which usually uses Anders & Grevesse (1989) abundances. Henley & Shelton (2015) modeled the halo's x-ray emission using solar metallicity with a variety of oxygen abundance tables and found good reduced χ^2 values for all of them. This suggests that the oxygen abundance of the halo is difficult to constrain. Considering the range of deduced metallicities,

Table 2.1: Simulation Parameters

Simulation	$n(H)_{cloud}$	$T_{\rm cloud}$	$n(H)_{ambient}$	$T_{ m ambient}$	$r_{ m cloud}$	$v_{ m inflow}$
	(cm^{-3})	(K)	(cm^{-3})	(K)	(pc)	(km s^{-1})
Run 1	0.4	5000	0.001	2×10^{6}	500	150
Run 2	0.4	5000	0.001	2×10^{6}	500	100
Run 3	0.4	5000	0.001	2×10^{6}	300	150
Run 4	0.4	5000	0.001	2×10^{6}	500	300
Run 5	0.04	5000	0.0001	2×10^{6}	500	150
Run 6	0.2	5000	0.001	1×10^{6}	500	150
Run 7	2.0	1000	0.001	2×10^{6}	500	150
Run 8	I.O	1000	0.001	1×10^{6}	500	150
Run 9	0.67	3000	0.001	2×10^{6}	500	300
Run 10	0.222	9000	0.001	2×10^6	500	150

we feel comfortable using a 0.7 solar metallicity. However, we also explore the effect of using alternate ambient metallicities.

To implement these metallicities, we conduct a two-step process. The first step is to arbitrarily set the metallicities of the cloud and ambient gas to simple values in the FLASH simulations. For convenience, we set the initial values for the cloud and ambient metallicities to 10^{-3} and 1 times the solar metallicity, respectively. The second step is to re-scale them during the post-processing to 0.1 solar for the cloud and 0.7 solar for the ambient material. As mentioned above, we also re-scale to other metallicities to explore the impact on our results. FLASH uses the abundance table of Anders & Grevesse (1989), but we re-scale during the post-processing to the abundance table of Asplund et al. (2009).

In order to explore how the cloud and ambient materials mix, cool, ionize, and recombine, we run 10 simulations with a variety of initial densities, temperatures, radii, and velocities (see Table 2.1.) Among our set of simulations, our choice of cloud hydrogen density, $n(H)_{cloud}$, ranges from 0.04 cm⁻³ to 2 cm⁻³. Our choice of cloud temperature, T_{cloud} , ranges from 1000 K to 9000 K. The ambient temperature, $T_{ambient}$, is set to 1×10^6 K or 2×10^6 K. The ambient density, $n(H)_{ambient}$, is set to 1×10^{-3} cm⁻³ or 1×10^{-4} cm⁻³. We start each simulation with the cloud in pressure equilibrium with the ambient material. This constrains the cloud density, considering the cloud temperature, ambient temperature,

and ambient density have already been specified. Our preliminary simulations and other work (Grønnow et al., 2017; Gritton et al., 2017) have shown that the initial radius of the cloud affects the cloud's evolution, mixing and ionization levels. For this reason, we run simulations with two choices of cloud radius, 300 pc and 500 pc. In order to observe how the inflow of ambient gas affects its mixing with the cloud material, we also adopt three different wind speeds, 100 km s $^{-1}$, 150 km s $^{-1}$, and 300 km s $^{-1}$. The simulations are run for 200 Myr, so each cloud has enough time to mix with the ambient gas and evolve into a more realistic shape. However, due to computational limitations, Runs 4 and 5 stopped after 185 and 128 Myr, respectively. Both simulations ran long enough for their clouds to fully evolve.

The cloud parameters given in Table 2.1 are the values at the center of the cloud. Near the outer region of the cloud, the density and temperature grade into those of the ambient material. The density follows the hyperbolic tangent function given by Gritton et al. (2014), but using a scale length of 50 pc. The temperature rises inversely with the density to preserve pressure equilibrium and mesh with the surrounding conditions. The transition between the cloud abundance and the ambient abundance occurs where the density is equal to $0.99n_{\rm ambient} + 0.01n_{\rm cloud}$. The velocity transition occurs at the same place.

At the start of the simulation, the ambient material travels at the chosen wind speed, but the cloud is at rest. As time progresses, some material is torn from the cloud while some ambient material is entrained into the cloud. In general, mixing between cloud and ambient material causes some computational cells to contain similar proportions of both cloud and ambient gas. This mixing erases the clear boundary between cloud and ambient material. Therefore, a new criterion for defining cloud material must be found, one that is both consistent with observational analyses and computationally feasible. In observations of actual clouds, the velocity contrast between the cloud and ambient gas is used to identify the cloud material. Actual HVCs are defined as clouds whose velocity differs from the local standard of rest by at least 90 or 100 km s⁻¹ (Wakker & van Woerden, 1997; Richter, 2017). We use these ideas to develop a velocity criterion for identifying the cloud. Any material in our domain whose velocity in the \hat{z} direction differs by more than 100 km s⁻¹ from that of the ambient material is considered to be part of the HVC. The ambient material speeds up slightly as the simulation progresses, which is taken into consideration in the application of the velocity criterion.

Our simulations model the mass of hydrogen and helium in the gas. Other elements make inconsequential contributions to the mass. Each simulation tracks the ionization level populations of helium and oxygen in every cell in a time-dependent manner based on the collisional ionization and recombination rates. It does not track the ionization level populations of hydrogen. Therefore, during the post-processing, we assume that the ratio of neutral hydrogen atoms to all hydrogen atoms and ions is equal to the ratio of neutral oxygen atoms to all oxygen atoms and ions. We make this assumption because their first ionization potentials are almost identical (Cox, 2000) and because there is rampant charge exchange (Field & Steigman, 1971).

In reality, HVCs are bathed in a photon field that contributes to the photoionization of each cloud. In order to estimate the extent of the photoionization, we perform Cloudy (Ferland et al., 2017) simulations during the post-processing. The photon field in the Cloudy simulations is the sum of the extragalactic background (EGB) and the radiation escaping from the Milky Way (MW). We use the HMo5 (Ferland et al., 2017) table for the EGB contribution and use the Fox et al. (2005) MW model for the MW contribution. The total ionizing flux for each contribution is taken from Fox et al. (2010). The abundance table used in our calculation (Asplund et al., 2009) is the same as that used in Fox et al. (2010). Our technique was verified by reproducing parts of Figure 5 in Fox et al. (2010), which used the same photon field model. In Cloudy, we model each cloud as a slab that has the same initial density and temperature as the cloud in the corresponding FLASH simulation. We calculate the column density of hydrogen which is photoionized by the EGB and MW photon fields. We use this column density of hydrogen in our post-processing calculations in Section 2.3.

2.3 Results

2.3.1 Simulation Results

First, we will describe the clouds' dynamics. As the simulations progress, material is ablated from the cloud. This deforms the cloud from its initial spherical shape into a more elongated structure. The ablated material forms a tail, as can be seen in Figure 2.1 for a representative simulation (Run 1 in Table

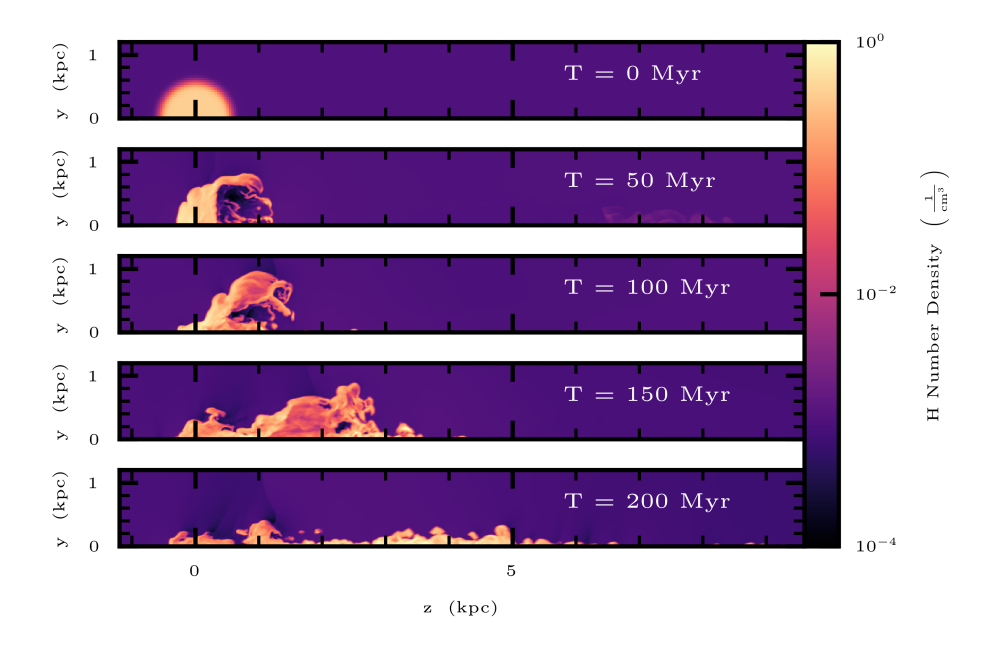


Figure 2.1: Hydrogen number density plots for Run 1 at 5 epochs (0, 50, 100, 150, and 200 Myr). The ambient gas moves to the right, interacting with the cloud gas. The resulting tail formation and hydrodynamic instabilities are apparent in this figure.

2.1). All figures and analyses were done with the YT software package (Turk et al., 2011). The interaction between the ambient gas and the tail decelerates the tail. Over time, the tail will approach the speed of the ambient gas and so will no longer meet the cloud criterion. This is shown by comparing Figure 2.1 with Figure 2.2 for which the velocity criterion has been applied to the domain.

Hydrodynamic instabilities such as the Rayleigh-Taylor and Kelvin-Helmholtz instabilities also affect the cloud. Rayleigh-Taylor instabilities are due to the head-on collisions between cloud and ambient material (Drazin, 2002). Kelvin-Helmholtz instabilities are due to the velocity shear at the boundary of the cloud and ambient material (Drazin, 2002). These instabilities tear material from the cloud and incorporate hot, ambient material into the cloud. Because the ambient material is very hot, it contains high ions of oxygen such as O VII to O IX. Once entrained in the cloud, the hot gas transfers heat to the cold gas and both components radiatively cool. Consequently, the high ions from the entrained ambient

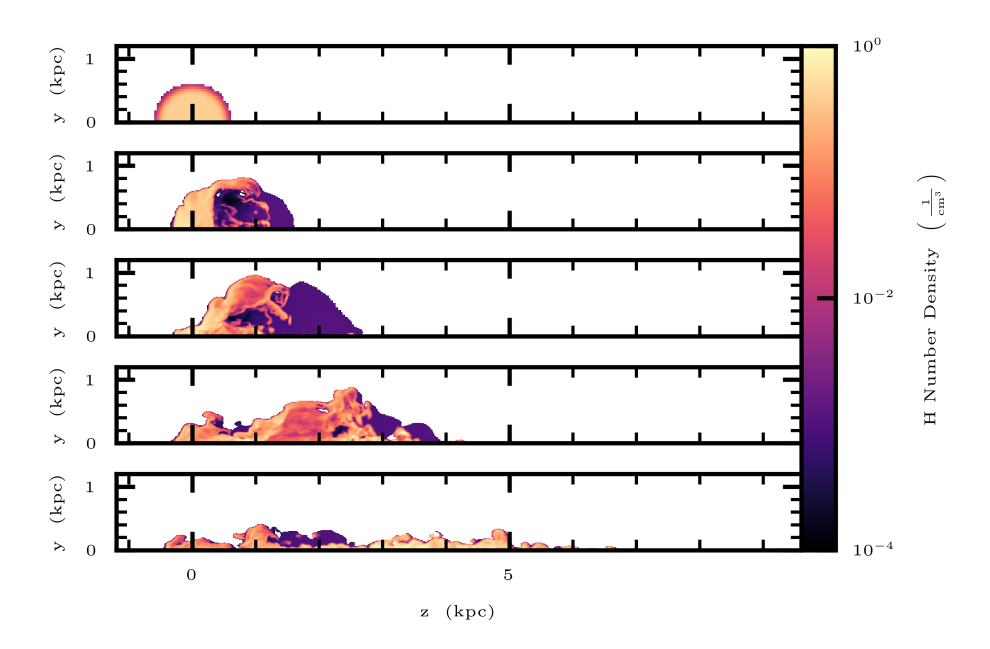


Figure 2.2: Hydrogen number density plots for Run 1 at 5 epochs (0, 50, 100, 150, and 200 Myr) for material whose velocity in the \hat{z} direction differs by more than 100 km s⁻¹ from that of the ambient material. At late times, part of the cloud's tail has slowed too much to be considered part of the cloud. This can be seen by comparing Figure 2.2 with Figure 2.1.

gas begin to recombine and the neutral and low ions in the cloud begin to ionize (Kwak & Shelton, 2010; Kwak et al., 2011).

As a result of this mixing, ionization, and recombination, O VI exists throughout the cloud and at a wide range of temperatures. Due to their dynamic nature, our set of simulations contains O VI across a wide temperature range of $\sim 2,000$ K to $\sim 2,000,000$ K. In contrast, static CIE and NEI models, such as those of Sutherland & Dopita (1993) and Gnat & Sternberg (2007), predict that O VI exists in a comparatively narrow temperature range of $\sim 150,000$ K to $\sim 1,000,000$ K.

The fact that we find O VI at a wide range of temperatures is important because it means that O VI does not solely trace hot, ionized hydrogen, but instead exists in all phases of gas. It also has implications for the calculation of the hydrogen column density, which will be discussed later in this section. Furthermore, the fraction of oxygen atoms in the O VI state, $f_{\rm OVI}$, is significant across the entire temperature range found in the cloud. Figure 2.3 shows this for a range of sight lines through the cloud. The evolution of

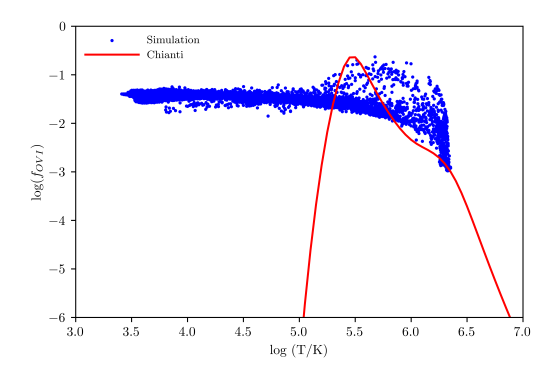


Figure 2.3: The $f_{\rm OVI}$ and temperature are plotted with a blue dot for every sight line through the cloud. The sight lines are oriented parallel to the x axis and the temperature is the mass-weighted average temperature along the line of sight. The plot was made from Run 1 at 100 Myr. Only the material that met the cloud's velocity criterion was used to make these plots. For comparison, the $f_{\rm OVI}$ vs T curve for static gas is plotted in red. It was calculated from Chianti (Dere et al., 1997; Del Zanna et al., 2021). O VI is confined to a narrower range of temperatures in the static curve than in our simulations, which include dynamic mixing of warm and hot gas.

the f_{OVI} is shown in Figure 2.4. At the beginning of each simulation, f_{OVI} is small. Over time, the cloud mixes with the ambient gas, causing f_{OVI} to rise. At even later epochs, f_{OVI} stabilizes.

For comparison with observations, we estimate the column density of H I using the following method. Although FLASH cannot distinguish H I from H II in each cell, it can track the ionization and recombination of other elements. We therefore use O I to trace H I. We calculate the quantity of H I in collisionally ionized gas from the ratio of O I to all oxygen in the cell times the quantity of hydrogen in each cell. This calculation is justified because the ratio of H I to all hydrogen is approximately equal to the ratio of O I to all oxygen, since oxygen and hydrogen have very similar first ionization potentials (Cox, 2000) and charge exchange between O II and H I particles is common (Field & Steigman, 1971). We use this procedure to calculate the column densities of neutral hydrogen for every sightline through the HVC; these are the column densities in collisionally ionized gas. Then, in order to approximate the effect of photoionization, we subtract from these column densities the column density of hydrogen that has been photoionized. We use the resulting H I to calculate the ratio of H I to O VI.

For each epoch in a simulation, we calculate the ratio of H I to O VI over the entire cloud. These curves can be seen in Figure 2.5. This ratio is highest at the start of the simulation; this is because there

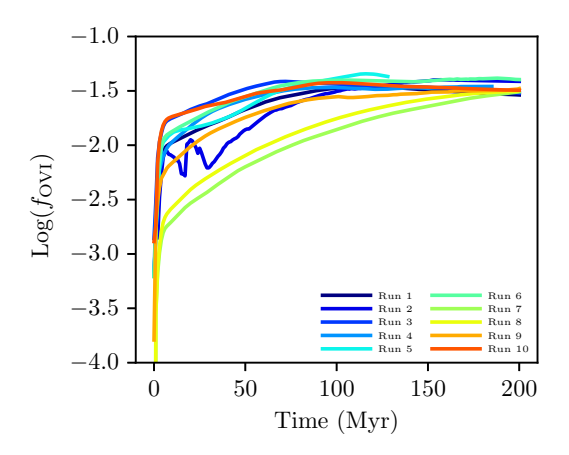


Figure 2.4: Plot of the cloud-averaged $f_{\rm OVI}$ for each simulation as a function of time. Generally, $f_{\rm OVI}$ increases with time as the cloud mixes with the ambient material.

has been little mixing and so the cloud consists of mostly cool, neutral gas. As the simulation evolves, the cloud mixes with the ambient gas, causing this ratio to decline until it reaches an asymptote. For comparison, the ratio of H I to O VI in the MS is 1.7×10^4 (Fox et al., 2010). This value is shown in Figure 2.5 as a horizontal line. Our simulations best replicate the MS during the epochs when they have the same H I/O VI ratios as these clouds.

Table 2.2 lists the 3 sight lines through the MS for which H I and O VI have been measured by Fox et al. (2010). We use the ratios of these observed H I and O VI column densities to determine the most appropriate epochs in the simulations for further analysis. We then determine the value of $f_{\rm OVI}$ at the corresponding epoch for each simulation for each sight line, using the values plotted in Figure 2.4. Note that $f_{\rm OVI}$ is not very sensitive to the choice of epoch. We then determine the average value of $f_{\rm OVI}$ for each sight line by averaging the corresponding $f_{\rm OVI}$ s from the ten simulations at the epochs when their H I/O VI ratio matches that of the sight line. Our results are shown in Table 2.2. Our ionization fractions are significantly lower than the maximum value of 0.22 predicted from CIE and NEI models of static gas (Sutherland & Dopita, 1993; Gnat & Sternberg, 2007). Until now, the maximum $f_{\rm OVI}$ in static gas has been used to determine the mass of hot ionized hydrogen in HVCs (Fox et al., 2010; Sembach et al., 2003). The ratio of the maximum $f_{\rm OVI}$ in static gas to our average $f_{\rm OVI}$ in dynamic gas ranges from

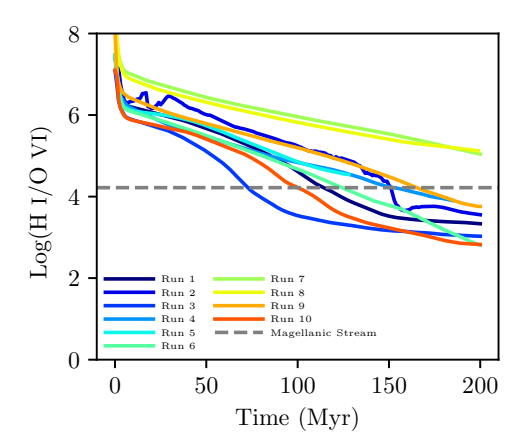


Figure 2.5: Plots of H I/O VI for each simulation as a function of time. Generally, H I/O VI decreases with time as hydrogen is ionized and $f_{\rm OVI}$ increases (see Figure 2.4). Also shown is the average observed H I/O VI ratios for the MS (Fox et al., 2010).

6.3 (NGC 7469, HE 0226-4110) to 6.5 (Mrk 335). For many sight lines in Complex C, these ratios are even larger (Goetz et al., 2024). This result leads to a related increase in the mass of HVCs, as shown below.

Table 2.2: $f_{ m OVI}$				
Clouds	Sight lines	$f_{\mathrm{OVI}}^{\mathrm{a}}$		
Magellanic	NGC 7469	0.035		
Stream	Mrk 335	0.034		
	HE 0226-4110	0.035		
	Average $f_{ m OVI}^{ m \ b}$	0.035		
	$f_{ m OVI}$ from average H I/O VI $^{ m c}$	0.036		

^a The $f_{\rm OVI}$ for each individual sight line is calculated using the H I/O VI of individual sight lines from Fox et al. (2010). It is the average of the values obtained from the ten simulations.

^b This $f_{\rm OVI}$ is the average value of the $f_{\rm OVI}$ of the three sight lines in the MS. It is calculated from the unrounded values.

^c This $f_{\rm OVI}$ is the average value of those calculated from the simulations at the epochs when (H I/O VI) matches the mean value of H I/O VI for the three sight lines listed.

2.3.2 New Methodology for Calculating N(H)

Until now the typical method for calculating the amount of ionized hydrogen associated with observed column densities of O VI has been:

$$N(H II) = \frac{N(O VI)}{\left(\frac{O}{H}\right)\left(\frac{O VI}{O}\right)}$$
(2.1)

e.g., (Sembach et al., 2003; Fox et al., 2010) where N(O VI) is the column density of O VI, (O/H) is the metallicity, and (O VI/O) is $f_{\rm OVI}$. Without specific knowledge of the temperature distribution of gas in a cloud, it is common for researchers to adopt $f_{\rm OVI}$ as less than or equal to the maximum value in the theoretical $f_{\rm OVI}$ curve for static gas. When Fox et al. (2010) used this method for the MS, they adopted $f_{\rm OVI} \leq 0.22$ from a static gas model (Gnat & Sternberg, 2007). Figure 2.3 compares $f_{\rm OVI}$ vs temperature for that static model with our dynamic results. In the static model, O VI only exists in a narrow temperature range around $10^{5.5}$ K, where nearly all of the hydrogen is expected to be ionized. Hence, typically the left side of Equation 2.1 is N(H II) rather than N(H) (e.g., Fox et al. (2010)). Sembach et al. (2003) adopted $f_{\rm OVI} \leq 0.2$ in their analysis in Complex C and used Equation 2.1.

Fox et al. (2010) also calculated the column densities of ionized hydrogen associated with Si IV and low ions. Their H II column densities associated with Si IV and O VI are also lower limits because the ionization fractions used are upper limits. Recognizing that there is a wide range of temperatures in a cloud, they then summed the H II column densities associated with low ions, Si IV, and O VI to achieve the total H II column density.

They made this summation because they assume that the low ions, Si IV, and O VI trace different temperature regimes and therefore different populations of H II. However, the turbulent mixing layer simulations of Kwak & Shelton (2010) show that this is not always the case. Individual cells can have populations in several ionization states. In addition, 97% of the cloud material has an O VI volume density of 10^{-9} cm⁻³ in the same simulation and epoch.

These points raise the question of how well adding temperature phase components reproduces the total amount of hydrogen. As a simple example, consider a cloud in which there is an equal amount

of oxygen in each ionization state. For the sake of argument, the total amount of hydrogen might be calculated in the following way:

$$N(H)_{\text{calc}} = \sum_{i=1}^{9} \frac{N(O_i)}{Zf_{i,max}},$$

where $N(O_i)$ is the column density of the ith oxygen ion, Z is the oxygen metallicity, and $f_{i,max}$ is the maximum ionization fraction for the ith ionization state of oxygen. Note that this $f_{i,max}$ is different from the actual fraction of ions in the ith ionization state in this example, which is $\frac{1}{9}$. Since Z is a constant and $N(O_i)$ is equal to $\frac{1}{9}$ th of the total oxygen column density, N(O), the above equation reduces to

$$N(H)_{\text{calc}} = \frac{N(O)}{9Z} \sum_{i=1}^{9} \frac{1}{f_{i,max}}.$$

Since $\frac{N(O)}{Z}$ is equal to the actual column density of hydrogen, $N(H)_{act}$, the expression further reduces to:

$$N(H)_{\text{calc}} = \frac{N(H)_{\text{act}}}{9} \sum_{i=1}^{9} \frac{1}{f_{i,max}}.$$

If $f_{i,max}$ were set to the maximum ionization fractions for oxygen from the CIE tables of Gnat & Sternberg (2007), then $\sum_{i=1}^{9} \frac{1}{f_{i,max}} = 15.3$, so $N(H)_{calc} = 1.70N(H)_{act}$. This technique overcounts the actual hydrogen column density by 70%.

Of course, it is unlikely that all 9 ionization states of oxygen would be observed for a sight line. A more practical example would be to use just a few ions that are expected to span the entire temperature range of the cloud. As an example, consider O I, C II, Si IV, and O VI. In this example, the total calculated hydrogen column density might be given as:

$$N(\mathrm{H})_{\mathrm{calc}} = \frac{N(\mathrm{O\:I})}{Z_O f_{\mathrm{OI,max}}} + \frac{N(\mathrm{C\:II})}{Z_C f_{\mathrm{CII,max}}} + \frac{N(\mathrm{Si\:IV})}{Z_{Si} f_{\mathrm{SiIV,max}}} + \frac{N(\mathrm{O\:VI})}{Z_O f_{\mathrm{OVI,max}}},$$

where Z_O , Z_C , and Z_{Si} are the oxygen, carbon, and silicon metallicities, respectively. As has been done frequently, the ionization fractions used here would be the maxima from Gnat & Sternberg (2007). This

calculation assumes that each ion is found in a disjoint temperature range and traces distinct gas. If each temperature range is in CIE at the temperature that maximizes the ionization fraction from static CIE gas models, then this equation would accurately capture the total hydrogen column density along the sight line. However, our dynamic simulations show that different ions can overlap significantly in temperature. There is also observational evidence of high ions such as O VI existing at a wide range of temperatures (see Section 2.4). Therefore, it is not accurate to assume that each ion traces different populations of gas. To account for this, we can define an ionization fraction of O VI that considers O VI at all temperatures along a sight line as the total number of O VI ions divided by the total number of oxygen atoms ($f_{\rm OVI,act}$). Suppose that for a given sight line, $f_{\rm OVI,act}$ differs from the maximum ionization fraction predicted from the static gas models of Gnat & Sternberg (2007) by a factor of $\beta_{\rm OVI}$, i.e., $f_{\rm OVI,act} = \beta_{\rm OVI} f_{\rm OVI,max}$, and likewise for the ionization fractions of O I, C II and Si IV. Then, the previous equation can be re-written as:

$$N(\mathrm{H})_{\mathrm{calc}} = \frac{N(\mathrm{O\ I})\beta_{\mathrm{OI}}}{Z_O f_{\mathrm{OI,act}}} + \frac{N(\mathrm{C\ II})\beta_{\mathrm{CII}}}{Z_C f_{\mathrm{CII,act}}} + \frac{N(\mathrm{Si\ IV})\beta_{\mathrm{SiIV}}}{Z_{Si} f_{\mathrm{SiIV,act}}} + \frac{N(\mathrm{O\ VI})\beta_{\mathrm{OVI}}}{Z_O f_{\mathrm{OVI,act}}}.$$

However, $\frac{N(\text{O VI})}{f_{\text{OVI,act}}}$ is by definition equal to the actual column density of oxygen along the entire sight line, $N(\text{O})_{\text{act}}$. Additionally, since Z_O is the oxygen abundance along the sight line, $\frac{N(\text{O})_{\text{act}}}{Z_O}$ is equal to the total hydrogen column density along the sight line, $N(\text{H})_{\text{act}}$. The same argument applies to O I, C II and Si IV. This allows a further simplification:

$$N(H)_{\text{calc}} = N(H)_{\text{act}} (\beta_{\text{OI}} + \beta_{\text{CII}} + \beta_{\text{SiIV}} + \beta_{\text{OVI}}).$$

This example highlights the problem with using multiple ions and assuming maximum ionization fractions. As a hypothetical example, consider a sight line that contains a substantial amount of O VI, such that $\beta_{\rm OVI}=\frac{1}{2}$, and lesser amounts of O I, C II, and Si IV, such that $\beta_{\rm OI}=\beta_{\rm CII}=\beta_{\rm SiIV}=\frac{1}{4}$. These choices of values may be realistic for a sight line that contains significant portions of hot gas. Using those β values, the sum of the four actual ionization fractions would be ~ 0.64 , indicating that a substantial percentage of the metals along the sight line are in those ionization states. In this case, this method would

overcount the total hydrogen column density by a factor of 1.25. On the other hand, if each ion's ionization fraction is smaller than its CIE maximum value by a factor such as 6.3–22.2, which are the factors found from our simulations for O VI, then this method results in undercounting by a factor of 1.6–5.6.

The above logic would need only slight modification if Cloudy is used to find the low ion column density and the neutral hydrogen column density is observed directly rather than deduced via O I, as in Fox et al. (2010).

From observations alone, it is not possible to obtain values for β , so it would not be clear whether the calculated hydrogen column density is over or under counting the actual hydrogen column density. However, dynamic NEI computer simulations make it possible to calculate the ionization fraction of O VI (or any other ion) in simulated clouds. This ionization fraction takes into account O VI found throughout the whole cloud and therefore coincident with neutral and ionized hydrogen. As a result, we remove the assumption that O VI only traces hot, ionized gas in Equation 2.1 by replacing N(H II) with N(H) and using the O VI/O from our simulations. The result is Equation 2.2, which is more mathematically accurate since the metallicity is the ratio of the total amount of oxygen to the total amount of hydrogen, not just ionized hydrogen.

$$N(H) = \frac{N(O \text{ VI})}{\binom{O}{H} \binom{O \text{ VI}}{O}}.$$
 (2.2)

Table 2.3: Magellanic Stream Log Column Densities

Sight Lines	N(O VI) ^a	N(H I) ^a	N(H II) _{o vi} a	N(H II) _{low + Si IV} ^a	N(H I)+N(H II)	N(H) ^b	N(H) _{alt} ^c
-	(cm^{-2})	(cm^{-2})	(cm^{-2})	(cm^{-2})	(cm^{-2})	(cm^{-2})	(cm^{-2})
NGC 7469	14.09	18.63	>19.10	>19.90	>19.98	19.71	19.70
Mrk 335	13.84	16.67	>18.80	>18.95	>19.18	19.80	19.78
HE 0226-4110	13.91	≈ 17.0	>18.9	>19.18	>19.37	19.68	19.66

^a The values of N(O VI), N(H I) and N(H II) are from Fox et al. (2010).

Since a single sight line may happen to pass through particularly cool or hot gas, we recommend using multiple sight lines when comparing with our method.

^b For each sight line, the value of N(H) is calculated using N(O VI) from Fox et al. (2010) and f_{OVI} in Table 2.2.

^c For each sight line, the alternate value of N(H) is calculated using N(O VI) from Fox et al. (2010) and the " f_{OVI} from average H I/O VI" in Table 2.2.

2.3.3 Comparisons

To see the effect of shifting to this new methodology, we calculate N(H) for the sight lines in Fox et al. (2010), using Equation 2.2, our $f_{\rm OVI}$, and N(O VI) taken from the observations reported in Fox et al. (2010). These values are shown in column 7 in Table 2.3. We think this is the most accurate method for calculating the total hydrogen densities, but we also provide the values calculated from the averages of the $f_{\rm OVI}$ s extracted from the simulations at the epochs when the values of H I/O VI match the average values of H I/O VI from Fox et al. (2010) and Sembach et al. (2003).

Here, we compare with the published results for the MS. Fox et al. (2010) include their estimated H II column density associated with low ions and Si IV. These numbers are tabulated in Table 2.3. These additional components must be considered when comparing the total masses. For the H II associated with Si IV, Fox et al. (2010) did a similar calculation as for O VI, but using the Si IV column densities, metallicity, and maximum CIE ionization fraction. For the H II associated with low ions, Fox et al. (2010) used Cloudy to model the degree of ionization in the cloud, assuming that the low ions come from photoionization rather than NEI collisional ionization. The H II column density associated with low ions comes from the best-fitting model. The total hydrogen column density predicted by Fox et al. (2010) is the sum of H I and the H II associated with low ions, Si IV, and O VI.

For the three sight lines listed in Table 2.3, our N(H) values (column 7) are an average of 2.2 times larger than the totals in column 6 found from Fox et al. (2010). Column 6 in Table 2.3 contains lower limits. For the first sight line, NGC 7469, our result is actually smaller than that found from Fox et al. (2010). That sight line is richer in low ions and Si IV than high ions and therefore has a low predicted O VI column density. Since our method is solely based on the observed O VI column density, it results in a low hydrogen column density. The other two sight lines are tilted more towards O VI, and so our method produces higher hydrogen column densities.

We do a similar analysis with Complex C, the results of which are summarized here. For more details, see Goetz et al. (2024). We find that our calculated N(H) values (column 6) are an average of 2.6 times

larger than the total column densities from Sembach et al. (2003), calculated from the sum of the observed N(H I) and the N(H II) found from Equation 2.1.

We now examine the effect of metallicity. Changing the metallicity of the cloud or ambient material shifts the H I/O VI vs time curve, changing the epoch that best matches observations. This changes the corresponding $f_{\rm OVI}$ value that is used to calculate the hydrogen column density. In the case of increasing the cloud's metallicity, the effect is to decrease the appropriate $f_{\rm OVI}$. However, since $f_{\rm OVI}$ is multiplied by the cloud metallicity when calculating the hydrogen column density, the decrease in $f_{\rm OVI}$ is mitigated by the increase in metallicity. The net result is a small change to the hydrogen column density. In the case of changing the ambient metallicity, the effect on the H I/O VI vs time curve is tiny, resulting in no significant change to the choice of $f_{\rm OVI}$ or calculated hydrogen column density. See Figures 2.6 and 2.7.

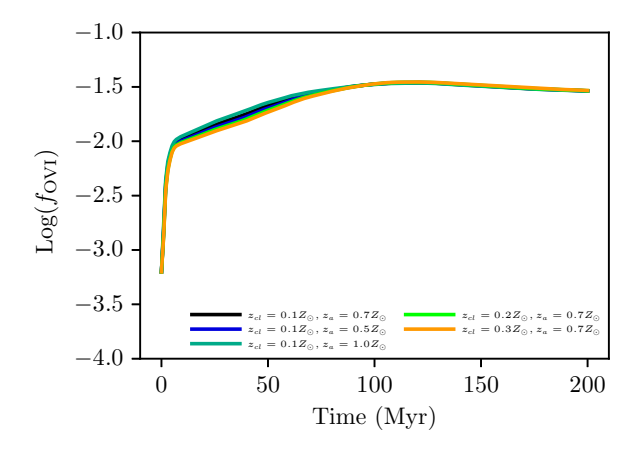


Figure 2.6: Plot of $f_{\rm OVI}$ for Run 1 for a variety of cloud and ambient metallicities. Changing the ambient metallicity has little effect on the curve. Changing the cloud metallicity has a more noticeable but still insignificant effect.

2.4 Discussion

We find that the O VI/oxygen ratio is greatly affected by dynamic mixing between hot and cool gas. NEI ionization and recombination are much more important in mixed gas than in static gas, resulting in a significantly different $f_{\rm OVI}$. The $f_{\rm OVI}$ for static gas is substantial only for a narrow range of temperatures and peaks at a value of 0.22 at a temperature of 3×10^5 K. This value is often used as an upper limit

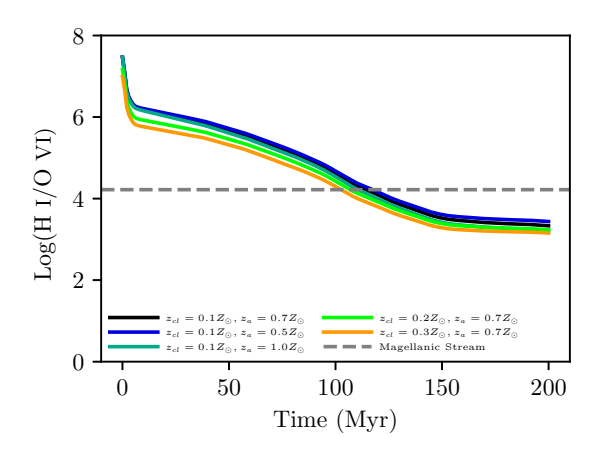


Figure 2.7: Plots of H I/O VI for Run I for a variety of cloud and ambient metallicities. As for $f_{\rm OVI}$, changing the ambient metallicity has little effect on the curve. Changing the cloud metallicity has a more noticeable, but still small effect.

in calculations. In contrast, the $f_{\rm OVI}$ in our simulations is substantial across 3 orders of magnitude in temperature, from $\sim 2 \times 10^3$ K to $\sim 2 \times 10^6$ K. Considering that the actual value of $f_{\rm OVI}$ varies over time and space, we adopt the value of $f_{\rm OVI}$ averaged over the whole simulated cloud at the time when the simulated H I/O VI ratio best matches the ratio for the observed sight line.

For any given sight line, we have 10 values of $f_{\rm OVI}$, one from each simulation. For each sight line, we compare the $f_{\rm OVI}$ values from the 10 simulations. Amongst the simulations, the standard deviation of $f_{\rm OVI}$ is small – roughly 5-13% of the average value across the 10 simulations. This suggests that the choice of initial parameters for the simulations does not have a large effect on the final results. Our average $f_{\rm OVI}$ are 4.5% - 15.9% of the peak $f_{\rm OVI}$ for static gas.

Historically, $f_{\rm OVI}$ has been used to estimate the quantity of hydrogen associated with the observed O VI. Our simulations show that O VI can be found in cool gas, where neutral hydrogen can exist, so we revise the methodology such that it predicts the sum of the neutral and ionized hydrogen. The differences between our method (Equation 2.2) and the previous method (Equation 2.1) are that 1.) our result is the total hydrogen column density including the neutral hydrogen, while the previous method attributes the resulting column density to only the ionized hydrogen around a temperature of 3×10^5 K; 2.) we use the

average of f_{OVI} of the simulated cloud instead of the peak value of f_{OVI} in CIE gas; and 3.) our method is an equality while the previous method provides a lower limit.

We use our method to estimate N(H) for sight lines through the MS from the observed $N(O\ VI)$ (Fox et al., 2010). Our values of N(H) are 2.2 times greater than the sum of the observed $N(H\ II)$ and the $N(H\ II)$ calculated using the older methodologies described in Section 2.3.3. It should be noted that the quoted $N(H\ II)$ from the MS is the sum of multiple components.

Stationary CIE and NEI gas has a very different $f_{\rm OVI}$ than dynamic NEI gas. This difference has several implications. First, as shown above, there should be more material in HVCs than previously thought. Our column densities are noticeably higher than previous lower limits; therefore, our cloud masses would be correspondingly higher as well. This logic should apply to any HVC for which the H II column density is calculated from the O VI column density.

Another implication pertains to low-redshift extragalactic O VI absorbers. Sembach et al. (2004) analyzed 25 low-redshift extragalactic O VI absorbers along the line of sight to PG 1116+215, finding that their ionization pattern was similar to that of HVCs. Furthermore, our finding that a significant portion of the O VI is in gas with temperatures below 10⁵ K (see Figure 2.3) also agrees with observations of low-redshift extragalactic O VI systems. Tripp et al. (2008) analyzed 51 O VI systems, finding that at least a third of the intervening O VI components "present compelling evidence of cool temperatures $(\log(T) < 5.0)$." This suggests that these systems are out of equilibrium. Another example of cool O VI is from Savage et al. (2014), who examined 14 sight lines with Hubble Space Telescope's Cosmic Origins Spectrograph (HST/COS). They saw 54 low-redshift O VI absorber systems, which they decomposed into 85 components. They discussed the O VI absorber components that aligned well with the H I components. Among the 45 well-aligned components, 31 have narrow line widths, implying values of log(T) < 4.8. This is much smaller than the CIE temperature, log(T) = 5.5. Traditionally, such narrow lines were thought to be due to the photoionization, but mixing can result in regions where the gas temperature is much less than the CIE temperatures of ions present in the gas (Kwak & Shelton, 2010). These examples show that significant amounts of O VI in low-redshift intergalactic absorbers are out of CIE. Therefore we use our NEI f_{OVI} to revise the estimate of the baryonic content of these systems.

Based on our f_{OVI} , there should be more material in low-redshift extragalactic regions than previously thought. The amount of low-redshift extragalactic material in these O VI systems has been estimated from observations of the O VI column density, like was done with HVCs (Tripp & Savage, 2000; Tripp et al., 2000; Sembach et al., 2004). In these cases, f_{OVI} appears in the denominator of the equation. Here we apply our f_{OVI} to those observations. These low-redshift extragalactic O VI absorbers have smaller H I/O VI ratios than either the MS or Complex C. Our simulations do not produce such low H I/O VI ratios within the simulated timeframe, but at late times our simulations asymptote to their lowest values of H I/O VI and their highest values of f_{OVI} . We therefore adopt the value of f_{OVI} at the last epoch from each simulation. We then average across the 10 simulations to produce a single estimated $f_{\rm OVI}$ of 0.034. Using this value of $f_{\rm OVI}$ in Equation 7 in Sembach et al. (2004), rather than their chosen value ($f_{\text{OVI}} \leq 0.2$), increases the baryonic content (Ω_b) of O VI absorbers by up to a factor of 5.9, to $\Omega_b(O\ VI) = 0.013\ h_{75}^{-1}$. This result implies that the amount of material in low-redshift extragalactic O VI absorption line systems is enormous. It is several times larger than the baryonic content of the stars and gas in galaxies, i.e., $0.0032h_{75}^{-1}$ (Fukugita et al., 1998; Fukugita & Kawasaki, 2003). It is also over a third of the expected baryonic content of the Universe (Richter et al., 2006). Similarly, Shull et al. (2012) used hydrodynamic simulations to calculate NEI f_{OVI} values that are lower than those from static gas models. They then recalculated the baryonic content of the warm and hot intergalactic medium using their $f_{\rm OVI}$ and found a greater Ω_b than the previous value.

We believe that our methodology provides a more accurate estimate of the hydrogen column density along sight lines through HVCs and this method can be applied to additional clouds for which H I and O VI have been observed. Our prescription is to use the observed H I/O VI ratio to determine $f_{\rm OVI}$, using the equation discussed below, and then use it and the observed O VI column density with Equation 2.2 to determine the total hydrogen column density.

The simulations show that the H I/O VI ratio is well correlated with f_{OVI} (see Figure 2.8). The value of f_{OVI} falls monotonically with increasing H I/O VI, allowing for a one-to-one relationship between observed H I/O VI and predicted f_{OVI} . Thus, an accurate f_{OVI} for a given sight line can be uniquely determined from the ratio of observed H I and O VI column density. The relationship between f_{OVI}

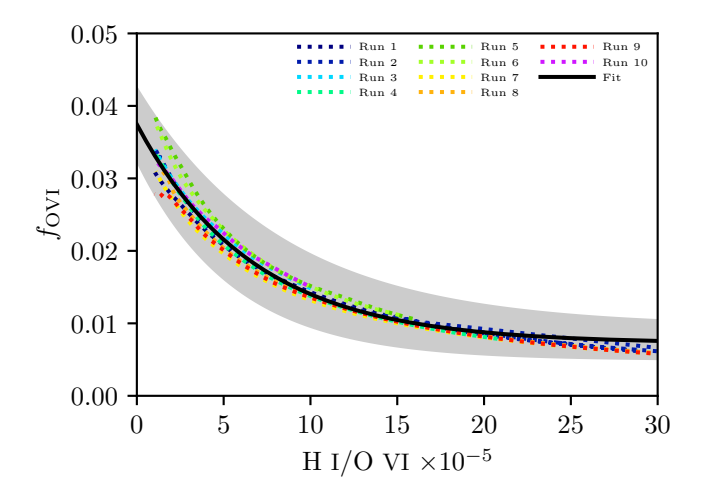


Figure 2.8: $f_{\rm OVI}$ vs H I/O VI ratio for the cloud material at each epoch of the simulations. Different colors represent different simulations. A non-linear fit of the form $Ae^{-bx}+C$ was performed for each simulation, where x=H I/O VI $\times 10^{-5}$, and the best fit values for A, b, and C were averaged. The curve with those values (i.e., $0.03e^{-0.17x}+0.007$) is plotted with a black solid line. The shaded region depicts the 1 sigma uncertainty on the fit parameters. This empirical relationship between $f_{\rm OVI}$ and H I/O VI can be used to estimate a reasonable value of $f_{\rm OVI}$ from an observed H I/O VI ratio. Our plot extends past the typical range of observed H I/O VI values, into a region where the fit slightly diverges from the simulation results.

and H I/O VI is largely independent of the input parameters of the simulations. The best fit to these simulational data is:

$$f_{\text{OVI}} = (0.030 \pm 0.003)e^{(-0.17 \pm 0.03)x} + (0.007 \pm 0.002)$$
 (2.3)

where $x = H I/O VI \times 10^{-5}$.

This analysis has been performed with oxygen. However, there are also large data sets for other elements, such as C, Si and Ne (Burchett et al., 2019). We plan to add such elements into our simulations and incorporate them in our methodology, so that hydrogen column densities can be calculated.

2.5 Author Contributions

Both Chen Wang and I, independently, ran all ten simulations and performed the analysis. I developed the prescription described in Section 2.4. Chen Wang and I worked together to compare our results with observations. The calculations related to the comparison with the Magellanic Stream are shown here, while those for Complex C will be in Chen Wang's thesis. Goetz et al. (2024) includes results for both the Magellanic Stream and Complex C. Robin Shelton contributed to the writing of Goetz et al. (2024).

All co-authors agree that the work may be included in this dissertation.

CHAPTER 3

COLLISIONS BETWEEN DARK MATTER

CONFINED HIGH VELOCITY CLOUDS

AND MAGNETIZED GALACTIC DISKS:

THE SMITH CLOUD, PART II ¹

¹Shelton, R. L., Goetz, E. H., & Galyardt, J. E. 2024, ApJ,405975, 96, doi: 10.3847/1538-4357/ad75fc. Reproduced with permission from the Astrophysical Journal.

Abstract

We present high resolution simulations of high velocity clouds (HVCs) colliding with the outer part of the Galactic disk. All of the simulations include a $3\times10^8~\rm M_\odot$ dark matter subhalo. Three simulations model a dark matter subhalo without a gaseous component, while eight simulations model a dark matter subhalo accompanied by a gaseous cloud of mass 2 to $8\times10^6~\rm M_\odot$. Half of the simulations include the coherent component of the Galaxy's magnetic field. Each simulation spans ~40 million years before the collision and ~40 million years after the collision. The collisions between the gas cloud and disk splash gas into the halo, punch half-kpc size holes in the disk, and form long-lived, multi-kpc size shells. Each shell encloses a bubble of relatively cool gas. Holes and shells of these scales would be observable and some have been observed in the past. We determine the fate of the HVC gas, temperature, composition, and ionization state of the bubble and shell gas, size and longevity of the holes, and effects of cloud density. The simulations show that the clouds do not survive the chaos of passage through the disk, but instead become part of the splash, bubble, and shell. Some dark matter clouds may appear to carry material with them long after the collision, but this material is shell gas that was captured by the dark matter subhalo. These results have ramifications for the Smith Cloud and other clouds hypothesized to have hit the Galactic disk.

3.1 Introduction

Many galaxies are evolving under the influence of collisions with infalling material. Forensic evidence shows that the Milky Way has been hit by objects as small as high velocity clouds (HVCs) and as large as dwarf galaxies (McClure-Griffiths et al., 2008; Izumi et al., 2014; Park et al., 2016; McMillan et al., 2022). Here, we consider HVCs, of the mass of the Smith Cloud, colliding with a disk galaxy like the Milky Way.

It has long been claimed that these collisions induce star formation. This is observationally apparent for the case of galaxy collisions and is simulated for the case of HVC collisions (Comeron & Torra, 1994; Alig et al., 2018). Even collisions between gas-free dark matter subhalos and galaxy disks can create the conditions for star formation (Bekki & Chiba, 2006).

Perhaps one of the most dramatic consequences of collisions is that they punch holes in the disk (Mirabel, 1982). There is substantial simulational evidence for this (Bekki & Chiba, 2006; Kannan et al., 2012; Galyardt & Shelton, 2016; Shah et al., 2019). There is also observational evidence, in that the simulational results of Shah et al. (2019) compare favorably with the observed holes in NGC 247 (Wagner-Kaiser et al., 2014). In addition, Bekki & Chiba (2006) suggested that the H I hole in NGC 6822 could have resulted from an impact with the dwarf galaxy "NW cloud". Here, we explore this general phenomenon further. We simulate clouds with and without dark matter and examine the holes they form. We also relate the size of the hole to the baryonic mass of the cloud. As expected, clouds with larger baryonic masses make larger and longer-lasting holes in the disk. Clouds without baryonic mass, but with a few hundred million solar masses of dark matter, do not produce substantial holes.

As the clouds punch through the disk, they push disk material downward, creating shells of HVC material and swept up gas (Vorobyov & Basu, 2005; Galyardt & Shelton, 2016). See also Mirabel (1982); Heiles (1984). Each shell grows to become a supershell. Here, we follow up the earlier work by tracing the origins of the supershell material and providing simulational predictions of its observational characteristics.

The fate of the cloud is also of interest. This is especially pertinent to the Smith Cloud, a $>4 \times 10^6$ M_{\odot} cloud (Lockman et al., 2008; Hill et al., 2009), located approximately 12 kpc away at l=39°, b= -13° (Lockman et al., 2008). Based on the Smith Cloud's trajectory, Lockman et al. (2008) suggested that it

could have already passed through the disk. This raised the question of how the Smith Cloud would have survived its passage through the disk. Nichols & Bland-Hawthorn (2009) suggested that the Smith Cloud contains dark matter that shepherded the cloud through the disk. They used semi-analytic calculations to model the gas cloud's response to the gravity of the dark matter subhalo and the ram pressure resulting from the passage through the disk. They estimated that 5-50% of the cloud material passes through the disk and remains with the dark matter subhalo. They concluded that the Smith Cloud had passed through the disk ~ 70 Myr ago, in agreement with Lockman et al. (2008).

Nichols et al. (2014) followed up with RAMSES (Teyssier, 2002) simulations that modeled the hydrodynamic effects of the collision and the gravitational pull of the dark matter subhalo. Their gas clouds ranged in mass from $1.3-7.8\times10^6\,M_\odot$ and their dark matter subhalo had a mass of $3\times10^8\,M_\odot$. They presented figures of the modeled Smith Cloud as it would appear today. These figures show a nebulous overdensity in the wider vicinity of the modeled dark matter subhalo. They concluded that shepherding by the dark matter enabled the gas clouds to survive passage through the disk with little to no mass loss.

Wanting to consider the screening effect of the Galactic magnetic field and to see the cloud's evolution as it collides with and passes through the disk, Galyardt & Shelton (2016) revisited the issue. They used FLASH (Fryxell et al., 2000) to simulate the magnetohydrodynamics of the cloud and Galaxy and the gravity of the dark matter subhalo. Their gas clouds had an initial mass of $5\times10^6~M_\odot$ and their dark matter subhalos had initial masses of $3\times10^8~M_\odot$ or $1\times10^9~M_\odot$. We have examined their simulation files and determined that the simulations had a maximum resolution of 15.6 pc. See Section 4.2 for a discussion of minimum cell size. In both the magnetic and non-magnetic set-ups, their simulations show that the passage through the disk strips the cloud gas from the dark matter subhalo. However, at late times, the subhalo is accompanied by a small amount of material that appears to have been accreted from the surroundings. This raises interesting questions about where the material accreted by the subhalo comes from and where the cloud material ends up.

Next, Tepper-García & Bland-Hawthorn (2018) simulated the Smith Cloud using the RAMSES hydrodynamic code (Teyssier, 2002). They found that a cloud with initial gas mass $1.6 \times 10^7 \, M_\odot$ and dark matter subhalo mass $2.4 \times 10^8 \, M_\odot$ is screened out by the collision with the disk and becomes a

streamer of material that merges with the halo. Their simulation was done with a resolution of 15 pc. In addition, Tepper-García & Bland-Hawthorn (2018) considered a cloud with an initial gas mass of $1.5 \times 10^8 \, \rm M_\odot$ and dark matter subhalo mass of $1.0 \times 10^9 \, \rm M_\odot$. They performed two simulations with the latter initial masses. One simulation had a resolution of 15 pc, while the other had a resolution of 60 pc. In the high resolution case, the cloud survives but loses half of its initial mass. In the low resolution case, the cloud is destroyed in a similar way to the low mass case. Based on this comparison, they suggested that the difference in survivability between their results and those of Galyardt & Shelton (2016) was due to simulational resolution. However, this difference could also be due to the much larger cloud mass. Their $1.5 \times 10^8 \, \rm M_\odot$ cloud survived while their $1.6 \times 10^7 \, \rm M_\odot$ cloud, which was more than twice as massive as the clouds in Galyardt & Shelton (2016), was destroyed.

Here, we revisit the cloud collision problem using 15.6 pc and 7.8 pc resolution, which meets or exceeds the resolution used by Tepper-García & Bland-Hawthorn (2018). We use the FLASH simulation framework including hydrodynamics and gravity (Fryxell et al., 2000). Some of our simulations also include a Galactic magnetic field. With FLASH, we model the interactions between the baryonic and dark matter components of the cloud and the outer disk of the Milky Way, where the trajectory calculated by Lockman et al. (2008) intersects the disk. We aim to examine survivability and other intriguing behaviors of the cloud. We examine clouds of different masses, finding that the less massive clouds are better blocked by the disk and confirming that HVC-sized clouds are destroyed. This suggests that the Smith Cloud is on its first approach towards the disk of the Milky Way. The fact that some of the earlier simulations showed material following the dark matter minihalo raises the question of where this material originated: the cloud, disk, or halo. Our simulations show that the trailing material is a mixture of all three, with ratios that depend on the amount of time since the collision and the initial density of the cloud. Furthermore, we examine the hole and shell formed by the cloud's collision with the disk. We also explore a case without a baryonic cloud. Without a baryonic cloud, there is a small disturbance in the disk as the dark matter subhalo passes through, but no hole or shell is formed. The simulation set up and parameters are discussed in Section 4.2. The results are presented in Section 3.3. In Sections 3.4, we discuss and summarize the results.

3.2 Simulations

We use FLASH (Fryxell et al., 2000) version 4.3 to simulate a portion of the Milky Way galaxy with an HVC moving through it. The simulation domain is a 4 kpc \times 4 kpc \times 24 kpc region in Cartesian coordinates and is centered on the Galactic disk at a Galactocentric radius of $R_{\rm gal} = 13$ kpc. The mass densities of the Milky Way's disk and halo are taken from the mass model of the Milky Way developed in Galyardt & Shelton (2016) from references therein. They result in an average hydrogen column density of the disk at the impact site of $10^{21.1}$ atoms cm⁻². The temperature profile of the ambient material is also taken from Galyardt & Shelton (2016). We use the coherent component of the Galactic magnetic field from Jansson & Farrar (2012a), with some smoothing to enhance numerical stability. We set the ratio of metal nuclei to hydrogens to be similar to that of the Milky Way's outer disk. We refer to this ratio as the metal abundance and express it in terms of the Sun's metal abundance, Z_{\odot} , which we adopt from Anders & Grevesse (1989).

FLASH segments the 3-dimensional Cartesian computational domain into blocks, each of which is subdivided into $8 \times 8 \times 8$ cells or zones during the simulation (Fryxell et al., 2000). With adaptive mesh refinement, the initial blocks can be subdivided multiple times in each Cartesian direction. A maximum refinement level of l corresponds to subdividing each initial block into 2^l blocks in each Cartesian direction. As a consequence, with initial block sizes of 2 kpc \times 2 kpc \times 2 kpc and a maximum refinement of 4 or 5, the smallest cell in a fully refined region of the domain is 15.6 pc or 7.8 pc, respectively. Following this rubric, the Galyardt & Shelton (2016) simulations, which had the same domain size and block structure as our simulations and a maximum refinement level of 4, had a minimum cell size of 15.6 pc.

We have included hydrogen, helium, and carbon in our simulations. The ionization and recombination of helium and carbon are calculated in a time dependent manner, although the ionization and recombination of hydrogen are not. The hydrogen is treated as if it is fully ionized in FLASH's calculations of thermal pressure.

Eight of our simulations track a gas cloud accompanied by a dark matter minihalo. The remaining 3 simulations track dark matter minihalos without accompanying gas clouds. In each case, the cloud

and/or minihalo is placed 10 kpc above the midplane and given an initial velocity of 200 km s⁻¹ toward the disk, resulting in a similar collision velocity to that of Tepper-García & Bland-Hawthorn (2018). The transverse bulk velocity is set to zero. When present, the baryonic cloud is spherical and has a 500 pc initial radius (see Table 3.1). Its gas density varies from one run to another, within the range of hydrogen number densities of 0.1 to 0.5 cm⁻³ (see Table 3.1). The hydrogen is accompanied by helium and carbon such that the gas density is 1.4 m_H n_H , where m_H is the mass of a hydrogen atom and n_H is the hydrogen number density. The density distribution in the cloud is given as $n_H = A_c \tanh(\frac{r-r_c}{20\,\mathrm{pc}}) + B_c$, where $A_c = -0.5(n_{H,C} - n_{H,A})$ and $B_c = 0.5(n_{H,C} + n_{H,A})$, and $n_{H,C}$ and $n_{H,A}$ are the hydrogen number densities of the cloud and ambient medium, respectively. The temperature of each cloud is set so as to enable pressure balance with the surrounding gas at the beginning of each simulation. Owing to the variation in cloud density from one simulation to the next, the initial cloud temperatures range from 210 to 1040 K at the center of the cloud. Like in Galyardt & Shelton (2016), we assume that the cloud originates in intergalactic space, where the metal abundance is very low. In order to trace the cloud gas as it interacts with the Galaxy, we set the initial cloud metal abundance to $1 \times 10^{-5} Z_{\odot}$.

The dark matter minihalo density profile is identical for all simulations and is taken from Galyardt & Shelton (2016). The dark matter minihalo is modeled as an Einasto profile (Einasto, 1965; Merritt et al., 2006): $\rho(r) = \rho_e \exp\{-d_n[(r/r_e)^{1/n} - 1]\}$, where ρ_e defines the nominal density, r_e defines the half-mass radius for an infinite dark matter distribution, n defines the 'shape' of the distribution, and $d_n \approx 3n - 1/3 + 0.0079/n$, for $n \gtrsim 0.5$ (Merritt et al., 2006). For the minihalos used in this work, we use $r_e = 1.0$ kpc, n = 1/0.17, and $\rho_e = 9.79 \times 10^{-3} \,\mathrm{M}_{\odot}\,\mathrm{pc}^{-3}$. The dark matter distribution is spherically symmetric with a radius of 2 kpc. The total mass of our dark matter minihalo (3.0 \times 10⁸ M $_{\odot}$) matches that of Nichols et al. (2014), but their simulations used a Navarro–Frenk–White profile (see Navarro et al. (1996)). Tepper-García & Bland-Hawthorn (2018) also used a Navarro–Frenk–White profile for their dark matter minihalo, but with masses of 10^8 and 10^9 M $_{\odot}$.

For these simulations, we use FLASH version 4.3, which is an update relative to version 4.2 which was used for Galyardt & Shelton (2016). In both projects, the FLASH calculations use the unsplit staggered mesh ideal MHD solver for simulations that include a magnetic field and use the unsplit solver for

simulations that did not model a magnetic field. In all cases, the adiabatic ideal gas equation of state is modeled, using an adiabatic index, γ , of 5/3. Radiative cooling is not modeled. The gravity unit in version 4.3 of FLASH is updated relative to that used in Galyardt & Shelton (2016), but it continues to use the Barnes-Hut Tree Solver to calculate self gravity between material within the domain. As in Galyardt & Shelton (2016), the gravity field due to the mass of the entire galaxy was calculated externally using the method described in that paper. The vertical component of the Galaxy's gravitational field was uploaded into FLASH and used in our simulations. The portion of the disk that is within the simulational domain contributes to both the Galaxy's gravitational field and to self gravity, but this double-counting is not expected to have significant effects on the results.

We ran 11 simulations, labeled Run Lo, Mo to M5, and Ro to R5 in Table 3.2. Three simulations (Runs Lo, Mo, and Ro) do not include a baryonic cloud, while the other 8 simulations do. In Runs M1 and R1, the cloud's initial hydrogen number density is 0.1 cm⁻³, while it is 0.2 cm⁻³ in Runs M2 and R2, 0.4 cm⁻³ in Runs M4 and R4, and 0.5 cm⁻³ in Runs M5 and R5. Runs M0 through M5 include a Galactic magnetic field, while Runs Lo and R0 to R5 do not. As stated previously, all simulations include a dark matter minihalo of mass $3 \times 10^8 \, \mathrm{M}_{\odot}$.

One topic of interest is the fate of the cloud material. We trace the cloud material by its metallicity. We determine the average location of the material that came from the original cloud by first calculating the mass of cloud material in each cell, using the cloud fraction defined in Section 3.3.2, and then calculating the center of mass of such material.

A second topic of interest concerns the material that moves with the dark matter minihalo. In order to identify this material, we find the gas that is within 1.0 kpc of the minihalo center of mass and whose \hat{z} component of velocity is within 50 km s⁻¹ of that of the minihalo center of mass.

Table 3.1: Simulation Parameters. Note that initial cloud density, presence of the Galactic magnetic field, and minimum cell size vary between the runs. Table 3.2 shows the chosen parameters for individual simulations.

Parameter	Size		
Gas cloud radius	500 pc		
Gas cloud H density	o, o.i, o.2, o.4, or o.5 $\rm H cm^{-3}$		
Gas cloud mass	o, i.7 $\times 10^6$, 3.3 $\times 10^6$, 6.6 $\times 10^6$, or 8.3 $\times 10^6 \mathrm{M}_\odot$		
Gas cloud metal abundance	$10^{-5}Z_{\odot}$		
Dark matter minihalo mass	$3.0 imes 10^8 \mathrm{M}_{\odot}$		
Initial location of cloud and minihalo	x = 0 kpc, $y = 0$ kpc, $z = 10$ kpc		
Initial velocity of cloud and minihalo	-200 km s $^{-1}$ \hat{z}		
Galactic metal abundance	o.3 Z_{\odot}		
Galactic magnetic field	Coherent component of Jansson & Farrar (2012a) or None		
Coordinate system	Cartesian		
Domain size	$4 \text{ kpc} \times 4 \text{ kpc} \times 24 \text{ kpc}$		
Minimum cell size	15.6 pc or 7.8 pc		

Table 3.2: Set of Simulations.

Simulation Name	Cloud H Density (H cm ⁻³)	Galactic Magnetic Field	Minimum Cell Size (pc)	Duration (Myr)
Lo	О	no	15.6	160
Mo	О	yes	15.6	160
$M_{\rm I}$	0.1	yes	15.6	160
M2	0.2	yes	15.6	150
M_4	0.4	yes	15.6	159
M5	0.5	yes	15.6	160
Ro	0	no	7.8	86
Rı	O.I	no	7.8	160
R2	0.2	no	7.8	162
R4	0.4	no	7.8	153
R5	0.5	no	7.8	160

3.3 Results

3.3.1 Cloud-free Minihalo Evolution

In order to determine if dark matter minihalos, alone, are able to gravitationally accrete gas from the halo and disk, we performed Runs Lo, Mo, and Ro. Each of these runs has a dark matter minihalo but no accompanying baryonic cloud. The minihalos in all three of these simulations do not accrete any gas as they pass through the halo prior to interacting with the Galactic disk. The dark matter minihalos temporarily affect the disk. As each minihalo passes through the disk, it pulls disk gas towards it, resulting in a pileup of gas along its path through the disk. Despite causing local distortions in the disk, the minihalo does not accrete any disk gas during its passage. See Figure 3.1.

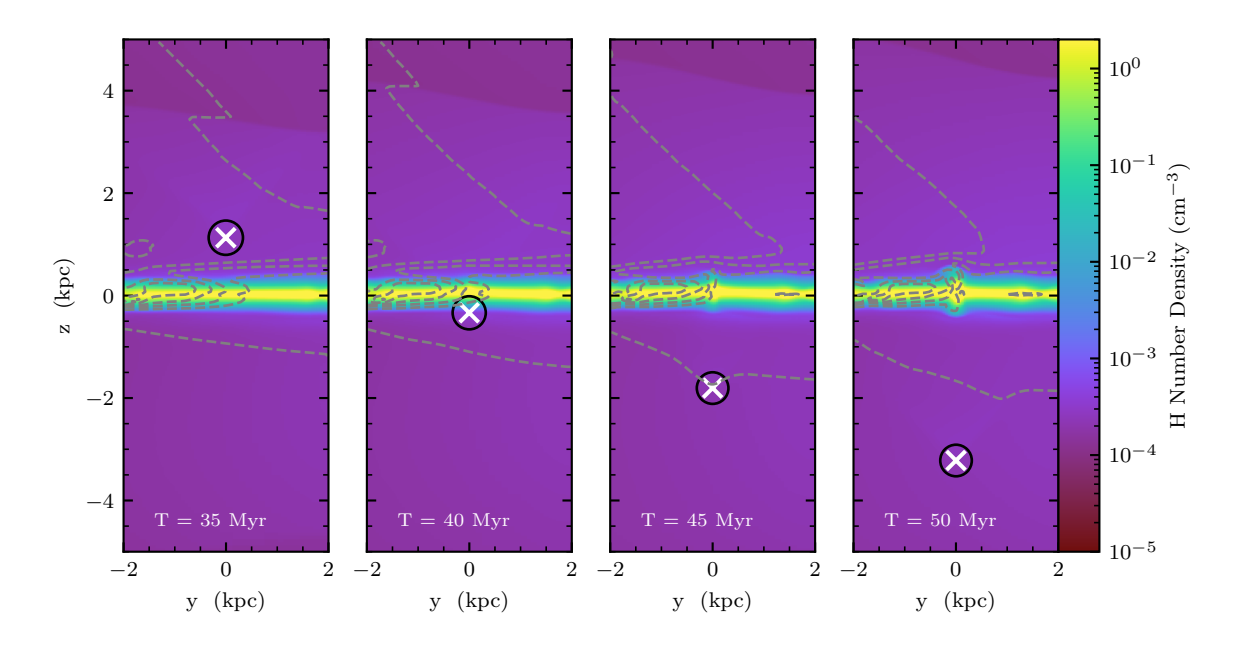


Figure 3.1: Hydrogen number densities for Run Mo at 4 epochs (35, 40, 45, and 50 Myr) along a vertical slice in the x=0 plane through the central portion of the domain. The white \times and black circle represent the center of mass and half-mass radius of the dark matter minihalo, respectively. The contours depict the magnetic field strength. This figure shows that the dark matter minihalo does not accrete gas during its passage through the disk.

3.3.2 Cloud Evolution

Runs M1-M5 and R1-R5 add a gaseous component to the dark matter cloud. This change has very little effect before the collision with the disk, but has enormous effects during and after the collision. Figure 3.2 shows the evolution of an example simulation.

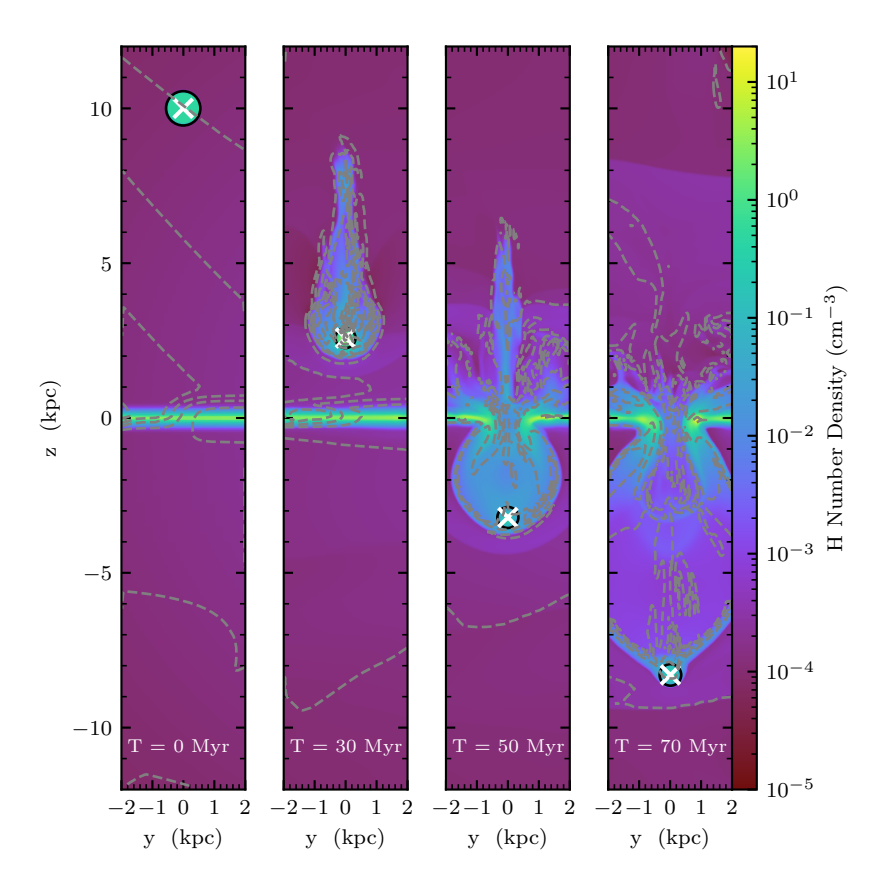


Figure 3.2: Hydrogen number densities for Run M5 at 4 epochs (0, 30, 50, and 70 Myr) along a vertical slice in the x=0 plane. The white \times and black circle represent the center of mass and half-mass radius of the dark matter minihalo, respectively. The contours depict the magnetic field strength.

Galyardt & Shelton (2016) gave an overview of the dynamics of this system. Here we extend their analysis. The gaseous cloud moves together with the dark matter minihalo until shortly before the collision with the Galactic disk. This is shown by the small distances between cloud and minihalo centers of mass (Figure 3.3, top panel), and the similarity in the bulk \hat{z} -velocities between all of the clouds and

their minihalo escorts for times prior to \sim 30 Myr (Figure 3.3, bottom panel; the minihalo center of mass v_z is shown as an orange curve). In the last few million years before the collision, the clouds begin to encounter the increased ambient density near the Galactic disk, which begins to slow them down relative to the dark matter minihalos. This slowing is demonstrated by both the widening gaps and the increasing velocity differences between the dark matter minihalos and the gaseous clouds (top and bottom panels of Figure 3.3).

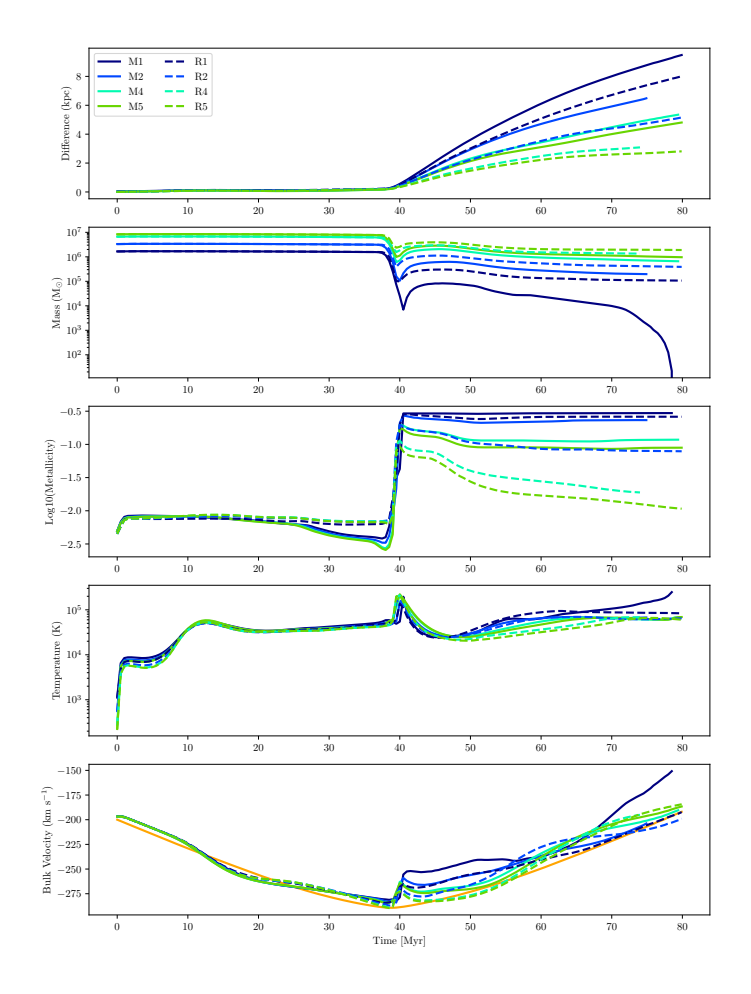


Figure 3.3: Top panel: Physical distance between dark matter minihalo center of mass and cloud center of mass as a function of time. Second panel: Total mass of the cloud material moving with the dark matter minihalo, based on the criteria set forth in Section 4.2. Henceforth, this material is referred to as the cloud. Third panel: Metallicity of the cloud. Fourth panel: Temperature of the cloud. Fifth panel: Bulk velocity of the cloud. The orange curve shows the velocity of the dark matter minihalo.

From roughly 37 to 41 Myr, the dark matter minihalos pass freely through the disk. As they approach the midplane, the gravitational acceleration decreases. As they cross the midplane, the gravitational acceleration increases, but in the positive \hat{z} direction. Consequently, the minihalos move fastest as they cross the midplane. Their velocities follow the expected parabolic evolution (see the orange curve in Figure 3.3, bottom panel). Conversely, the gas clouds feel the ram pressure of the disk, causing them to decelerate more substantially. As a result, the gaseous clouds cannot keep up with their dark matter minihalos during this time frame. This causes the sudden drop in cloud mass (second panel of Figure 3.3) and uptick in the relative distance between the gas clouds and their dark matter minihalos at roughly 40 Myr (top panel of Figure 3.3).

The hydrodynamics of the cloud collision make this case different from the case described in Section 3.3.1. The ram pressure of the gas cloud displaces the Milky Way gas. The gravitational pull of the minihalo contributes to the motion. The affected gas is substantially accelerated, enabling it to be captured by the dark matter minihalo or at least meet the criteria for cloud material accompanying the subhalo described in Section 4.2.

This ability to displace and attract the disk gas raises the question of how much disk gas is enmeshed in the post-collision cloud. This question can be quantitatively answered by examining the metal abundances of the post-collision material. The metal abundance in any given cell (Z) is the mass-weighted sum of the metal abundance of the original cloud (Z_c) and the metal abundance of the ambient Milky Way gas (Z_a): $Z = f_c Z_c + f_a Z_a$, where f_c is the fraction of material in the cell that came from the cloud and f_a is the fraction of material in the cell that came from the ambient Milky Way gas (Gritton et al., 2014). The sum of these fractions must always be 1. Solving these two equations yields the fraction of material in a cell that came from the cloud:

$$f_c = \frac{Z - Z_a}{Z_c - Z_a}. (3.1)$$

Figure 3.3 (third panel) shows the time evolution of the cloud's metallicity, where metallicity refers to $\log\left(\frac{Z}{Z_{\odot}}\right)$ and cloud refers to the gaseous material accompanying the dark matter minihalo. In the first 35 Myr, the cloud's metallicity drops slightly from -2.3 to -2.4 for runs M1-M5 and rises slightly from -2.3

to -2.2 for the runs R1-R5. Then, as the dark matter minihalo passes through the disk, the metallicity of the gaseous material accompanying it quickly rises to between -1.0 and -0.5, depending on the simulation. In the most extreme case (M1), the post-collision cloud is almost entirely comprised of Milky Way gas. In the least extreme case (R5), the post-collision cloud is roughly a third Milky Way gas.

Clouds with larger initial densities conduct more gas through the Galactic disk than do clouds with smaller initial densities, as shown by the metallicity trends at 50 Myr in panel 3 of Figure 3.3. For each set of runs, the relative mixture of original cloud material to entrained material increases monotonically with the initial density of the progenitor cloud. See Table 3.3 for the fraction of the progenitor that remained in the cloud, the ratio of accreted material to surviving progenitor material, and the ratio of the cloud mass to the initial cloud mass at 50 Myr. The cloud mass used in Table 3.3 is that of the material that moves with the dark matter minihalo, based on the criteria set forth in Section 4.2. These mixtures are the result of multiple processes: the stripping of progenitor cloud material from the minihalo and the displacement of Milky Way gas and its attraction to the dark matter minihalo. The loss of progenitor gas is so significant that no more than 35% of the low–metallicity progenitor cloud mass survives the collision (see Table 3.3). In all, by 50 Myr the mass of surviving progenitor gas plus entrained gas drops to roughly 4 - 38% of the original progenitor cloud mass (see Table 3.3 and Figure 3.3, second panel) during the collision with the disk. The mass loss depends on the initial density of the cloud; less dense clouds are more eroded by passage through the disk.

By 70 Myr, the mass of surviving progenitor gas plus entrained gas drops further, to roughly 1 - 24% of the original progenitor mass (see Table 3.4). This is due to both accreted gas and progenitor cloud gas being stripped from the dark matter minihalo as it moves away from the disk.

The progenitor material mildly lags the dark matter minihalo before passing through the disk and substantially lags it after passing through the disk (see Figure 3.3, top panel). The lag is strongest for the lowest density clouds and weakest for the highest density clouds. The separation is also larger for the M series of simulations than the R series of simulations. As a consequence of the lag, the metallicity of the gas in the vicinity of the minihalo rises towards that of the Milky Way. This is shown by the metallicity of the gas located within 100 pc of the dark matter minihalo center of mass (see Figure 3.4). We used a 100 pc

Table 3.3: Fate of the progenitor cloud. The second column is the ratio of surviving progenitor cloud mass in the post-collision cloud to the original progenitor cloud mass. The third column is the ratio of accreted material to surviving progenitor material in the post-collision cloud. The fourth column is the ratio of post-collision cloud mass to original progenitor cloud mass. The tabulated results are for 50 Myr.

Simulation	Progenitor Survival	Accreted/Surviving	Overall Mass Retention
Mı	0.001	27.73	0.04
M ₂	0.05	2.55	0.16
M4	0.15	0.64	0.24
M5	0.18	0.44	0.26
Rı	0.03	4.27	0.16
R ₂	0.17	0.56	0.27
R ₄	0.31	0.15	0.35
R ₅	0.35	0.10	0.38

Table 3.4: Same as Table 3.3 but for 70 Myr.

Simulation	Progenitor Survival	Accreted/Surviving	Overall Mass Retention
Mı	0.0001	68.45	0.01
M ₂	0.01	3.42	0.06
M4	0.07	0.61	0.12
M5	0.10	0.40	0.14
Rı	10.0	6.77	0.07
R ₂	0.10	0.37	0.13
R ₄	0.20	0.07	0.21
R ₅	0.23	0.05	0.24

radius to order to isolate material moving with the dark matter minihalo while minimizing contamination from other gas. Bow shock gas is not within this radius.

In general, the gas captured by the minihalo continues to track the dark matter center of mass in position and velocity. By 50 Myr, this captured gas is well-separated from the disk (see Figure 3.5, upper left panel) and continues on its trajectory away from the disk at high velocity (Figure 3.5, lower left panel). However, this captured gas soon begins to lag behind the dark matter minihalo. Figure 3.3 shows the lag.

Run M1 is the most extreme case. By 70 Myr, the gravitationally attracted cloud for M1 is much farther behind the dark matter minihalo than are the gravitationally attracted clouds for other runs. Furthermore, Run M1 does not exhibit a density enhancement above the mean density of the surrounding medium at

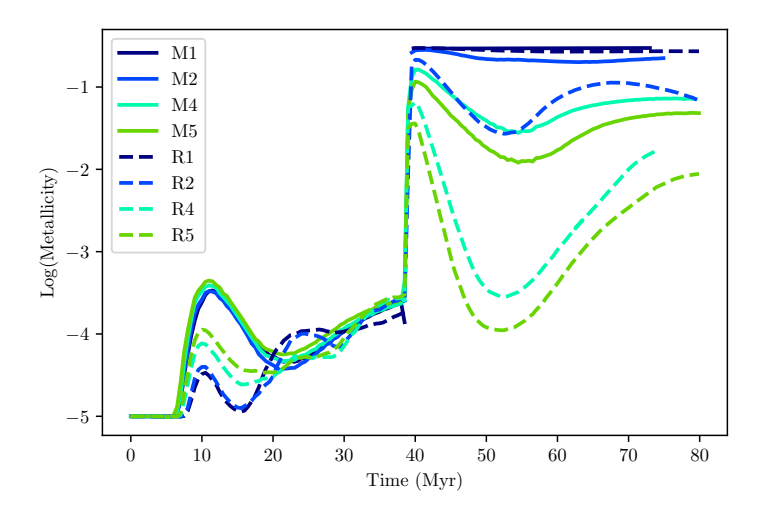


Figure 3.4: Average metallicity of the gas found within 100 pc of the dark matter minihalo center of mass.

the location of the minihalo, confirming that the dark matter minihalo has outpaced the gravitationally attracted cloud.

In general, after moving through the disk, the progenitor material slowly expands, falls farther behind the dark matter minihalo, and merges with the bubble. The bubble is described more extensively in Section 3.3.3.

3.3.3 Splashes and Bubbles

Figures 3.7, 3.8, and 3.9 show the profiles of several simulation variables versus z at 30, 50, and 70 Myr, respectively. The plots show all of the gas in the domain; no selection has been applied to the gas prior to profile generation. In each figure, the panels display (clockwise from upper left) cell mass—weighted profiles of the hydrogen number density, metallicity, temperature, and velocity along the \hat{z} axis. Each quantity is averaged across thin slabs in the x–y plane at each value of z. The z position of the minihalo is shown as a black vertical line in each panel, with gray shading representing the half–mass radius of the dark matter minihalo. In the velocity panels of each figure, the velocity of the minihalo is indicated by a

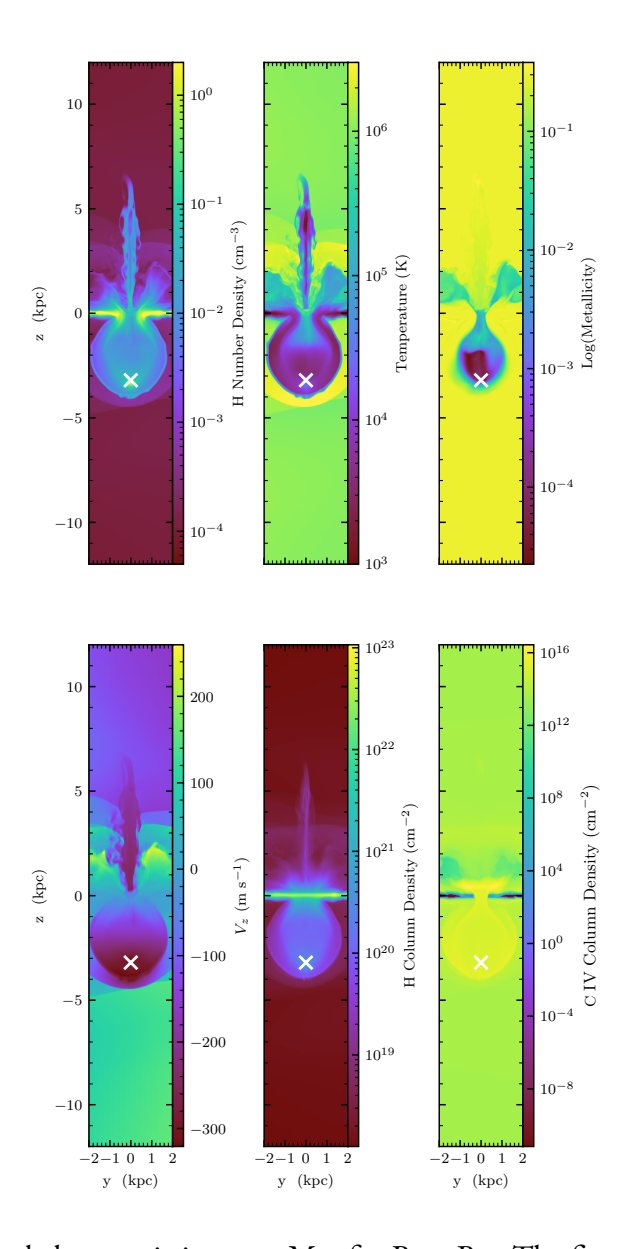


Figure 3.5: Plots of physical characteristics at 50 Myr for Run R5. The first four plots show hydrogen number density, temperature, metallicity, and \hat{z} velocity along a vertical slice in the x=0 plane. The last two plots show the hydrogen column density and C IV column density.

horizontal orange line. The minihalo trajectory is nearly identical for all runs with a gaseous cloud, with negligible differences due to gravitational interactions with the local gas. On the other hand, individual clouds evolve noticeably differently, depending on their initial hydrogen density.

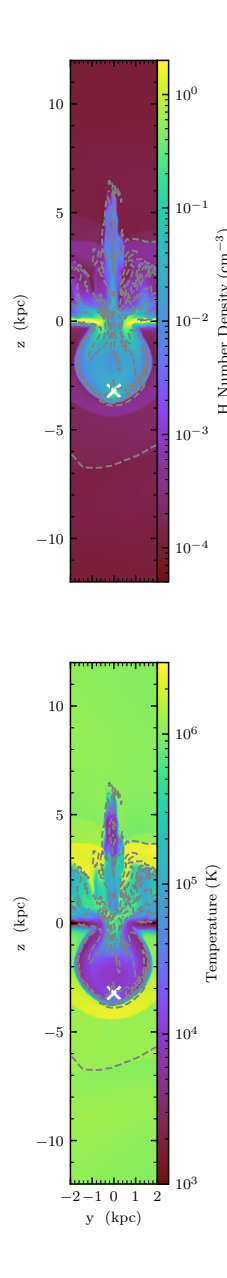


Figure 3.6: Hydrogen number density and temperature along a vertical slice in the x=0 plane at 50 Myr for Run M5. The contours depict the magnetic field strength. In comparison with Figure 3.5, Run M5 creates slightly smaller and warmer bubbles.

All of the runs evolve similarly until the collision with the disk at 37 Myr. Figure 3.7 shows the evolution at 30 Myr. The hydrogen number density profile (upper left panel) shows two prominent peaks: the peak at z = 0 kpc is the Galactic disk, while the peak at roughly z = 2.5 kpc coincides with the head of the cloud. The cloud density peak is aligned with the dark matter minihalo center of mass, represented by the solid

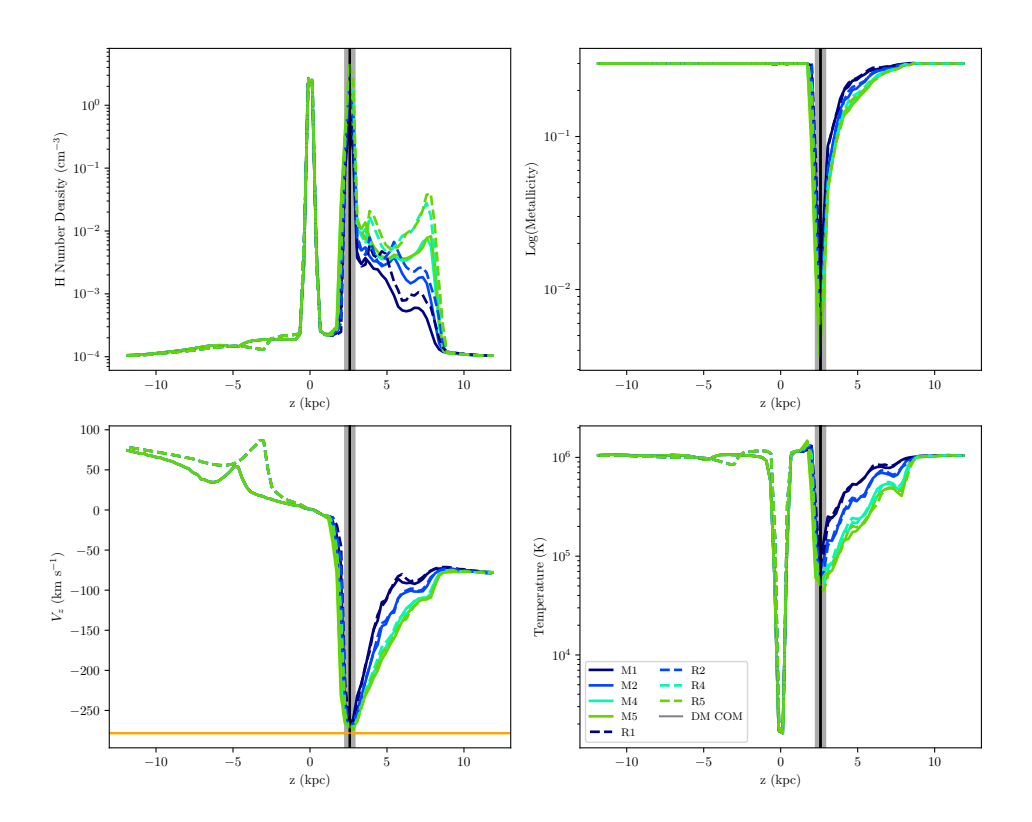


Figure 3.7: Clockwise from the upper left, the plots show the average hydrogen number density, metallicity, temperature, and velocity in the \hat{z} direction as functions of z at 30 Myr. The cloud is still ~ 2.5 kpc above the disk and will collide at 37 Myr.

black vertical line. The cloud tail material extends from z = 2.5 kpc to about 9 kpc. At this epoch, the progenitor material, traced by low–metallicity gas, is confined to the cloud and its tail (Figure 3.7, upper right panel), the cloud and the Galactic disk are the coolest features of the domain (lower right panel), and the mean gas velocity at the z position of the cloud head is consistent with the minihalo velocity (Figure 3.7, lower left panel; the minihalo velocity is marked by the horizontal orange line).

When the clouds collide with the disk at about 37 Myr, the impact shock—heats a thin layer of disk gas at the impact site and creates a large pressure gradient that fragments the clouds. The pressure gradient induced by the impact is so large that it accelerates a significant amount of cloud and disk gas upwards, to heights above the disk. The lower left panel of Figure 3.8 shows that the gas within 4 kpc above the midplane has been accelerated upwards to speeds approaching 100 km s^{-1} . The backsplash is obvious

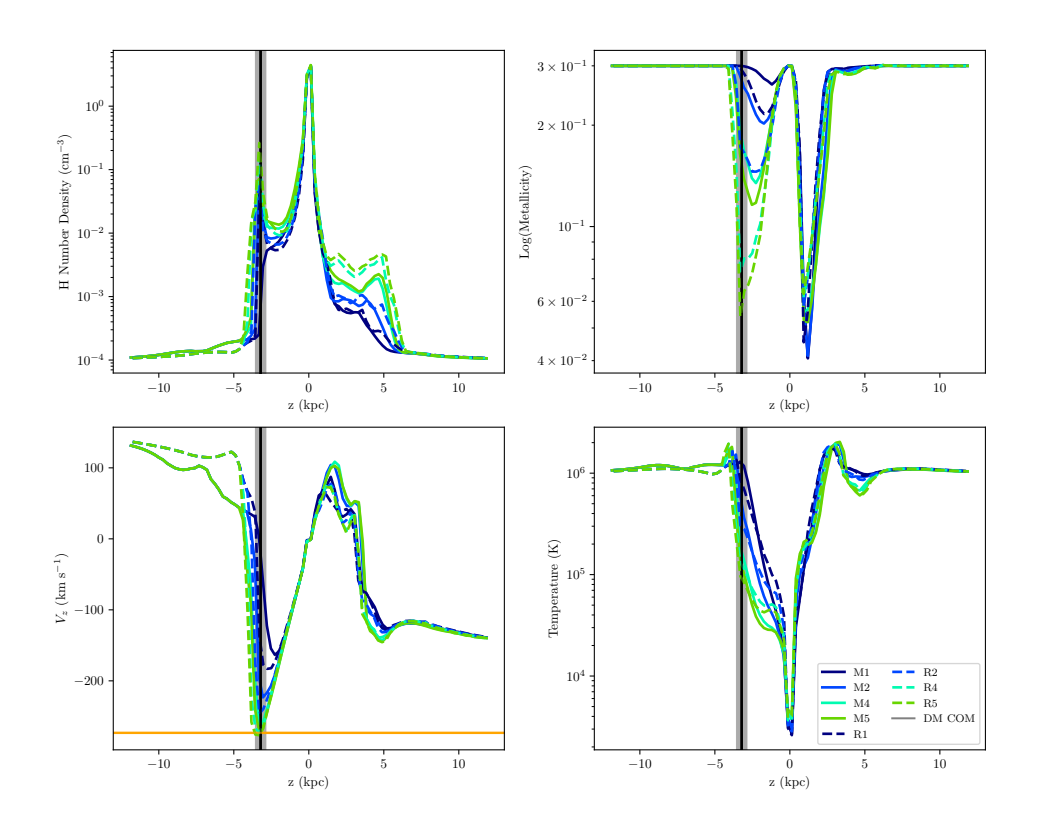


Figure 3.8: Same as Figure 3.7, but for 50 Myr.

in slice plots of the 50 Myr epoch, shown for Run R5 in Figure 3.5. This recoiling gas has a lower mean metallicity than the Galactic gas, indicating that its composition includes gas from both the initial cloud and Galactic sources. In fact, for the lower density runs, the majority of the low–metallicity gas is in the recoil, above the disk midplane. The impact-induced pressure gradient also transfers momentum from the cloud to the disk gas, fomenting an expanding bubble structure below the disk. Since most of the cloud and disk gas is cool, the interior of the collision-induced bubble structure is also cool. The shell of the bubble is hotter, as it is shock—heated (see Figure 3.5). At late times, an extended hole develops in the center of the bubble.

The bubbles are slightly smaller and warmer in the M series simulations than in the R series simulations (see Figure 3.6). The difference could be due to the magnetic field, difference in resolution, or both. For both the M series and R series of simulations, the bubble has a mass-weighted average temperature of $\sim 10^4$ to $\sim 10^5$ K, is traced by C III, C IV, and C V, and has an average hydrogen column density of

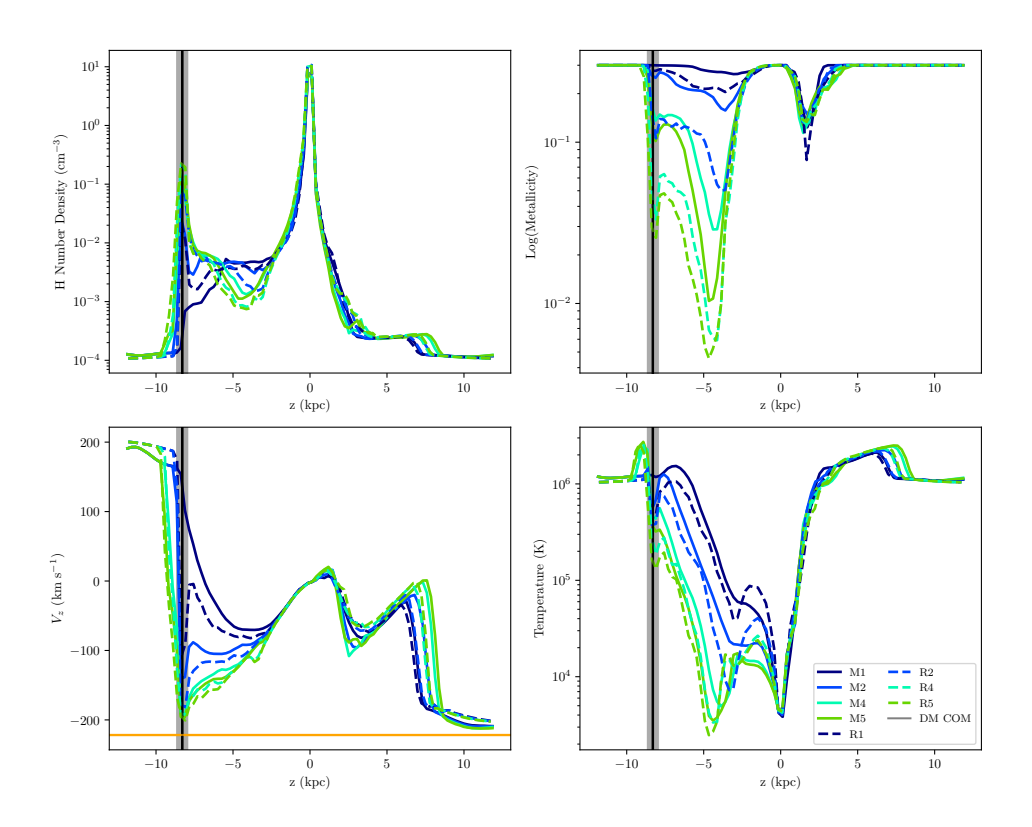


Figure 3.9: Same as Figure 3.7, but for 70 Myr.

 $10^{19.6}$ to $10^{20.3}$ cm⁻², from 45 to 75 Myr. Another factor driving the morphology is the presence of the dark matter minihalo. The simulations of Galyardt & Shelton (2016) show that the presence of a dark matter minihalo accompanying a baryonic cloud results in a larger bubble than those created by baryonic clouds alone.

Low-metallicity gas from the tail of the pre-collision cloud continues to fall through the collision-induced hole in the disk between 50 and 70 Myr, further reducing the mean metallicity of the bubble region (Figure 3.9, upper right panel, upper left panel). By 70 Myr, the majority of the low-metallicity gas has accumulated in the bubble structures of all runs except M1 (Figure 3.9, upper right panel). This inflow of cool progenitor cloud gas into the bubble structure along with the expansion of this structure further lowers its temperature (Figure 3.9, lower right panel). The coolest gas in the bubble has a temperature of ~ 700 K. Due to the low relative velocity between the bubble's shell and minihalo, some of the shell gas

is captured by the minihalo. This is confirmed by the poorly ionized but metal-rich gas coincident with the dark matter subhalo.

3.3.4 Holes

At the beginning of the simulation, the average H column density of the disk is $10^{21.1}$ atoms cm $^{-2}$. The initial H column density is determined by counting only gas whose $|v_z| \leq 10$ m s $^{-1}$ and whose temperature is less than 6.0×10^5 K. As each simulated gas cloud collides with and passes through the Galactic disk, it creates a hole in the disk. Figures 3.10 and 3.11 show the holes in the Runs M5 and R5 disks after the clouds have finished passing through the disk. These figures show the column densities along vertical sight lines through the disk (defined here as material whose \hat{z} velocity is -50 km s $^{-1}$ to 100 km s $^{-1}$ and whose temperature is less than 5.0×10^5 K) at 40, 50, and 70 Myr. The white regions represent places in the disk where the vertical column density is less than 1/100th of the initial column density of the disk. Each hole is largest immediately following the impact. Subsequently, the hole shrinks in size as the disk heals from the impact.

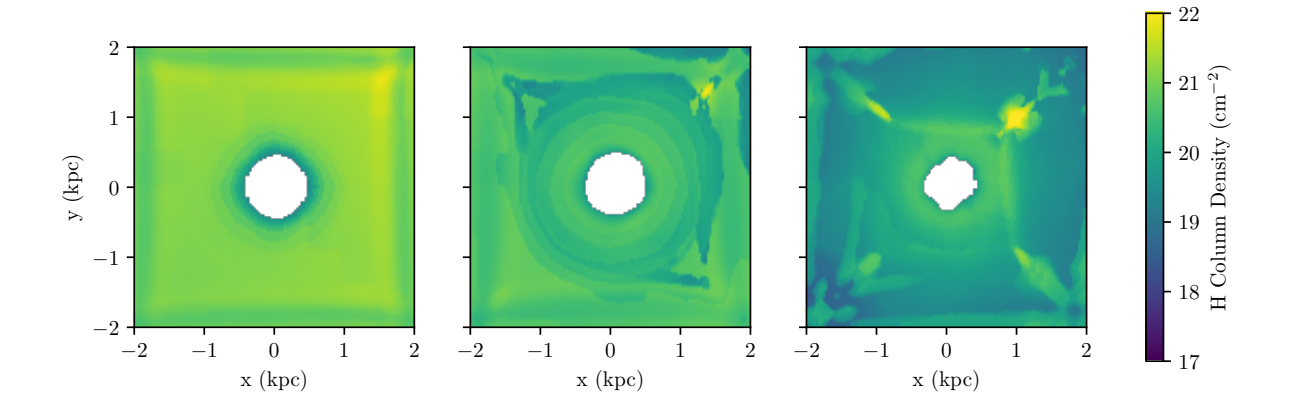


Figure 3.10: Disk hydrogen column densities for Run M5 from a face on view of the disk at 40, 50, and 70 Myr. The halo and cloud material are not shown in these panels. The first panel is shortly after the cloud hit the disk (which occurred at 37 Myr) and the hole was formed. The later panels show that the hole in the disk decreases in size as time goes by.

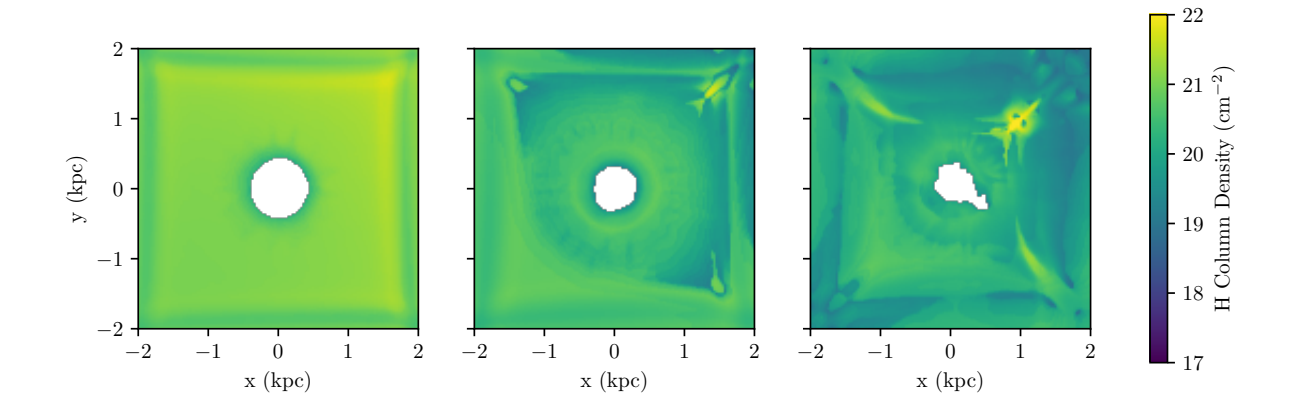


Figure 3.11: Same as Figure 3.10 but for Run R5.

The unusual square-shaped structure seen in these figures is due to waves traveling through the domain. They already exist near the edges of the domain at 40 Myr, as seen in the left panels of Figures 3.9 and 3.10. These waves bounce off of the domain boundaries and move towards the center. As the right panels show, by 70 Myr the waves have not yet reached the center of the disk, so they do not affect the hole.

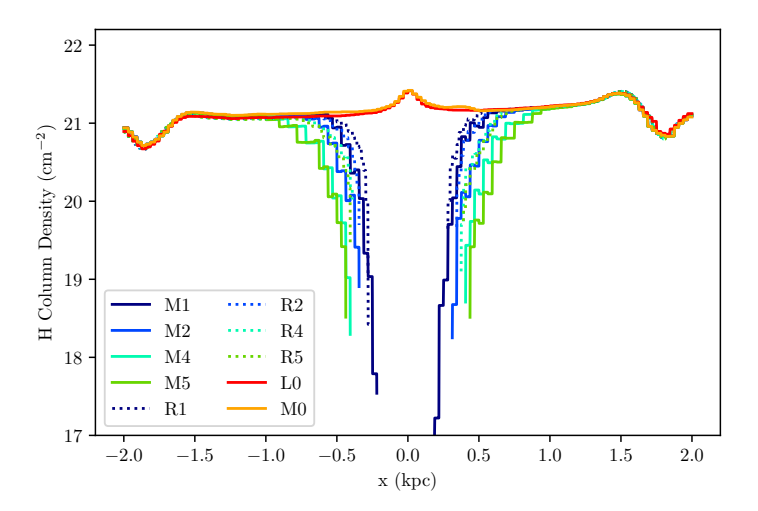


Figure 3.12: Hydrogen column density along vertical sight lines through the disk at y=0 kpc and various values of x are shown for Runs Lo, Mo-M5, and R1-R5 at 40 Myr. The holes in Runs M1-M5 and R1-R5 can be identified by the precipitous drop in column density near x=0 kpc. Their sizes depend on both the density of the cloud and the presence of a magnetic field. The dark matter minihalos in Runs Lo and Mo pull disk gas inwards, creating the pileups of disk gas at x=0 kpc. These runs only contain dark matter clouds, which our simulations find incapable of creating holes.

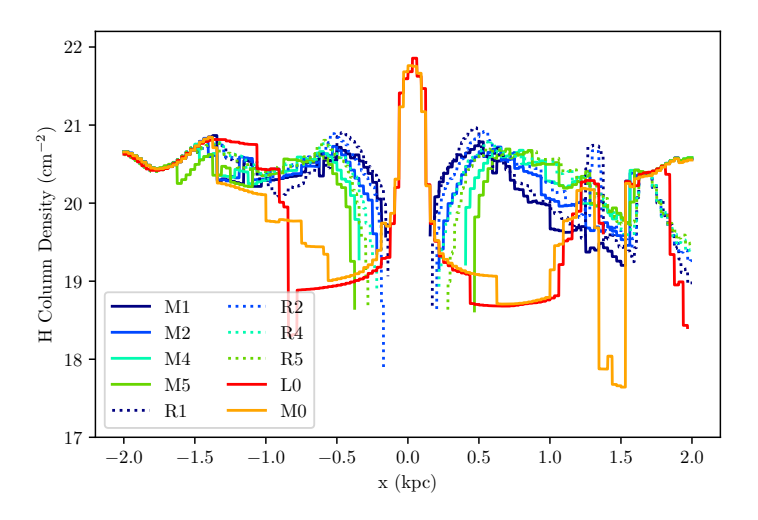


Figure 3.13: Same as Figure 3.12 but for 50 Myr.

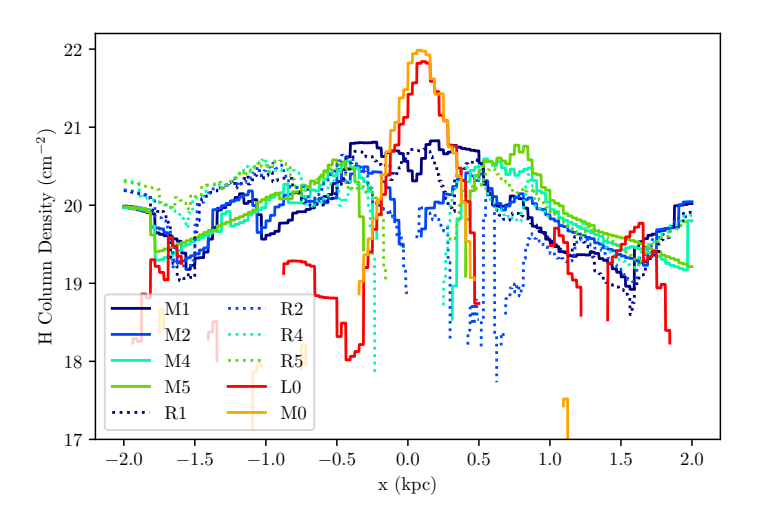


Figure 3.14: Same as Figure 3.12 but at 70 Myr. The holes still exist at 70 Myr in the higher density cloud simulations, but have already healed in the lower density cloud simulations. For runs Lo and Mo, the pileup of disk gas at the center of the disk grows over time, creating the large peaks.

The densest clouds in our set of simulations create the most pronounced holes. Figures 3.12, 3.13, and 3.14 show the disk's density profile at 40, 50 and 70 Myr. The denser clouds produce more prominent and longer-lived holes. Table 3.5 lists the dimensions of the holes for each simulation at these three epochs. For each simulation, the holes decrease in size over time. For the lowest density runs, the holes have healed by 70 Myr.

The largest of these holes can exceed 400 pc in radius. Holes of this size can be seen by observers with high resolution telescopes. For example, a 400 pc radius hole in a galaxy 800 Mpc away would have an angular diameter of 0.2 arcseconds, which is much larger than the angular resolution of the Very Large Baseline Array of 0.11 - 22 milliarcseconds².

3.4 Discussion

What happens if HVCs reside within dark matter envelopes (Blitz et al., 1999; Braun & Burton, 2000; Simon et al., 2006; Nichols & Bland-Hawthorn, 2009; Tepper-García & Bland-Hawthorn, 2018)? Many

²See https://public.nrao.edu/telescopes/vlba/

Table 3.5: Dimensions and area of the holes formed for each run. Blank rows signify epochs where a hole was not present. Dimensions are given as the maximum extent of the hole in each direction.

Run	Epoch	Dimensions (pc)	Area (kpc²)
Lo	40	-	-
	50	-	-
	70	-	-
Mo	40	-	-
	50	-	-
	70	-	-
Mı	40	560.8 × 530.4	0.23
	50	343.2 × 311.2	0.13
	70	-	-
M ₂	40	687.2 × 716.8	0.362
	50	467.2 × 467.2	0.175
	70	248.8 × 280.0	0.044
M4	40	842.4 × 843.2	0.532
	50	748.8 × 717.6	0.424
	70	592.0 × 624.0	0.275
M5	40	874.4 × 874.4	0.591
	50	843.2×843.2	0.568
	70	717.6×748.8	0.371
Rı	40	560.8 × 560.8	0.234
	50	327.2 × 311.2	0.073
	70	-	-
R ₂	40	685.6 × 670.4	0.352
	50	389.6 × 389.6	0.112
	70	217.6 × 201.6	0.021
R ₄	40	764.0 × 764.8	0.456
	50	486.0 × 484.0	0.174
	70	570.4 × 483.2	0.164
R ₅	40	795.2 × 795.2	0.492
	50	608.8×608.8	0.280
	70	608.0 × 764.8	0.237

of these clouds will eventually hit galaxies. This scenario raises the specter of the cloud's destruction during the impact. Galyardt & Shelton (2016) found that the clouds were scattered upon impact, but their study also found gas accompanying the dark matter minihalo 40 Myr after impact. Here, we determine the origin of that gas. This work also answers several ancillary questions. One question is the fate of the HVC material. Another question whether the Smith Cloud has previously passed through the Galactic disk. A third question is whether a dark matter minihalo with a negligible baryonic component can gather and confine gas gravitationally as it passes through a galactic halo and disk. A final question asks for the characteristics of the collision-induced holes and bubbles.

Regarding the fate of HVC gas after the collision, the simulations presented here confirm the conclusion of Galyardt & Shelton (2016) that an infalling dark matter minihalo with a bound gaseous component will only carry a small fraction of its original gas away from a collision with the outer Galactic disk. This result applies to clouds with masses between $10^6~M_\odot$ and $10^7~M_\odot$. As the mass of the progenitor cloud increases, the percentage of surviving gas increases, so clouds with initial masses orders of magnitude higher than our clouds may carry a more significant percentage of their original gas. The vast majority of the progenitor HVC gas is decellerated by the collision, and later becomes part of the bubble structure below the disk and the splash above the disk. In the case that the progenitor cloud had low density, it tends to bounce off the disk and become part of the splash, whereas in the case of a high density progenitor cloud, most of the material moves through the disk. In each case, roughly one third of the progenitor mass goes into creating the bubble. This fraction grows over time as material from the splash subsequently falls through the hole in the disk. All of the gas that is not bound to the minihalo will eventually fall back onto the disk, since neither the recoil gas nor the bubble gas are pressure supported against gravity.

Various studies (Tenorio-Tagle et al., 1986; Galyardt & Shelton, 2016; Tepper-García & Bland-Hawthorn, 2018) have shown that infalling HVCs with no dark matter component contribute all of their gas to the Galactic disk after the initial impact response is damped out by gravity. Our simulations indicate that a dark matter component of an HVC would only make a small correction to this result. HVC infall represents an efficient mechanism for contributing fresh fuel for star formation to the Galaxy (Wakker et al., 1999; Lehner et al., 2012). Of course, if star formation were initiated by the initial impact (Bekki,

2009; Kannan et al., 2012; Shah et al., 2019) or subsequent evolution of the bubble or recoil structures, a stellar wind generated by newly formed stars may support a portion of these out-of-plane gas structures, increasing the time needed for cooling and subsequent gravitational collapse.

We next consider the hypothesis that the Smith Cloud is left over from a previous collision between an extragalactic HVC and the Galactic disk. An intergalactic cloud would be expected to have a very low metallicity. In contrast, the Smith Cloud metallicity (head: 0.15 – 0.44 Z_{\odot} Hill et al. (2009); tail: 0.53 Z_{\odot} Fox et al. (2016)) is similar to the outer disk of the Milky Way. Although our simulations show that the clouds exchange material with the Milky Way as they pass through it, only the low-density clouds exchange enough material for their metallicities to be similar to their surroundings. Among our simulations, only those with initial hydrogen number densities of \leq 0.2 cm⁻³ create post–collision clouds whose metallicities are comparable to the ambient metallicity. However, our simulations also show that such low-density clouds have difficulty passing through the disk. Therefore, it would be unlikely for such a low-density cloud to retain enough mass to explain the currently–observed mass of the Smith Cloud. Moderating these effects is that the magnetic field in our simulations does not include the random components described in Jansson & Farrar (2012b) and so a more realistic magnetic field would have stronger effects than our simulations show. For a given cloud initial density, raising the magnetic field would likely cause the post–collision clouds to be less massive and have more disk–like metallicities. This would likely allow for a somewhat denser, more massive progenitor cloud.

Regarding the question of whether a cloud-free dark matter minihalo can capture gas from the disk, in our simulations no disk gas was captured by the minihalo. The chief hinderance to gas accretion is the large relative velocity between the minihalo and the disk gas. An oblique trajectory aligned with rotation of the Galactic disk may reduce the relative velocity, perhaps making disk gas capture a low probability event.

Such gas free dark matter minihalos may exist near disk galaxies, as intergalactic interlopers, leftovers from the galaxies' formation via dark matter aggregation, or infalling dwarf galaxies stripped of their gas but still orbiting the Galaxy. Our simulations show that when the minihalo is quite close to the disk, the disk gas responds gravitationally. The simulations of Bekki (2009), Kannan et al. (2012), and Shah et al.

(2019) also show a localized gravitational interaction. In our simulations, the disturbed disk gas does not reach escape velocity, and so does not move with the dark matter minihalo as the minihalo leaves the disk.

A connection between galactic holes and HVCs has been suggested by many authors. Pokhrel et al. (2020) observed 306 H I holes in 41 gas-rich dwarf galaxies. They suggested various mechanisms for the formation of these holes, HVCs being one. Tenorio-Tagle (1980, 1981); Tenorio-Tagle et al. (1987) simulated HVCs passing through the Galactic midplane and found that they punch holes in the disk. More recently, Bekki et al. (2008) presented computer simulations for the case of the Magellanic Stream Leading Arm clouds colliding with the Milky Way disk. They found that 10^7 and 10^8 M $_{\odot}$ clouds caused long lived, kiloparsec scale holes in the outer disk. Our simulations extend those results, finding that clouds with masses 1.7×10^6 to 8.3×10^6 M $_{\odot}$ also punch holes in the Galactic disk. Because we use less massive clouds and a more massive disk than Bekki et al. (2008), we naturally find smaller holes.

Our simulations suggest that the HVC's passage through the disk also creates a bubble surrounded by a higher-density shell. Such shells have been observed in our Galaxy. For example, Park et al. (2016) identified a connection between a compact HVC (HVC 040 + 01-282) and a shell (GS040.2+00.6-70) that appears to surround the cloud in H I maps. Park et al. (2016) suggested that the HVC approached the disk from below at an inclination angle of 30° and passed through the Galactic midplane roughly 5 Myr ago, reaching its currently observed location 420 pc above the Galactic midplane. Based on the energetics of the shell, Park et al. (2016) found that the HVC has lost at least 90% of its mass due to its motion through the disk. Our simulations predict similar consequences. Roughly 5 Myr after passing through the midplane, our simulated cloud is roughly 400 pc from the midplane, appears to be at the edge of the disk, and is surrounded by a shell composed of disk and cloud material. In our simulations, the hole in the disk is apparent; however, if the cloud had approached the disk with a 30° inclination angle and been observed from Earth, the resulting projection of the shell would likely appear to enclose the cloud. In agreement with Park et al. (2016), our simulated clouds lose most of their mass as they pass through the disk.

Regarding the question of the characteristics of the bubble, we find that the interior of the bubble is cool, low metallicity gas mostly originating from the cloud and the disk. The surrounding shell is hotter

than the bubble because it has been shock heated. A small amount of shell material is captured by the minihalo due to the low relative velocity between the expanding shell and the minihalo. Observational signatures of our tepid bubbles include C III, C IV, and C V-rich interiors and shells and heights up to ~ 8 kpc. They survive for at least 40 Myr. It should be noted that these results are idealized. Rotational motion would deform the shapes of the bubbles, making them somewhat harder to identify.

There is some interest in distinguishing bubbles made by high velocity clouds and those made by supernovae. The bubbles formed by supernovae are hot, whereas those formed by HVCs are cool. Supernovae remnants are concentrated in the Galactic disk, whereas HVC-induced bubbles are on one side of the disk or the other (Section 3.3.3; see also Mirabel (1982)). Supernova remnants are usually less than 100 pc across, whereas the holes created by HVCs can exceed 500 pc in diameter and the HVC-induced bubbles can extend 5 kpc or more away from the disk. Supernova explosions increase the metal abundance of the surrounding area, whereas HVC collisions dilute the metal abundances. Supernova explosions typically have energies of 0.5 - 1.0 $\times 10^{51}$ ergs. Assuming a mass of 10^6 M $_{\odot}$ and a collision velocity of 100 km s $^{-1}$, the kinetic energy of such an HVC would be 10^{53} ergs. This is the equivalent of 100-200 supernova explosions. Faster and more massive HVCs would collide with even more energy.

There is observational evidence that HVCs do collide with the Galactic disk. McClure-Griffiths et al. (2008) observed signs of the interaction between the Leading Arm of the Magellanic Stream and the Milky Way's disk. Lockman et al. (2023) found that the forerunner of the Smith Cloud is colliding with the disk. Park et al. (2016) observed a supershell associated with a compact HVC, CHVC040, that collided with the disk of the Milky Way. These examples highlight the importance of understanding the dynamics of HVCs colliding with galactic disks.

3.5 Author Contributions

The simulations in this chapter were run by Jason Galyardt. The analysis was done by myself. The writing was done by Jason Galyardt, Robin Shelton, and myself.

All co-authors agree that the work may be included in this dissertation.

CHAPTER 4

COOLING IN NON-COLLISIONAL EQUILIBRIUM ENVIRONMENTS 1

¹Goetz, E. H. & Shelton, R. L., 2025, To be submitted to the Astrophysical Journal.

Abstract

We implement two new algorithms for radiative cooling in the FLASH hydrodynamic code (Fryxell et al., 2000). Currently, FLASH simulations with radiative cooling use a look-up table with collisional ionization equilibrium cooling rates taken from Sutherland & Dopita (1993). These cooling rates are compiled from data on 16 elements, and the rate used from the table depends on the temperature of the FLASH cell. However, FLASH allows for the tracking of individual ion populations that result from non-equilibrium ionization and recombination. Here, we develop a non-equilibrium cooling algorithm based on the actual ion populations in each cell and corresponding cooling rates for those ions. For comparison purposes, we also develop a new collisional equilibrium cooling algorithm that includes only those elements present in the simulation. Finally, we apply our new radiative cooling algorithms to simulations of high velocity clouds. To determine the effect on the predicted characteristics of these clouds, we compare our results with those from existing simulations (Goetz et al., 2024).

4.1 Introduction

Radiative cooling is an important process in many astrophysical contexts, from high velocity clouds (HVC) to galaxy formation. HVCs are cool clouds moving through a hot ambient environment. As they move, ambient gas is entrained in the cloud and begins to cool. The rate at which that gas cools has implications for the populations of various ions observed in the cloud.

When radiative cooling is included in astrophysics simulations, it is often based on a look-up table using cooling rates calculated in collisional ionization equilibrium (e.g. Kwak & Shelton (2010); Gritton et al. (2014); Goetz et al. (2024) using the FLASH hydrodynamics code (Fryxell et al., 2000), Ramsøy et al. (2021) using the NUT simulation code (Powell et al., 2011)). However, simulations incorporating non-equilibrium ionization and recombination have demonstrated that many astrophysical environments are out of ionization equilibrium. Examples include HVCs (Henley et al., 2012; Kwak et al., 2015; Goetz et al., 2024), turbulent mixing layers (Kwak & Shelton, 2010; Kwak et al., 2015), and the diffuse ionized gas in the Milky Way (McCallum et al., 2024). These environments can have ionization fractions that are significantly different from what would be expected from collisional ionization equilibrium (CIE) calculations. In the case of dynamic environments such as HVCs, the ionization fractions are also different from what would be expected from non-equilibrium ionization (NEI) calculations of hot gas allowed to cool statically (Gnat & Sternberg, 2007). This raises the question of the accuracy of using a CIE table for radiative cooling when modeling these environments. Ions contribute different amounts to the overall cooling rate, so the difference in NEI versus CIE ionization fractions will result in different total cooling rates for the gas. This could substantially change the amount of cooling that occurs in an environment.

Here, we introduce a radiative cooling algorithm for the FLASH simulation code that is based on the actual ion populations present in the simulation, calculated using non-equilibrium collisional ionization and recombination and cooling rates from Chianti (Dere et al., 1997; Del Zanna et al., 2021). We then compare our new algorithm with the existing FLASH radiative cooling method that uses a look-up table with CIE radiative cooling rates from Sutherland & Dopita (1993). However, the radiative cooling rates from Sutherland & Dopita (1993) differ slightly from those in Dere et al. (1997) and Del Zanna et al.

(2021) and include contributions from 16 elements, all of which may not necessarily be present in the FLASH simulations. Therefore, we also introduce a third radiative cooling algorithm based on CIE radiative cooling rates from Chianti, but only including the elements present in the particular FLASH simulation. This provides a more direct comparison between radiative cooling calculations based on collisional ionization ion populations versus non-equilibrium ion populations.

We first compare the three different radiative cooling algorithms by running simulations of a static isothermal gas in a 3-dimensional box. We run simulations at three different initial temperatures - 2×10^4 K, 2×10^5 K, and 2×10^6 K. We also vary the elements present in the simulations. All simulations include hydrogen and helium. They may also include various combinations of C, N, O, and Ne. After H and He, C, N, and O are the most prevalent elements in the Universe. We include Ne as well, because of its significant contributions to cooling in $\sim 10^6$ K CIE gas. We track the gas temperature and the contribution to cooling from the different species present in the simulations. This allows us to determine which of these are the most important elements for radiative cooling in different temperature regimes.

We also apply our new radiative cooling algorithms to simulations of HVCs. We use the same simulation set up as Goetz et al. (2024), but with the different radiative cooling algorithms. We then compare the characteristics of the HVCs predicted from the different simulations, such as the ionization fractions of various oxygen ions, the ratio of H I to O VI, and the cloud temperature.

In Section 4.2, we discuss the development of our new radiative cooling algorithms, as well as the application to HVC simulations. In Section 4.3, we compare the effects of the three cooling algorithms on isothermal gas. We also compare the effects of these cooling algorithms on simulated HVC characteristics. In Section 4.4, we discuss the implications of these results and the importance of using non-equilibrium cooling algorithms.

4.2 Methods

4.2.1 Development of New Algorithms

Cooling in Non-collisional Ionization Equilibrium Plasmas

We use Chianti version 10.1 (Dere et al., 1997; Del Zanna et al., 2021) to calculate the cooling rates from a variety of processes (i.e., radiative recombination, bound-bound transitions, bremsstrahlung, and, for hydrogen-like and helium-like ions, two photon emission) as a function of temperature and ion species, for all possible ionization levels of He, C, N, O, and Ne, plus H II. We sum these cooling rates, resulting in the total cooling coefficient per ion species as a function of temperature, $\Lambda_j(T)$.

We implement these coefficients in FLASH simulations. FLASH and other hydrodynamics codes calculate the temperature and density in each cell in the simulational domain. FLASH also has the ability to calculate the ionization fractions of selected elements² in a time-dependent manner from the ionization and recombination rates and gas temperature. These ionization fractions are needed for our non-equilibrium cooling algorithm.

In order to calculate the total radiative energy loss rate per unit volume in any given cell, we multiply $\Lambda_j(T)$ by the electron number density and the ion number density, and sum over all species. The overall cooling rate per unit volume in a given cell can therefore be given by the following equation:

$$r_{total} = \sum_{i=1}^{N} n_e * n_j * \Lambda_j(T), \tag{4.1}$$

where N is the number of species in the simulation (excluding electrons), n_e is the electron number density, n_j is the number density of the jth species, and Λ_j is the cooling rate of the jth species at the FLASH cell temperature. It should be noted that FLASH assumes that all of the hydrogen in the simulation is ionized. Therefore, we do not include cooling from neutral hydrogen.

²FLASH simulations include hydrogen by default and have an additional 13 elements that can be included as well.

Collisional Ionization Equilibrium Cooling

To see the effects of non-equilibrium radiative cooling, we want to compare with the results of CIE radiative cooling. The existing CIE radiative cooling tables in FLASH do not provide a good comparison because they use cooling rates from Summers (1974) and they include contributions from 16 elements, while FLASH is designed to track the ionization states of up to 14 of these elements. Furthermore, due to computational limitations, most FLASH simulations only track a small subset of those elements. We develop a new CIE radiative cooling algorithm that only considers the elements included in the simulation and uses the same individual ion cooling rates as the NEI cooling algorithm.

The CIE cooling rate per unit volume in a given cell is given by:

$$r_{total} = \sum_{k=1}^{N} n_e * n_k * \left(\sum_{i} f_{i,k}(T) * \Lambda_{i,k}(T)\right),$$
 (4.2)

where N here is the number of elements in the simulation, n_e is again the electron number density, n_k is the total number density of the kth element, $f_{i,k}$ is the ionization fraction of the ith ionization state of the kth element, and $\Lambda_{i,k}$ is the cooling rate of that particular ion.

We test our algorithm using a subset of the elements tracked by FLASH.

Model Comparisons

To compare the three different radiative cooling algorithms (our NEI radiative cooling algorithm, our CIE radiative cooling algorithm, and FLASH's existing CIE radiative cooling algorithm), we run FLASH simulations in an isothermal domain with various subsets of elements included. At the beginning of the simulation, the gas is in CIE, with ionization fractions calculated based on the ionization and recombination rates of Summers (1974). Different elements contribute more to the cooling in different temperature regimes. Therefore, we run simulations at three different initial temperatures: 2×10^4 K, 2×10^5 K, and 2×10^6 K. We run the simulations for 200 Myr. We track the temperature of the domain as a function of time as well as the contribution from each species to the total cooling in each cell. The results of these comparisons are discussed in Section 4.3.1.

4.2.2 High Velocity Cloud Simulations

In order to evaluate the effects of our NEI radiative cooling algorithm with those of FLASH's CIE radiative cooling algorithm, we compare with the results published in Goetz et al. (2024) and therefore use the same physical setup and post-processing as Goetz et al. (2024). Specifically, here we compare with Run 3 in Goetz et al. (2024), which models a cold, dense cloud of gas surrounded by the hot, ambient medium. That run has an ambient temperature and hydrogen number density of $2 \times 10^6 \mathrm{K}$ and $1 \times 10^{-3} \mathrm{cm}^{-3}$, respectively. At the center of the cloud, the initial temperature and hydrogen number density are $5000 \mathrm{K}$ and 0.4 cm⁻³, respectively. However, towards the edge of the cloud, the density decreases to match that of the ambient environment. The density gradation is modeled by the hyperbolic tangent function described in Gritton et al. (2014) with a scale length of 50 pc. The cloud has a radius of 300 pc. As the cloud begins the simulation in pressure equilibrium with the ambient environment, the cloud temperature correspondingly increases towards the edge of the cloud. We use a wind tunnel setup, such that the cloud begins at rest relative to the reference frame of the domain, with the ambient medium moving past it. The ambient environment moves past the cloud at a velocity of 150 km s⁻¹.

As in Goetz et al. (2024), we set the initial metallicity of the cloud to be 10^{-3} times the solar metallicity (Z_{\odot}) and the initial metallicity of the ambient environment to be Z_{\odot} . This is done to easily distinguish between cloud and ambient gas. During post-processing, we scale the metallicities such that the cloud has a metallicity of $0.1Z_{\odot}$ and the ambient medium has a metallicity of $0.7Z_{\odot}$, as in Goetz et al. (2024). These numbers are chosen to match observations; see Goetz et al. (2024) and references therein. To identify cloud material in the simulation domain, we apply a velocity cut. Material with a velocity greater than 100 km s⁻¹ relative to the ambient medium is considered to be part of the HVC. Characteristics of this material, including its average temperature, ionization fractions of various ions, and ion ratios, are discussed in Section 4.3.2.

4.3 Results

4.3.1 Cooling Model Comparisons

Here, we examine the results of the three different radiative cooling algorithms applied to isothermal static gas. Our CIE and NEI cooling algorithms can be run with various numbers of elements. To see the effects of specific elements, we begin with H and He in a cooling simulation. We then add O, then C, then Ne, and finally, N. We examine each of these cases in three temperature regimes. The first has an initial gas temperature of 2×10^5 K and initial gas hydrogen number density of 1×10^{-4} cm⁻³. Our second and third cases have the same density but initial gas temperatures of 2×10^6 K and 2×10^4 K, respectively. Each of the simulations models a single cell. In each simulation, we let the gas radiatively cool for 200 Myr³ using one of the three cooling algorithms and track the temperature and total cooling rate. For our NEI and CIE cooling models, we can also track the contribution to the total cooling rate by each species or element in the simulation, respectively.

H and He Model

The cooling curves for our CIE model and the default FLASH model using H and He are shown in Figure 4.1. The cooling curves for our CIE model have been scaled by the solar metallicity to match Sutherland & Dopita (1993) used in the default FLASH model. The two curves are almost identical at sufficiently high temperatures (above $\sim 10^5$ K). Below that threshold, the curves are significantly different. This is primarily because the default FLASH cooling curve includes the contribution from neutral hydrogen. Our CIE curve does not, because FLASH treats all of the hydrogen as if it is ionized. The individual cooling curves for the four species in our NEI cooling algorithm (H II, He II, He III) are shown in Figure 4.2. Unlike the curves in Figure 4.1, these have not been scaled by metallicity or ionization fraction.

 $^{^{3}}$ In some of the low temperature simulations, the gas temperature reaches the cooling floor of 10^{4} K before 200 Myr. When this happens, the state variables cease to change. FLASH then rapidly increases the time steps, overshooting the intended end time.

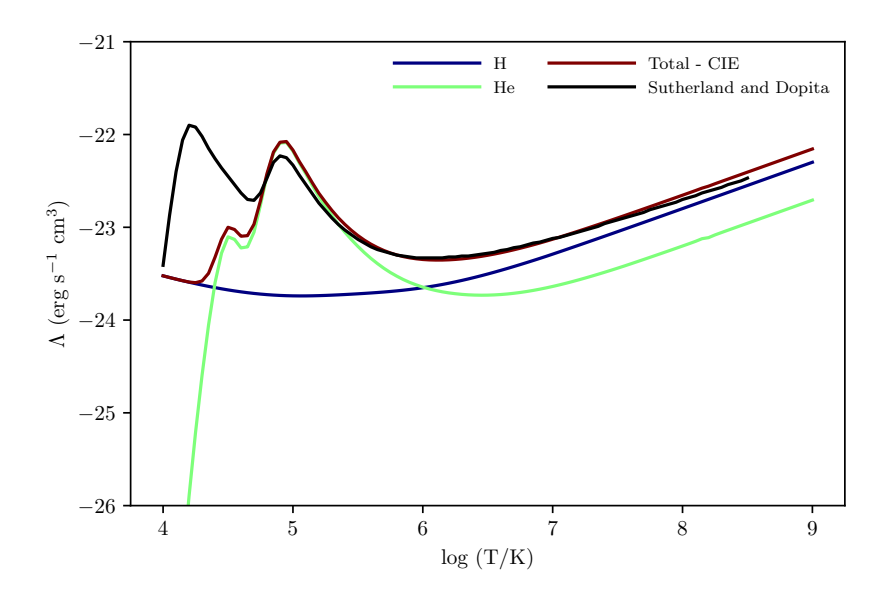


Figure 4.1: Cooling curves for our CIE cooling model and the default FLASH cooling model from Sutherland & Dopita (1993). The black curve is from Sutherland & Dopita (1993) and includes contributions from both H and He. The blue and green curves are the contributions to our CIE cooling curve from H II and all ions of He, respectively. The red line is the combination of the CIE H and He curves.

Figure 4.3 shows the gas temperature as a function of time for the three different cooling models, each with an initial gas temperature of 2×10^5 K. At early times, the three models show similar results. This is because the initial ionization fractions of the helium ions match those expected from a CIE calculation at 2×10^5 K. As the simulation evolves, the three models start to diverge slightly. This is because the He ion fractions calculated from the NEI module in FLASH differ from the fractions predicted by a CIE model.

We can also compare the contribution to the cooling rate from each species or element in the simulation for our NEI and CIE cooling algorithms, respectively. These contributions are shown in Figures 4.4 and 4.5 for our first temperature case. With our CIE algorithm, the cooling is dominated by helium throughout the simulation. This is consistent with helium being responsible for most of the cooling in the $T\sim2\times10^5$ K regime (see Figure 4.1).

In our NEI algorithm, we see that the cooling largely comes from He II. Even though the majority of the He at this temperature is in the He III ionization state, the cooling rate of He II is several orders

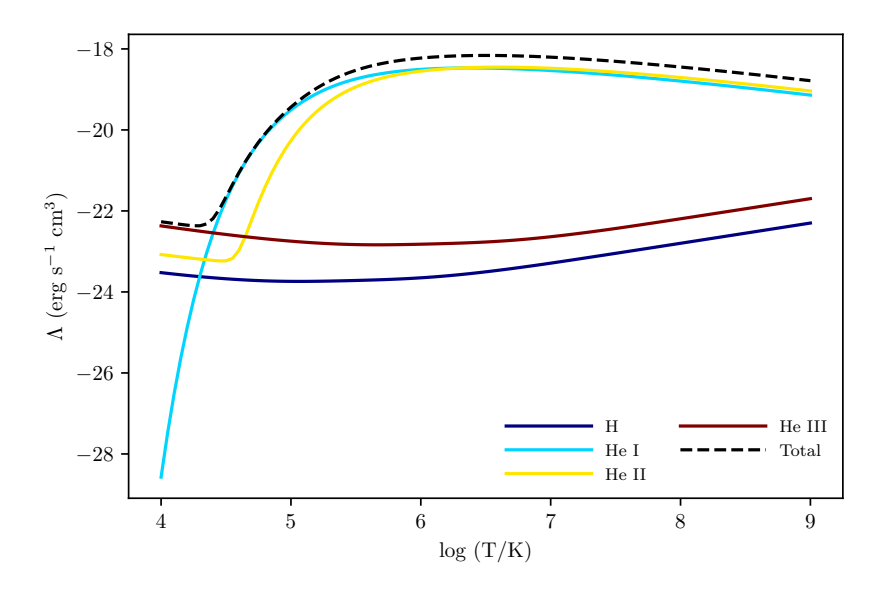


Figure 4.2: Cooling curves for the individual species in our H and He simulations. These are used in our NEI cooling algorithm. Each curve is multiplied by the electron number density and the corresponding ion's number density to get the cooling rate per volume associated with that ion.

of magnitude higher than that of He III at these temperatures. He I has the highest cooling rate of all four species at these temperatures. However, only a negligible fraction of the He is in the He I ionization state, so the cooling resulting from that ion is several orders of magnitude lower than the cooling from the other species.

We next look at simulations with a starting temperature of 2×10^6 K. For this case, there is very little difference between our CIE and NEI cooling rates. This can be attributed to the fact that there is minimal cooling occurring in the simulations. There is little temperature change over the 200 Myr of the simulations, as seen in Figure 4.6. Therefore, there is little change in the ionization fractions for the helium ions. There is slightly more cooling when using the default FLASH cooling algorithm. This is due to the slight differences between our CIE cooling curve and that of Sutherland & Dopita (1993) at 2×10^6 K.

In our CIE model, the cooling is largely done by the hydrogen. Again, this matches what is expected from our CIE cooling curve (Figure 4.1).

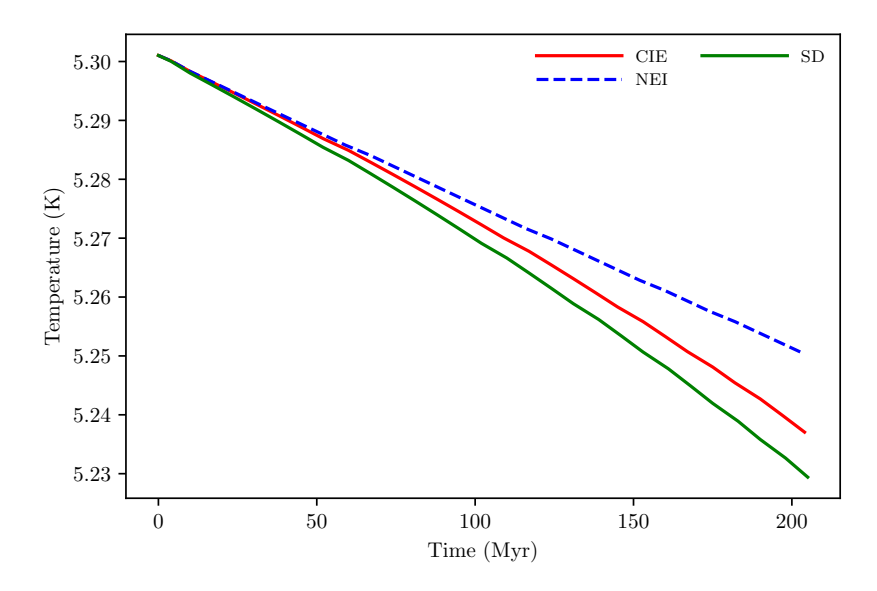


Figure 4.3: Gas temperature as a function of time for the three different cooling models. At early times, the curves overlap. As time evolves and the gas becomes more out of equilibrium, the curves begin to diverge.

In our NEI model, the cooling is dominated by the H II and He III. This is because at these high temperatures, almost all of the helium is He III.

Similarly, for a starting temperature of 2×10^4 K, there is very little difference between our CIE and NEI cases (see Figure 4.9). This is due to the fact that the helium is already mostly in the neutral state. As in the previous case, there is little difference between the helium ionization fractions for the NEI and CIE cases, and therefore little difference in the cooling. An additional factor is that the gas starts close to the cooling floor of 10^4 K, which minimizes the amount of cooling possible in the simulation. For this case, the differences between the our CIE and NEI models and the FLASH model are more pronounced. This is because even though FLASH treats all hydrogen as ionized, the cooling curve from Sutherland & Dopita (1993) includes the contribution from neutral hydrogen, which has a large cooling rate at low temperatures (see Figure 4.1). This is most important at low temperatures.

In our CIE model at this temperature, the contributions to cooling due to hydrogen and helium are similar.

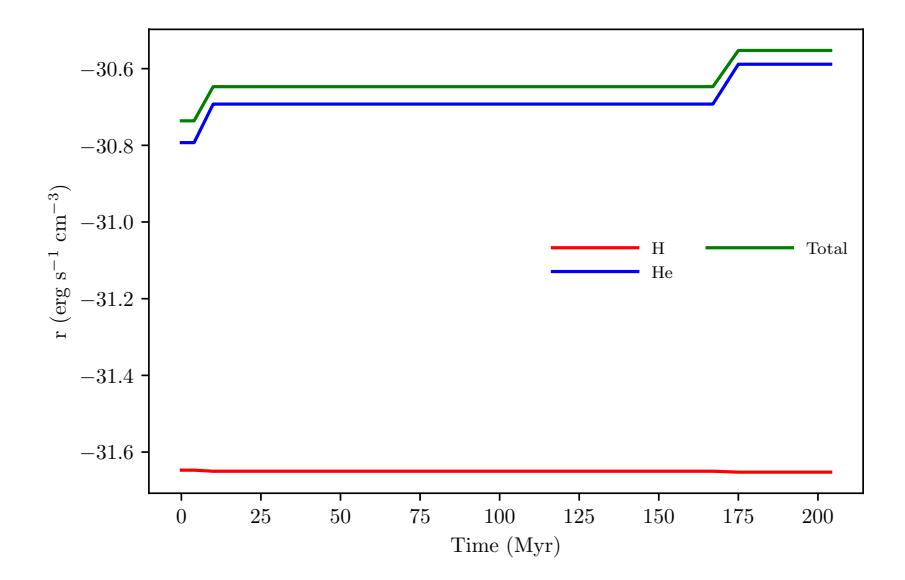


Figure 4.4: Cooling rates per volume for hydrogen and helium in our CIE radiative cooling model for the simulation with an initial temperature of 2×10^5 K. At each epoch, we use the temperature of the gas to select the correct cooling coefficients from the cooling curves shown in Figure 4.1. We then multiply by the electron number density, hydrogen number density, and the element's solar abundance to get the cooling rate per volume shown here.

In our NEI model, the cooling is dominated by hydrogen and He I. At this temperature regime, the helium is almost entirely in the He I state, so this result makes sense.

The difference between our NEI and CIE cooling models is largest at the intermediate temperature regime (2 \times 10⁵ K). The fast cooling in that temperature regime allows ions to get out of equilibrium, so CIE is poor at modeling the actual ionization fractions.

H, He, and O Model

Next, we add oxygen to our NEI and CIE models. For the default FLASH model, we also switch to the cooling curves from Sutherland & Dopita (1993) that include a total of 16 elements. The Sutherland & Dopita (1993) cooling curve and our CIE cooling curves for this model are shown in Figure 4.12. The cooling is dominated by oxygen over a wide temperature range in this model, from $T = 10^4 \, \text{K} - 10^7 \, \text{K}$. The individual cooling curves for the species in this NEI cooling model are shown in Figure 4.13. As in the previous section, these curves have not been scaled by metallicity. The dominant species for cooling in

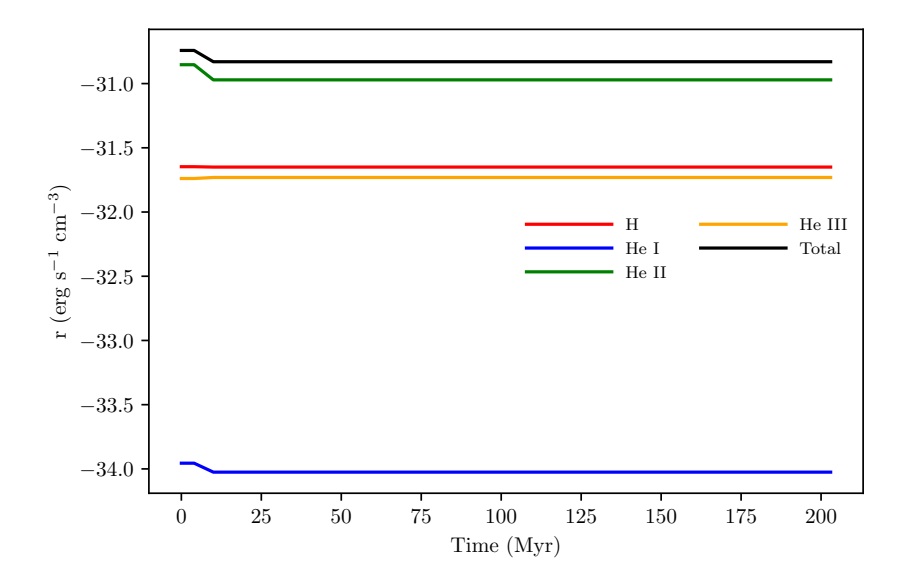


Figure 4.5: Cooling rates per volume for hydrogen and all ions of helium, calculated from our NEI radiative cooling model for the simulation with an initial temperature of 2×10^5 K. At each epoch, we use the temperature of the gas to select the correct cooling coefficients from the cooling curves shown in Figure 4.2. We then multiply by the electron number density and the ion's number density to get the cooling rate per volume shown here.

the temperature regimes we are interested in are largely the middle O ions, such as O III, O IV, O V, and O VI. At very low and high temperatures, the contributions from high ions such as O VIII and O IX are important.

As in the previous section, we start testing our cooling models in simulations with an initial gas temperature of 2×10^5 K. The gas temperature as a function of time for the three models is shown in Figure 4.14.

In our CIE model, the cooling is done almost entirely by oxygen. This is expected from the CIE cooling curve, shown in Figure 4.12.

In our NEI model, the cooling is dominated by the middle oxygen ions, such as O IV and O V.

We next examine the cases with a starting temperature of 2×10^6 K. As in the previous section, our CIE and NEI models produce almost identical results (see Figure 4.17). Again, this is because there is very little cooling occurring in these simulations, as shown in the CIE and NEI cooling curves at this temperature (see Figures 4.12 and 4.13). There is more cooling in the simulation that uses the cooling

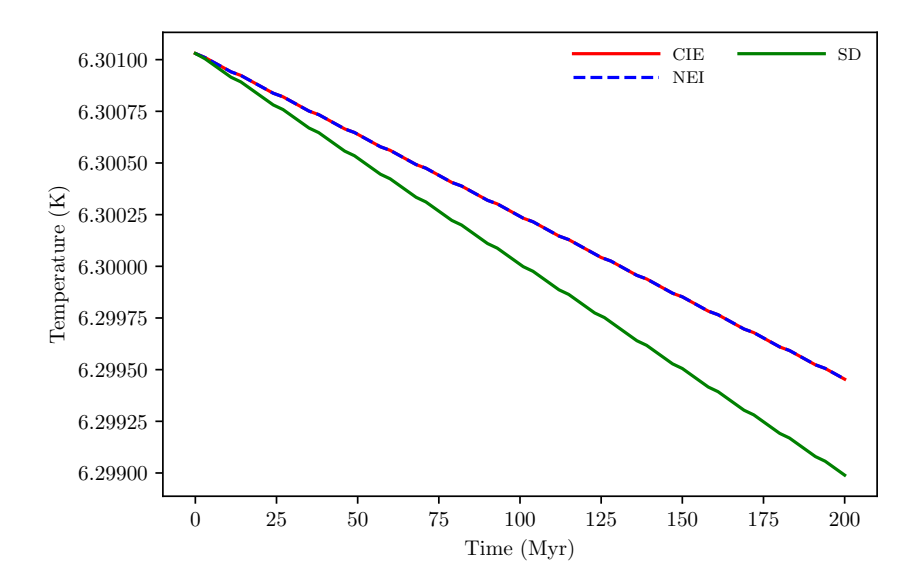


Figure 4.6: Same as Figure 4.3, but for the simulation with an initial gas temperature of 2×10^6 K.

curve from Sutherland & Dopita (1993). This is because far more elements are included in that cooling curve, compared to our CIE and NEI models.

In our CIE model, the cooling is mostly done by oxygen. However, both hydrogen and helium contribute non-negligible cooling to the simulation, with their cooling rates per unit volume being approximately one order of magnitude smaller than that of oxygen, as shown in Figure 4.18.

In our NEI model, we see that the cooling is largely done by high oxygen ions, such as O VII and O VIII (see Figure 4.19). This matches expectations, as these are two of the most prevalent oxygen ions in this temperature regime.

Finally, we examine the simulations with an initial gas temperature of 2×10^4 K. There is much more cooling in these simulations due to the inclusion of oxygen. The simulations with our CIE and NEI models reach the cooling floor of 10^4 K before the simulations end. They also match each other extremely well. The default FLASH cooling model has a different cooling floor, but the gas temperature in the simulation using that model appears to start to asymptote to $\sim 10^{3.7}$ K. These results are shown in Figure 4.20.

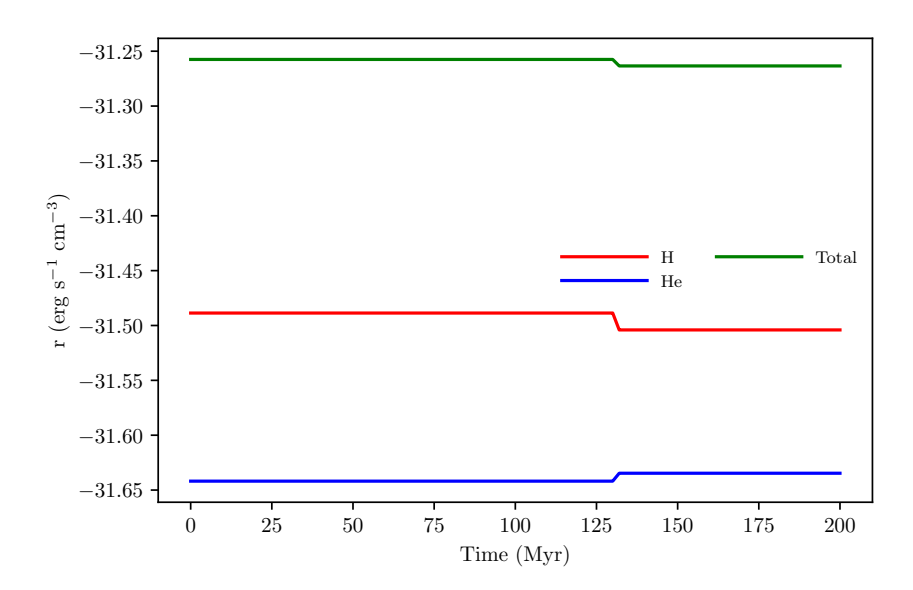


Figure 4.7: Same as Figure 4.4, but for the simulation with an initial gas temperature of 2×10^6 K.

At the start of the simulation using our CIE model, the cooling is primarily done by oxygen. As the gas cools, the contribution from hydrogen begins to become the dominant factor. Helium does not contribute an appreciable amount to the overall cooling in this simulation. See Figure 4.21.

In our NEI model, the cooling is dominated by hydrogen and low ions of oxygen (mostly O II). No oxygen ions higher than O III contribute to the cooling (see Figure 4.22).

As in the previous section, the largest differences between our CIE and NEI models occur in the 2×10^5 K initial temperature simulations. The cooling is maximized in this temperature regime, allowing for ions to get out of equilibrium more easily than in the other temperature regimes. Additionally, in the high temperature regime, the helium and oxygen atoms are already entirely or significantly ionized. The minimal cooling in this regime limits the opportunity for oxygen ions to recombine, resulting in little difference between the ionization fractions in the CIE and NEI models. Similarly, in the low temperature regime, the helium and oxygen in the gas starts in a largely neutral or singly ionized state. Despite the significant cooling that occurs, the ionization fractions for helium and oxygen ions do not change much, since they are already in their lowest ionization states.

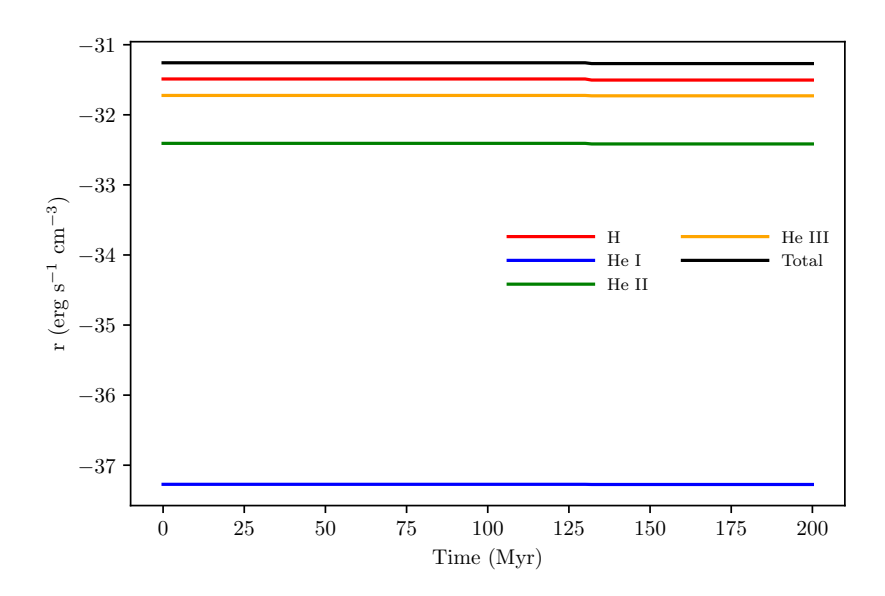


Figure 4.8: Same as Figure 4.5, but for the simulation with an initial gas temperature of 2×10^6 K.

H, He, C, and O Model

We next add carbon to our NEI and CIE models. We use the same cooling curve from Sutherland & Dopita (1993) as in the previous section, as it includes C among its elements. The Sutherland & Dopita (1993) cooling curve and our CIE cooling curves for this model are shown in Figure 4.23. The cooling is largely dominated by oxygen from $T = \sim 10^4 \text{ K} - \sim 10^7 \text{ K}$. However, between 10^4 K and 10^5 K , the cooling from carbon matches and even exceeds the cooling from oxygen.

The individual cooling curves for the species in this NEI cooling model are shown in Figure 4.24. As in the previous sections, these curves have not been scaled by metallicity. Oxygen is the dominant coolant in this model. However, low and middle carbon ions (C II to C V) have significant cooling rates in the temperature range of 10^4 K to 10^6 K.

We first examine our cooling models in simulations with an initial gas temperature of 2×10^5 K. The temperature of the gas in the simulation over time is shown in Figure 4.25 for the three cooling models. There are significant differences between the three models. The default FLASH method has the most cooling. This is expected because it uses the Sutherland & Dopita (1993) cooling curve, which includes

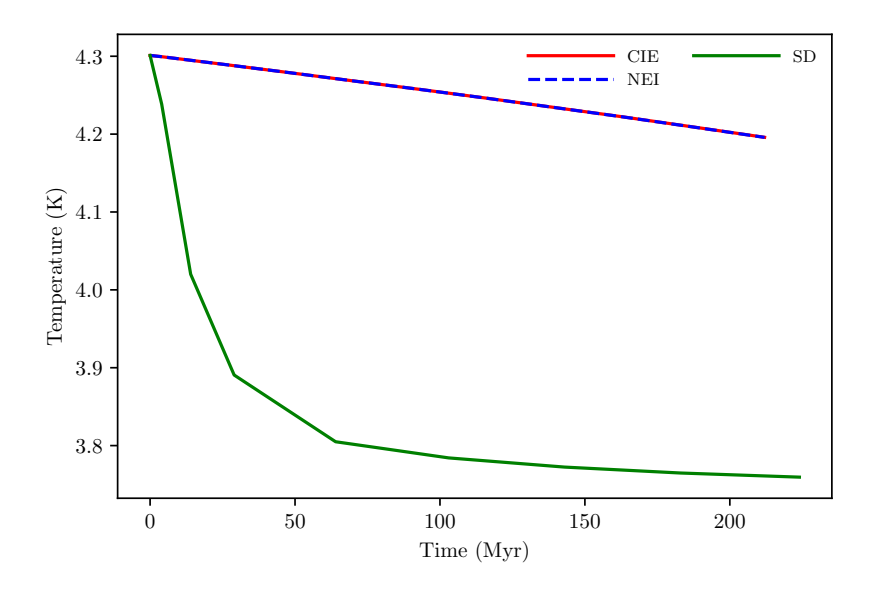


Figure 4.9: Same as Figure 4.3, but with an initial gas temperature of 2×10^4 K.

contributions from 16 elements, rather than the four that are included in our CIE and NEI models. We also see that there is much more cooling from our CIE model, compared to our NEI model.

In our CIE model, the cooling is mostly done by carbon and oxygen, as seen in Figure 4.26. This is expected from the CIE cooling curve, shown in Figure 4.23. At late times (and therefore lower temperatures), the contribution from hydrogen starts to become a more significant factor.

In our NEI model, the cooling is dominated by oxygen. Of the carbon ions, C IV is the most important contributor, on par with hydrogen and helium. C IV is a middle ion prevalent in this temperature range, so it is not surprising that it is an important contributor to the cooling in the simulation. The other carbon ions do not contribute significant amounts to the overall cooling rate per volume, with the possible exception of C III and C V at some brief points in the simulation. This is shown in Figure 4.27.

Next, we examine the simulations with a starting gas temperature of 2×10^6 K. Our CIE and NEI models do produce similar results, but there are more noticeable differences at late times. However, cooling is still minimal in these simulations. Again, there is more cooling in the simulation that uses the cooling curve from Sutherland & Dopita (1993), because of its increased number of included elements.

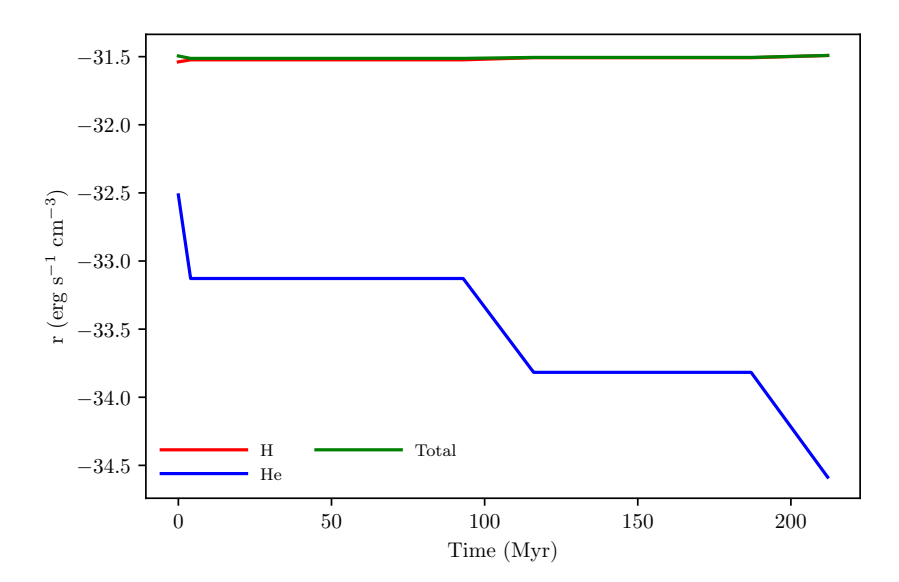


Figure 4.10: Same as Figure 4.4, but for the simulation with an initial gas temperature of 2×10^4 K.

At this starting temperature, the cooling in our CIE model is dominated by oxygen. The cooling from hydrogen, helium, and carbon is non-negligible, again at approximately one order of magnitude smaller than that from oxygen (Figure 4.29).

In the simulation using our NEI model, oxygen is most responsible for the cooling. C VI is a significant contributor, on par with hydrogen and helium. C V and C VII make minor impacts on the overall cooling rate, while the rest of the carbon ions are not significant (Figure 4.30).

We then look at the simulations with an initial gas temperature of 2×10^4 K. As in the previous section, both our CIE and NEI models reach the cooling floor of 10^4 K before the end of the simulation, and they produce similar results. As we use the same Sutherland & Dopita (1993) cooling curve for the simulation using the default FLASH cooling algorithm, the green curve in Figure 4.31 matches the green curve in Figure 4.20.

At the start of the simulation using our CIE cooling algorithm, the cooling is dominated by oxygen. As the simulation evolves and the gas cools, the contributions from hydrogen and carbon grow in importance. At approximately 75 Myr, carbon becomes the largest contributor to the overall cooling rate, and even hydrogen surpasses oxygen (see Figure 4.32).

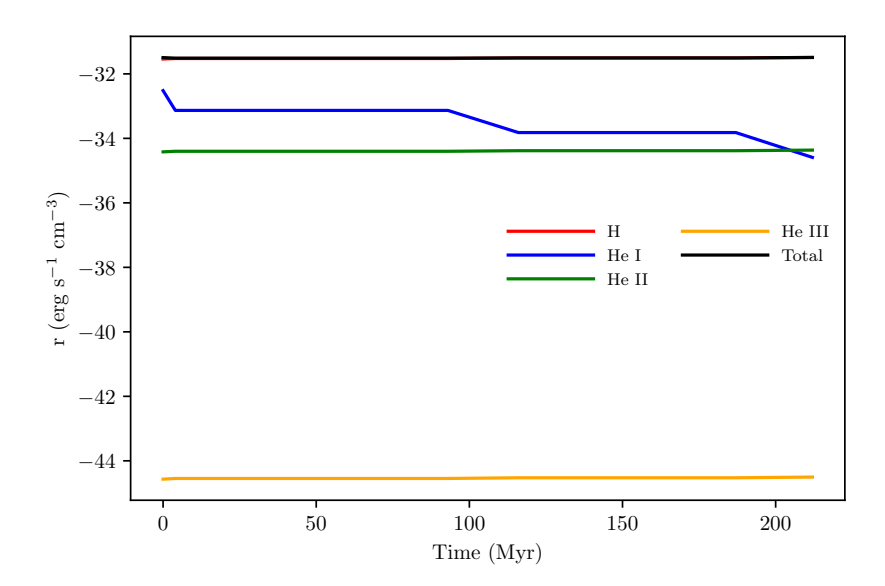


Figure 4.11: Same as Figure 4.5, but for a simulation with an initial gas temperature of 2×10^4 K.

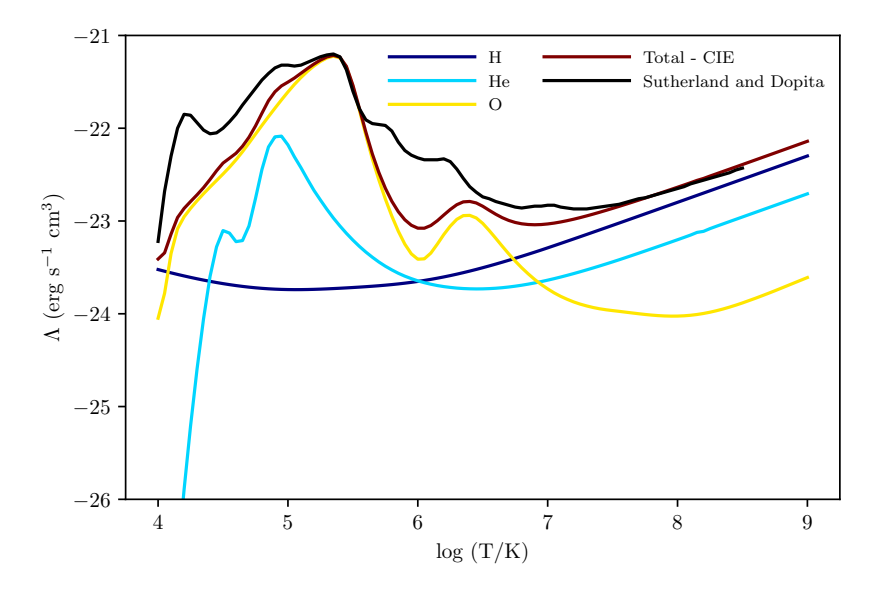


Figure 4.12: Cooling curves for our CIE cooling model and the default FLASH cooling model from Sutherland & Dopita (1993). The black curve is from Sutherland & Dopita (1993) and includes contributions from H, He, and 14 other elements. The dark and light blue curves are the contributions to our CIE cooling curve from H II and all ions of He, respectively. The yellow line is the contribution to the CIE cooling curve from all ions of O. The maroon line is the combination of the CIE H, He, and O curves.

In our NEI model at this starting temperature, the cooling is mostly due to oxygen. Of the carbon ions, the most important to the overall cooling rate is C II. Only C I and C III contribute even slightly to the overall cooling rate of this simulation (see Figure 4.33).

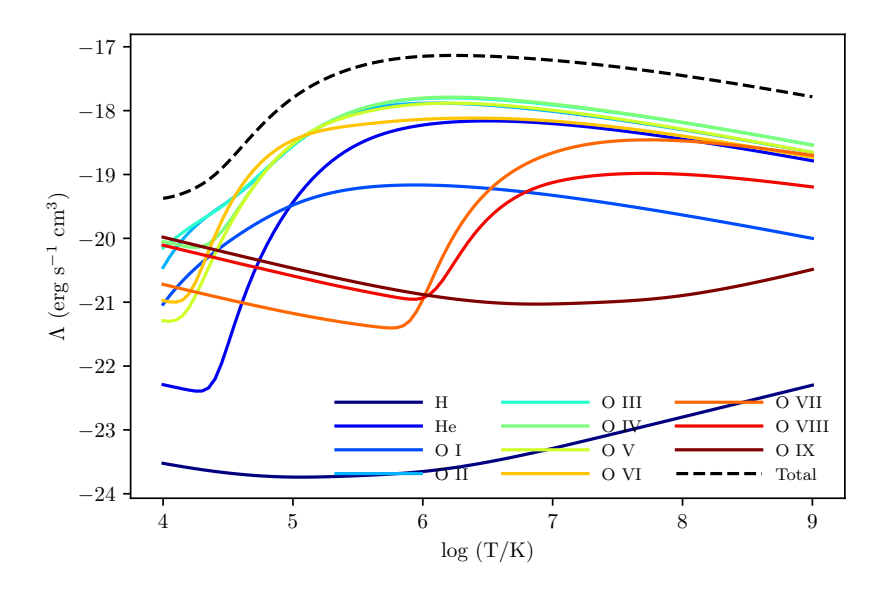


Figure 4.13: Cooling curves for some the individual species in our H, He, and O simulations. We combine the cooling curves for the three helium ions into one curve (shown in blue). The individual cooling curves for each of the oxygen ions are included. These curves are used in our NEI cooling algorithm.

Again, we find that the differences between our CIE and NEI models are most significant in the simulations with an initial gas temperature of 2×10^5 K. This is for similar reasons as discussed in the previous section; larger cooling rates combined with a wide range of ions present in the simulations allow for more out of equilibrium ionization fractions.

H, He, C, O, and Ne Model

Next, we add neon to our NEI and CIE models. As in the previous two sections, we use the same cooling curve from Sutherland & Dopita (1993). The Sutherland & Dopita (1993) cooling curve and our CIE cooling curves for this model are shown in Figure 4.34. Neon does not play a significant role in the cooling, except for its peak at $\sim 10^{5.2}$ K.

Figure 4.35 shows the individual ion cooling curves for all ions of neon. These curves are not scaled by metallicity or ionization fraction. Many of the neon ions have similar magnitude cooling curves, but all of them are smaller than those of carbon and oxygen.

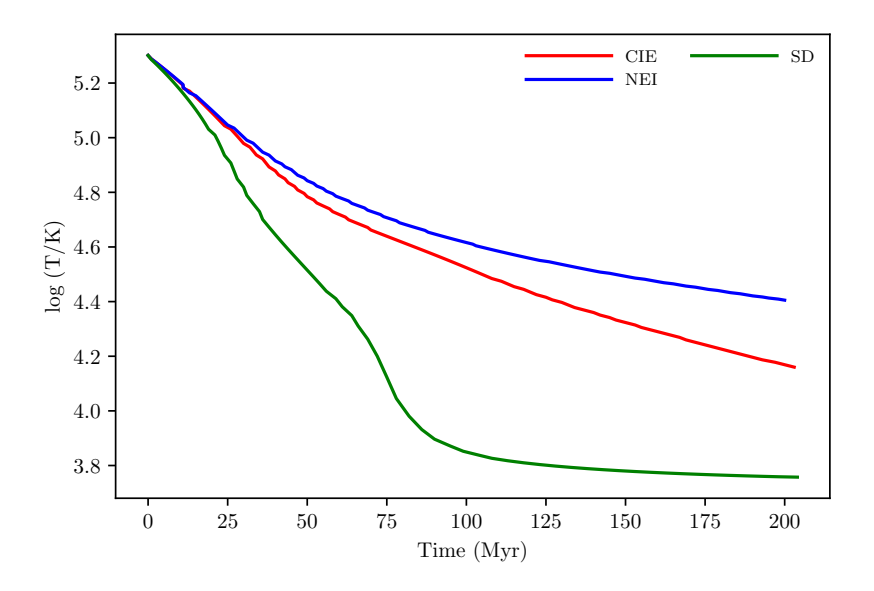


Figure 4.14: Same as Figure 4.3, but our CIE and NEI models shown here include H, He, and O. The Sutherland & Dopita (1993) model used here includes contributions from 16 elements.

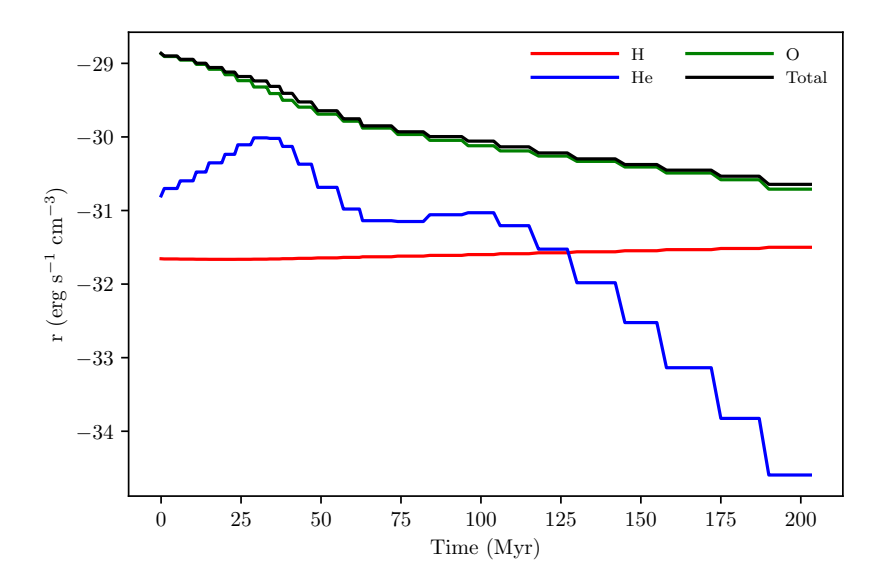


Figure 4.15: Same as Figure 4.4, but for a simulation with H, He, and O.

First, we apply our cooling model to simulations with an initial temperature of 2×10^5 K. Figure 4.36 shows the gas temperature of the gas in the simulation over time for the three cooling models. There are significant differences between the three models. The default FLASH method has the most cooling. This is expected because it uses the Sutherland & Dopita (1993) cooling curve, which includes contributions

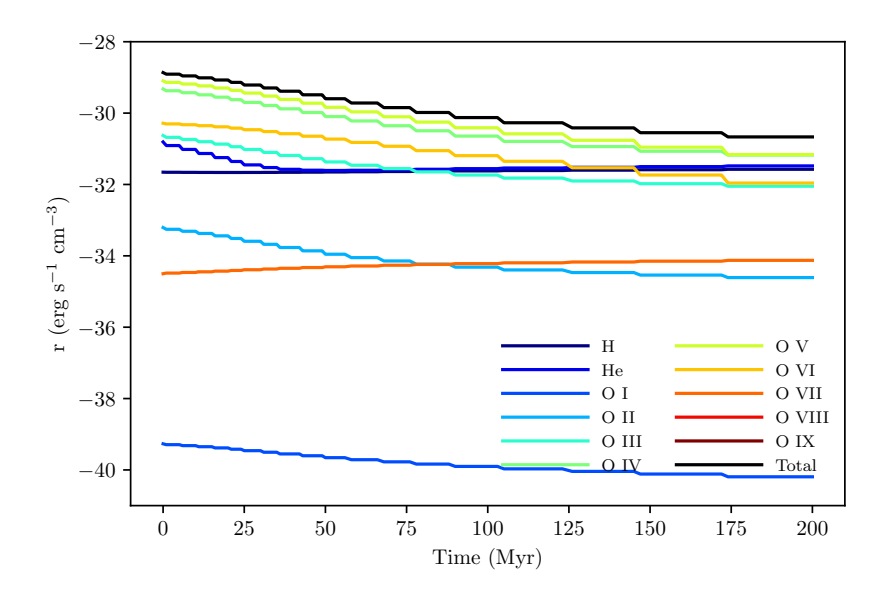


Figure 4.16: Same as Figure 4.5, but for a simulation with H, He, and O. The curves for O VIII and O IX are not shown here because they are too low.

from 16 elements, rather than the five that are included in our CIE and NEI models. We also see that there is much more cooling from our CIE model, compared to our NEI model.

As in the previous section, the cooling here is largely done by carbon and oxygen (see Figure 4.37). The cooling from neon is similar to that from helium. Especially for late times in the simulation, the cooling from neon and helium are several orders of magnitude smaller than that from hydrogen, carbon, or oxygen.

As in the previous section, the cooling in the simulation using our NEI model is dominated by oxygen (Figure 4.38). Ne V is the largest contributor to the cooling of the neon ions, on par with the contributions from hydrogen, helium, and carbon.

We now look at the simulations with an initial temperature of 2×10^6 K. In this case, our CIE and NEI models produce almost identical results for the gas temperature in their respective simulations (Figure 4.39). In both cases, the cooling is minimal. There is more cooling in the simulation using the default FLASH algorithm, as in the previous sections.

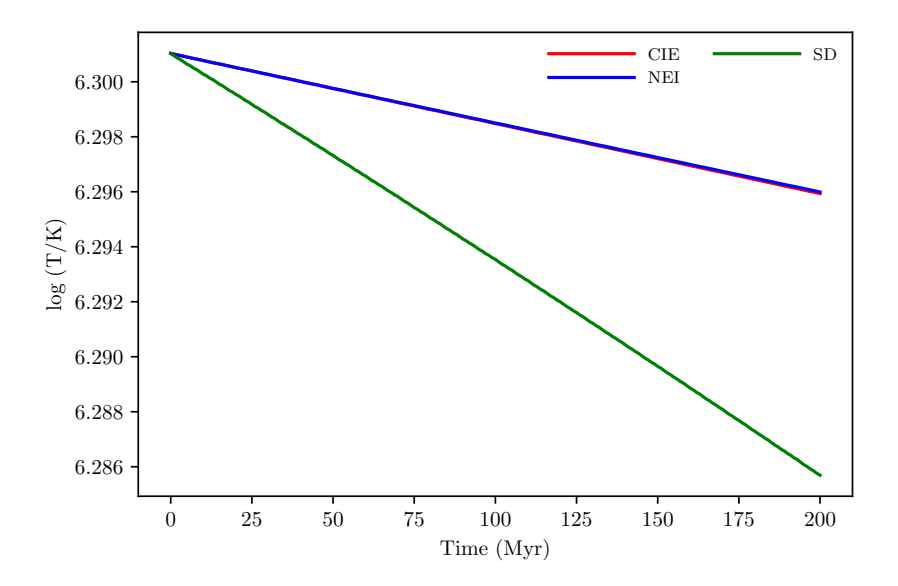


Figure 4.17: Same as Figure 4.14, but for a simulation with an initial temperature of 2×10^6 K.

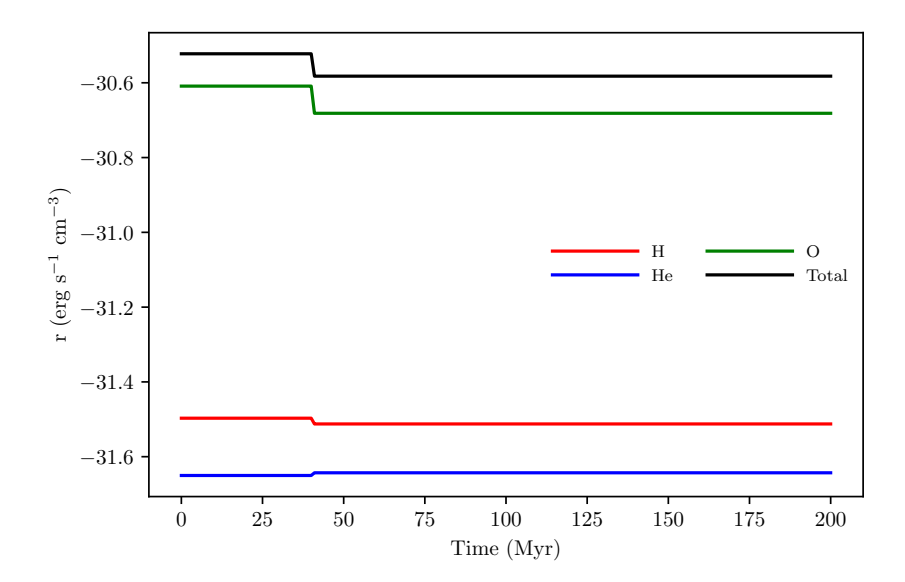


Figure 4.18: Same as Figure 4.15, but for a simulation with an initial temperature of 2×10^6 K.

For the simulation using our CIE model, the cooling comes mostly from oxygen. The cooling from neon is similar to that from hydrogen, helium, and carbon (Figure 4.40).

Using our NEI model, the cooling is predominantly due to oxygen. Of the neon ions, the cooling from Ne VIII and Ne IX is the most significant. Ne VII and Ne X also account for minor contributions to the overall cooling rate. See Figure 4.41.

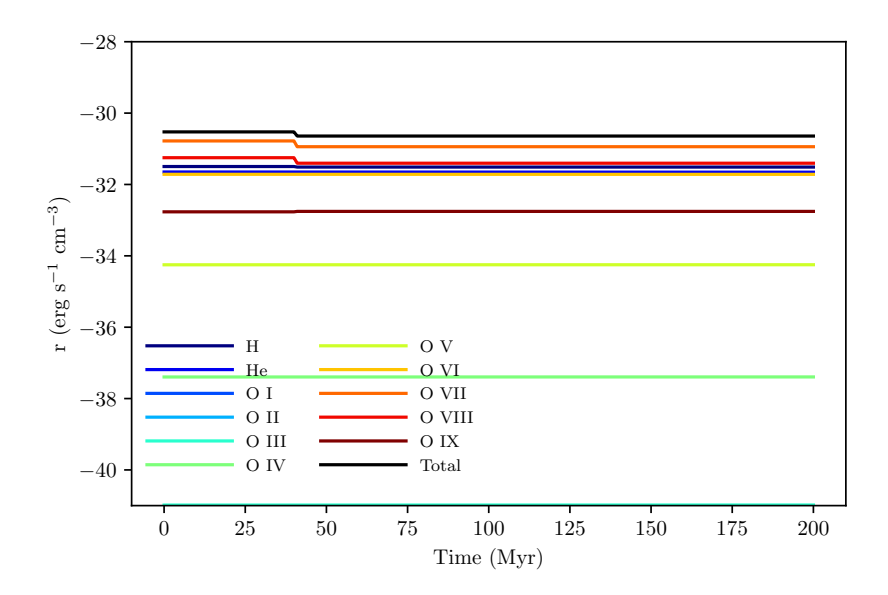


Figure 4.19: Same as Figure 4.16, but for a simulation with an initial temperature of 2×10^6 K.

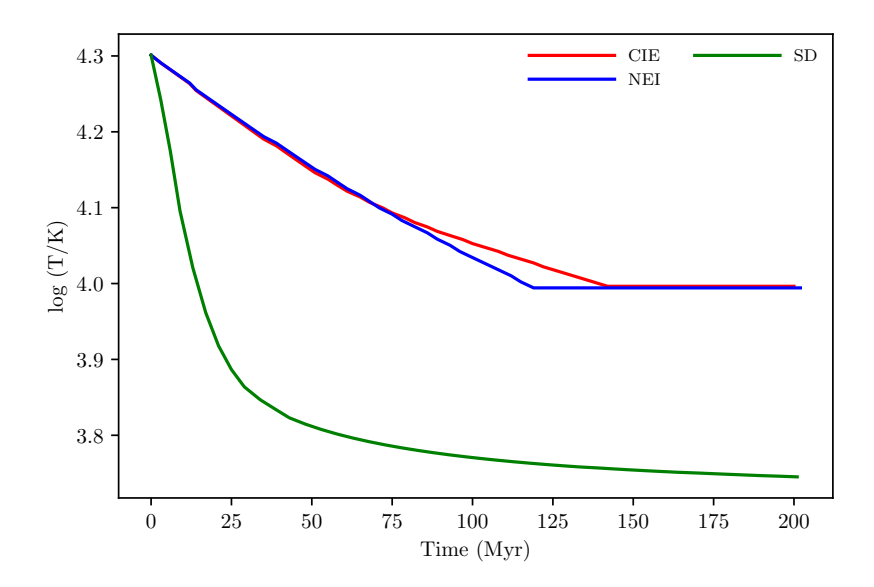


Figure 4.20: Same as Figure 4.14, but for a simulation with an initial temperature of 2×10^4 K.

Finally, we consider simulations with an initial gas temperature of 2×10^4 K. The temperatures of the simulations with our CIE and NEI models overlap well and reach the cooling floor, as seen in Figure 4.42.

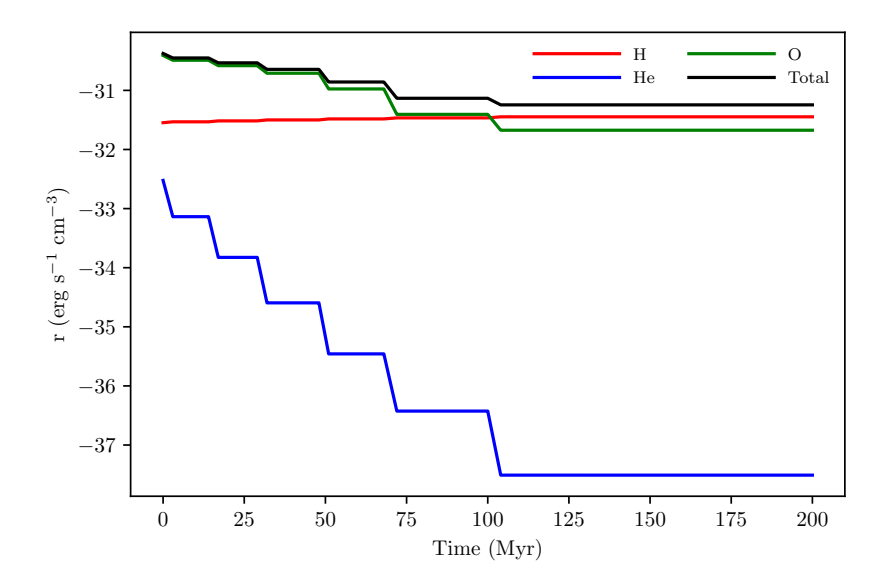


Figure 4.21: Same as Figure 4.15, but for a simulation with an initial temperature of 2×10^4 K.

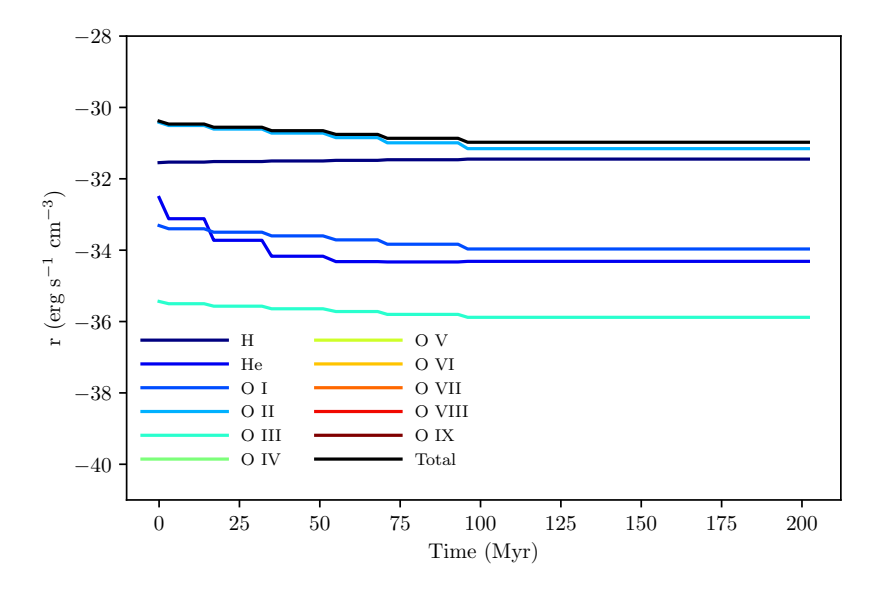


Figure 4.22: Same as Figure 4.16, but for a simulation with an initial temperature of 2×10^4 K. The curves for oxygen ions above O III are not shown here because they are too small to fit on the plot.

In the simulation using our CIE cooling algorithm, the largest contributor to the cooling rate is oxygen, with carbon and hydrogen also playing significant roles. Helium and neon do not contribute much to the overall cooling rate (Figure 4.43).

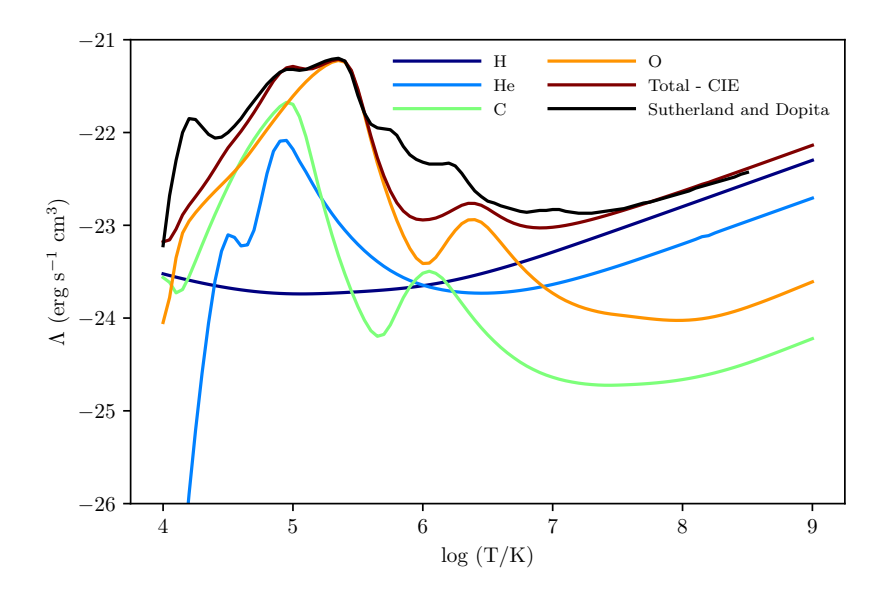


Figure 4.23: Cooling curves for our CIE cooling model and the default FLASH cooling model from Sutherland & Dopita (1993). The black curve is from Sutherland & Dopita (1993) and includes contributions from H, He, and 14 other elements. The dark and light blue curves are the contributions to our CIE cooling curve from H II and all ions of He, respectively. The green and orange lines are the contribution to the CIE cooling curve from all ions of C and O, respectively. The maroon line is the combination of the CIE H, He, C, and O curves.

In the simulation using our NEI cooling algorithm, the cooling is mostly due to oxygen, carbon, and hydrogen. Of the neon ions in the simulation, only Ne II is responsible for any significant contribution to the cooling rate (Figure 4.44).

As in the previous two sections, we find the largest differences between the simulations using our CIE and NEI models for an initial gas temperature of 2×10^5 K. This is due to the fact that the peak of the cooling curve is in this temperature regime. We also find that neon is not a significant source of radiative cooling for these cases.

H, He, C, N, O, and Ne Model

Finally, we add nitrogen to our NEI and CIE models. As in the previous three sections, we use the same cooling curve from Sutherland & Dopita (1993). The Sutherland & Dopita (1993) cooling curve and our CIE cooling curves for this model are shown in Figure 4.45.

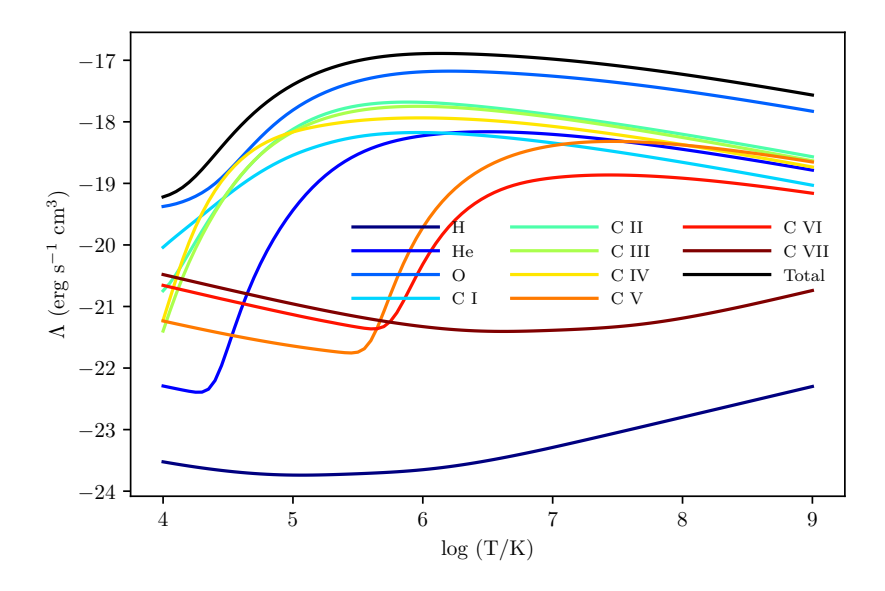


Figure 4.24: Cooling curves for the individual species in our H, He, C, and O simulations. To highlight the effect of the carbon ions, we combine the individual cooling curves for the three helium ions and the nine oxygen ions. These curves are shown in different shades of blue. These curves are used in our NEI cooling algorithm.

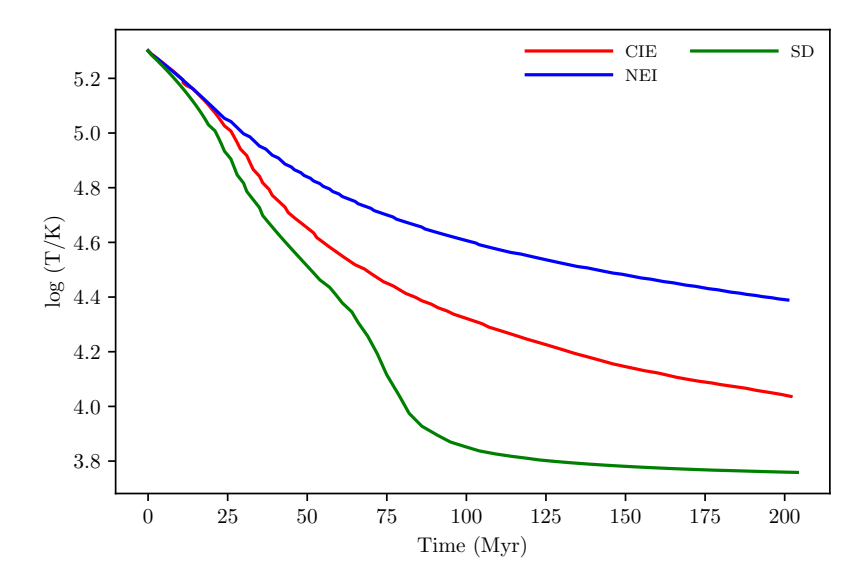


Figure 4.25: Same as Figure 4.3, but our CIE and NEI models shown here include H, He, C and O. The Sutherland & Dopita (1993) model is the same as in Figure 4.14.

Figure 4.46 shows the individual ion cooling curves for all ions of nitrogen. These curves are not scaled by metallicity. The low and middle ions of nitrogen (i.e., N II to N V)) contribute the most to the overall cooling of all the nitrogen ions.

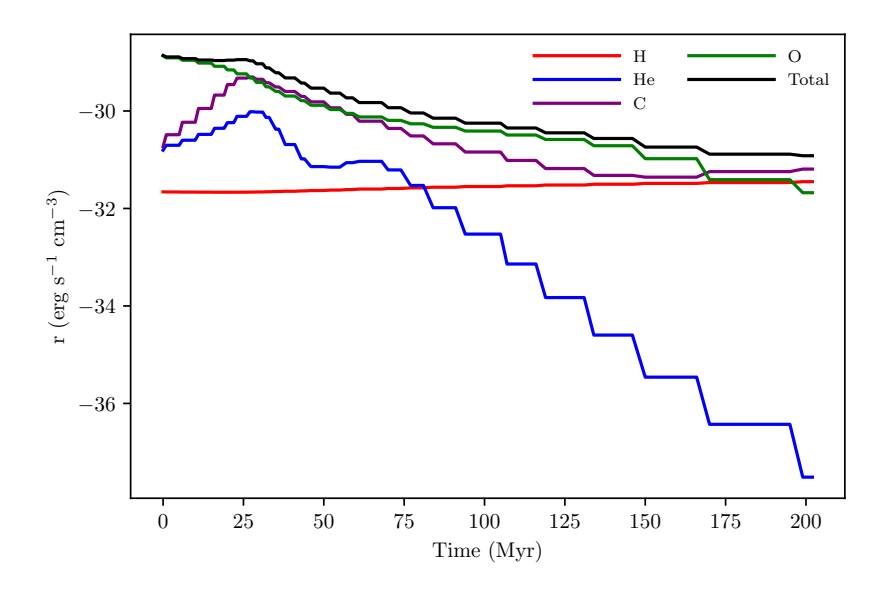


Figure 4.26: Same as Figure 4.4, but for a simulation with H, He, C, and O.

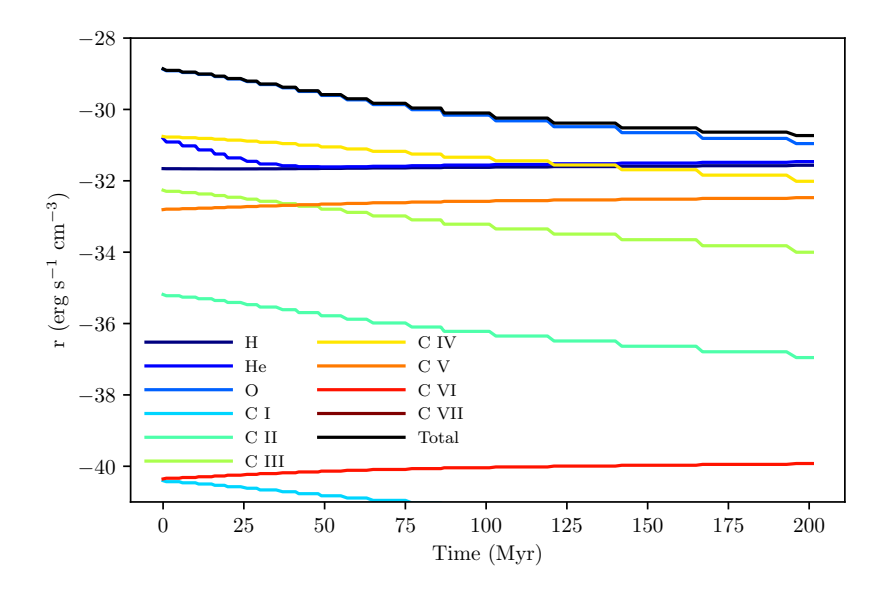


Figure 4.27: Same as Figure 4.5, but for a simulation with H, He, C, and O. The curve for C VII is not shown here because it is too low.

We first apply our cooling models to simulations with an initial temperature of 2×10^5 K. The gas temperature of the gas in the simulation over time for the three cooling models is shown in Figure 4.47. At early times, the cooling is stronger in our NEI case than in our CIE case. At approximately 50 Myr, this trend reverses. Again, the default FLASH method has the most cooling.

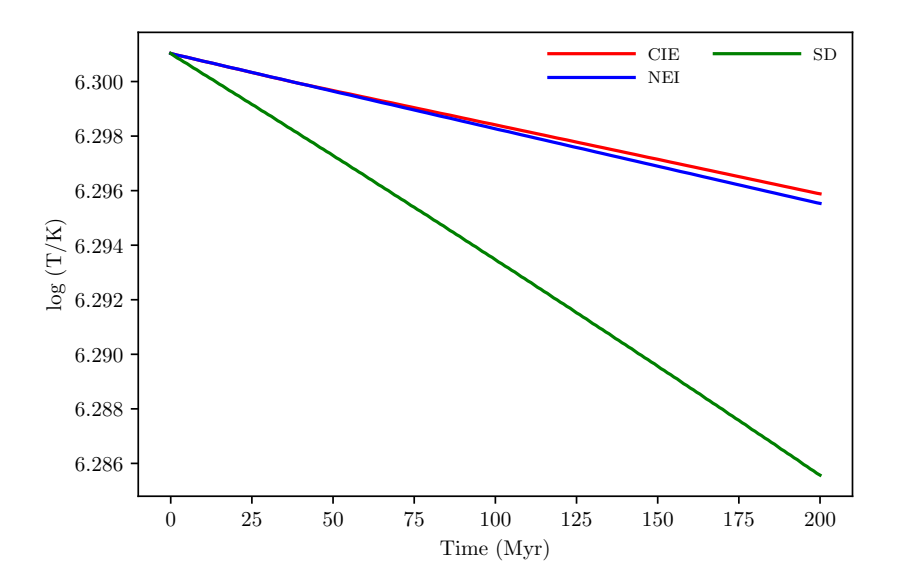


Figure 4.28: Same as Figure 4.25, but for a simulation with an initial temperature of 2×10^6 K.

In our CIE model, at early times, the nitrogen contributes a significant amount to the overall cooling rate (Figure 4.48). As time evolves, the contribution from nitrogen drops off and it is surpassed by carbon and hydrogen.

In our NEI model, N IV and N V contribute the most to the cooling. N III and N VI contribute some at early and late times, respectively (Figure 4.49).

We next run simulations with an initial gas temperature of 2×10^6 K. The gas temperature as a function of time is shown in Figure 4.50. As in the other simulations with this initial gas temperature, the difference between our NEI and CIE models is negligible.

Using our CIE model, we find that oxygen is responsible for the most cooling (Figure 4.51). Carbon and hydrogen are the next largest contributors, with cooling rates per volume within one order of magnitude to that of oxygen. Nitrogen contributes a similar amount of cooling as hydrogen.

Using our NEI model, of the nitrogen ions, N VI and N VII contribute the most to the cooling. These are followed by N VIII and N V (Figure 4.49).

Finally, we run our simulations with a starting temperature of 2×10^4 K. The cooling for our CIE and NEI models is similar, with both simulations quickly reaching the cooling floor (Figure 4.53). The default

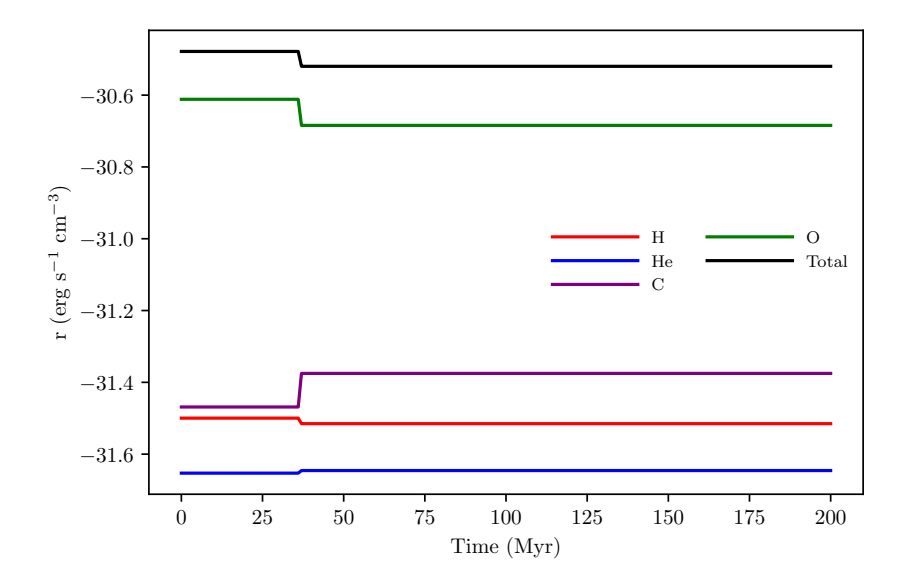


Figure 4.29: Same as Figure 4.26, but for a simulation with an initial temperature of 2×10^6 K.

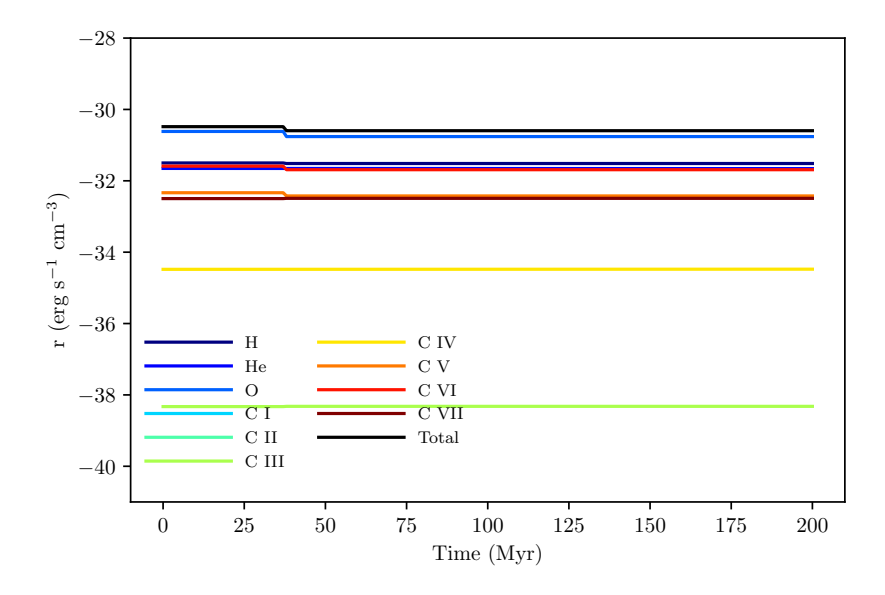


Figure 4.30: Same as Figure 4.27, but for a simulation with an initial temperature of 2×10^6 K. The cooling rates for C I and C II are not shown here because their values are too small.

FLASH cooling model produces more cooling, due to the different cooling floor and larger number of contributors.

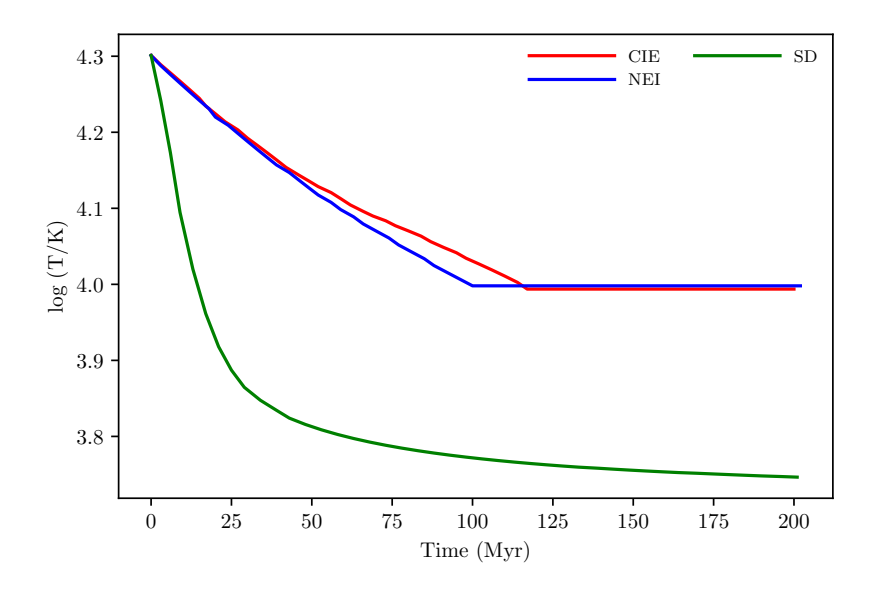


Figure 4.31: Same as Figure 4.25, but for a simulation with an initial temperature of 2×10^4 K.

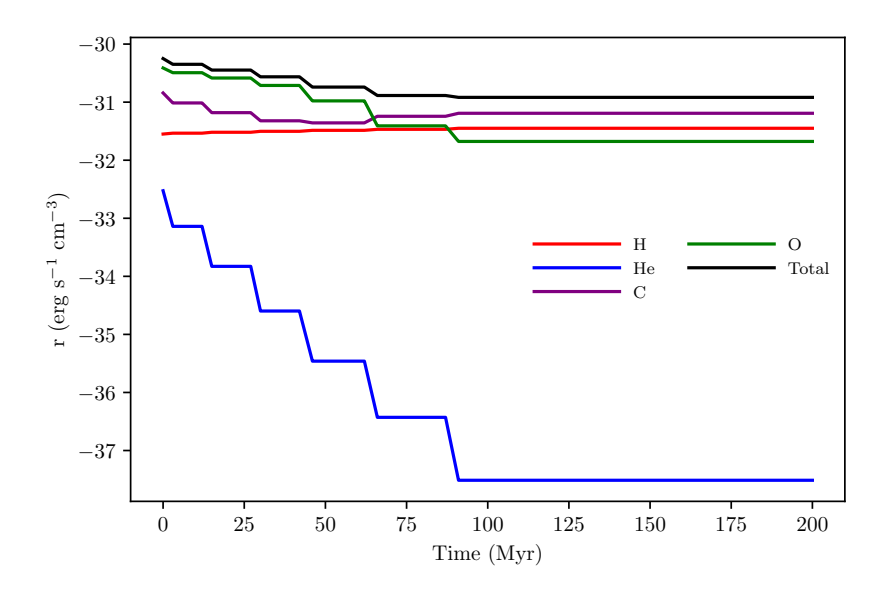


Figure 4.32: Same as Figure 4.26, but for a simulation with an initial temperature of 2×10^4 K.

The simulation with our CIE model has most of the cooling resulting from oxygen. Carbon and hydrogen are the next largest contributors, but nitrogen, neon, and helium all have cooling rates within approximately one order of magnitude of that of oxygen (see Figure 4.54).

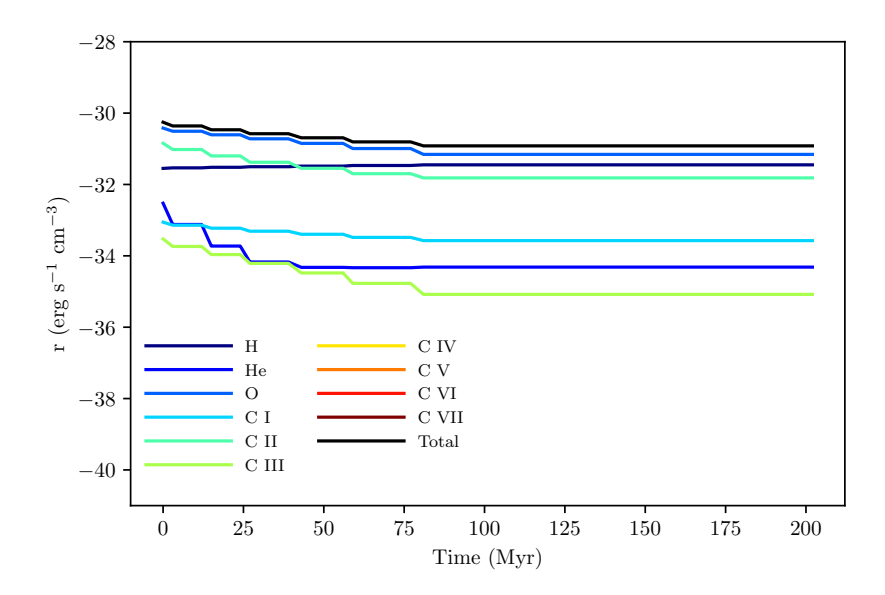


Figure 4.33: Same as Figure 4.27, but for a simulation with an initial temperature of 2×10^4 K. The curves for carbon ions above C III are not shown here because they are too small to fit on the plot.

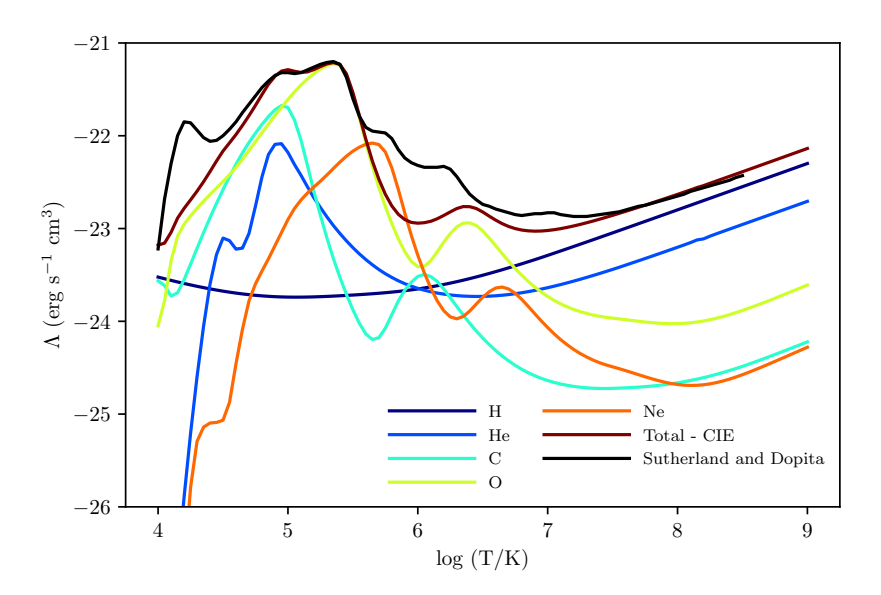


Figure 4.34: Cooling curves for our CIE cooling model and the default FLASH cooling model from Sutherland & Dopita (1993). The black curve is from Sutherland & Dopita (1993) and includes contributions from H, He, and 14 other elements. The dark blue and blue curves are the contributions to our CIE cooling curve from H II and all ions of He, respectively. The aqua, green, and orange lines are the contribution to the CIE cooling curve from all ions of C, O, and Ne, respectively. The maroon line is the combination of the CIE H, He, C, O, and Ne curves.

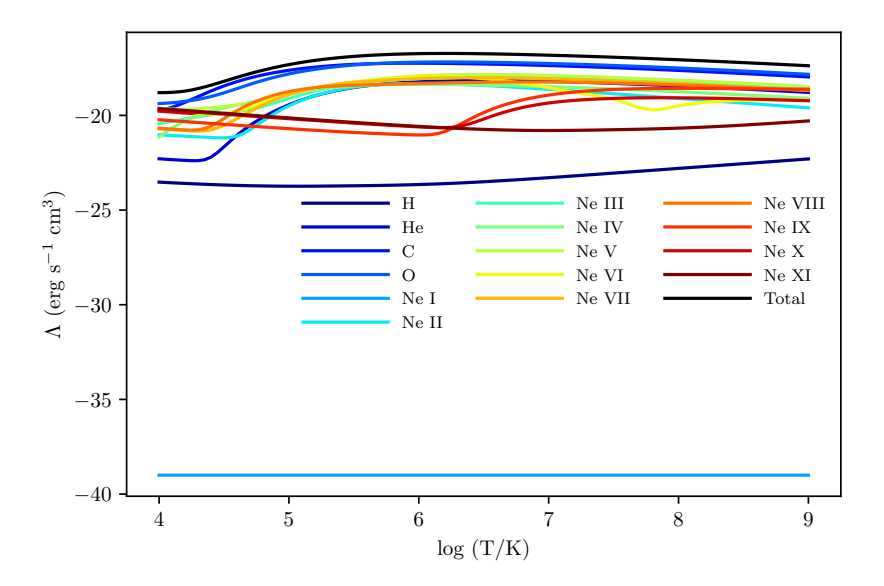


Figure 4.35: Cooling curves for the individual species in our H, He, C, O, and Ne simulations. We combine the contributions of the individual ions for He, C, and O. These curves are shown in different shades of blue. These curves are used in our NEI cooling algorithm.

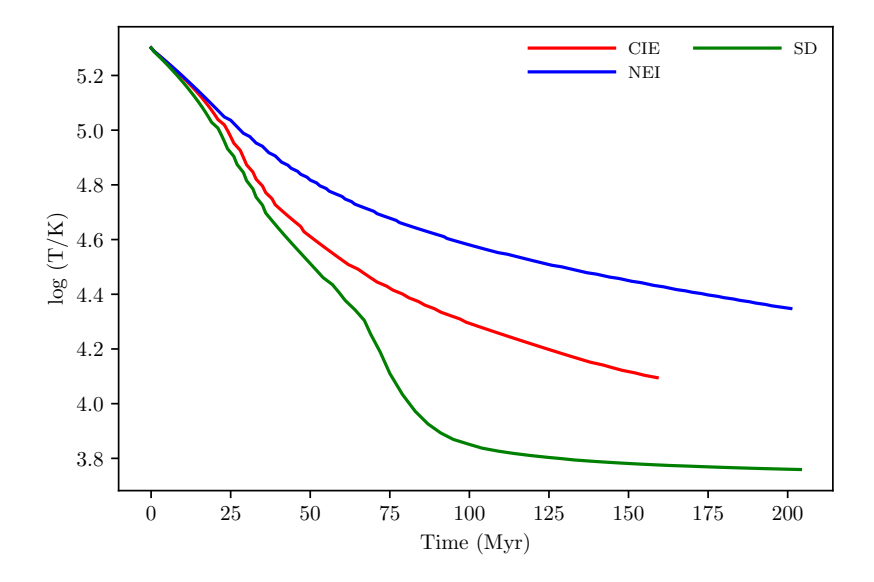


Figure 4.36: Same as Figure 4.3, but our CIE and NEI models shown here include H, He, C, O, and Ne. The Sutherland & Dopita (1993) model is the same as in Figure 4.14.

In the simulation with our NEI cooling model, most of the cooling is due to oxygen. Carbon and hydrogen also produce significant cooling. Of the nitrogen ions, N II contributes the most to the overall

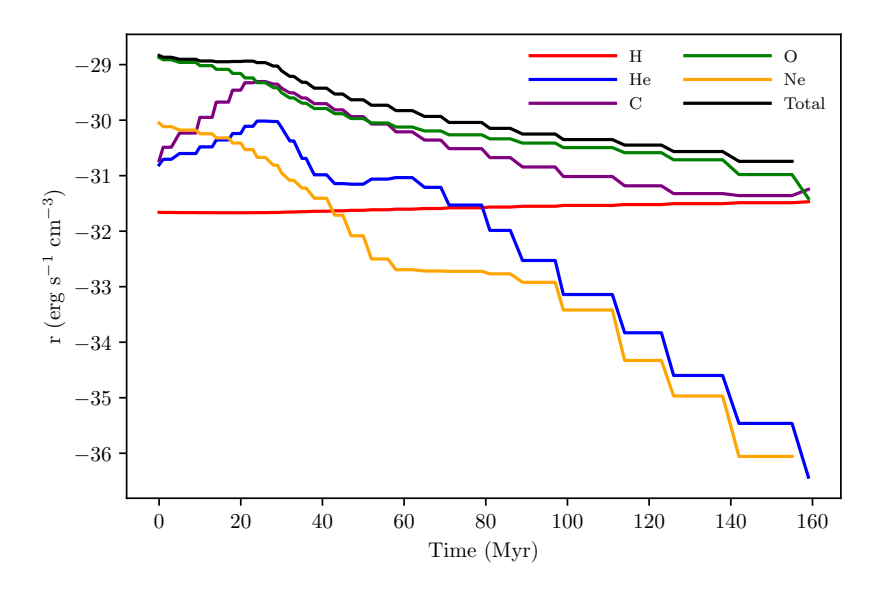


Figure 4.37: Same as Figure 4.4, but for a simulation with H, He, C, O, and Ne.

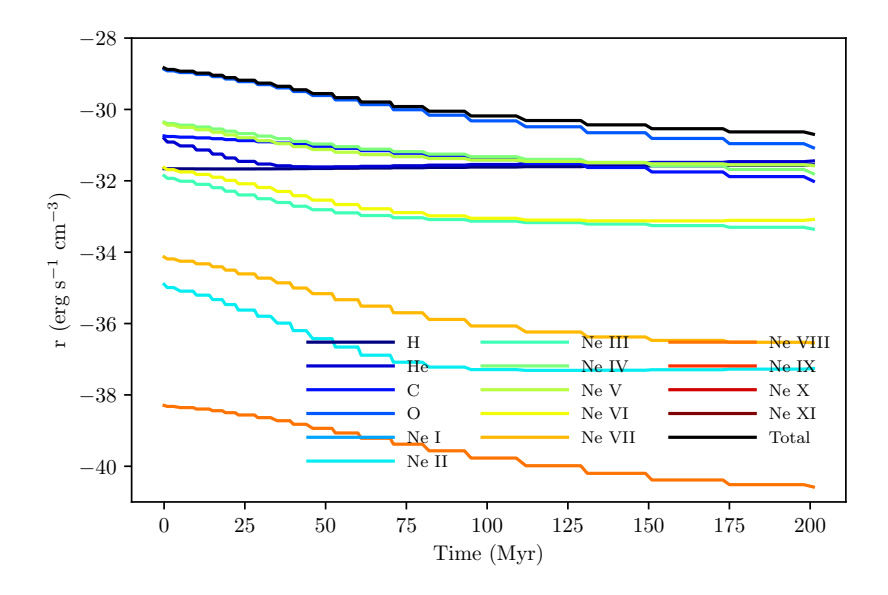


Figure 4.38: Same as Figure 4.5, but for a simulation with H, He, C, O, and Ne. The curves for Ne IX, Ne X, and Ne XI are not shown here because they are too low.

cooling rate (see Figure 4.55). N I and N III also contribute some cooling, although the cooling from N III is several orders of magnitude smaller.

Again, we find the largest differences between our CIE and NEI models in the simulations with an initial gas temperature of 2×10^5 K. The addition of nitrogen does not change the fact that the peak of

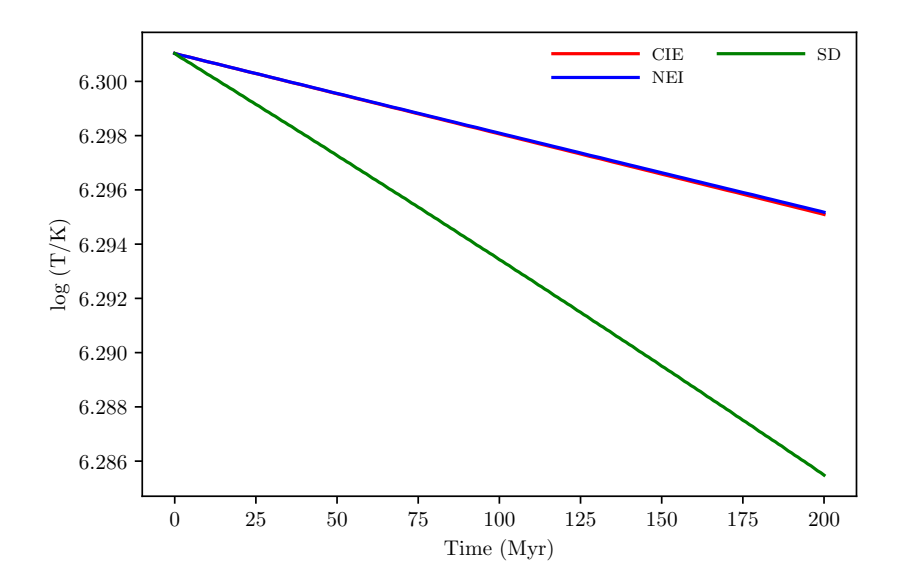


Figure 4.39: Same as Figure 4.36, but for a simulation with an initial temperature of 2×10^6 K.

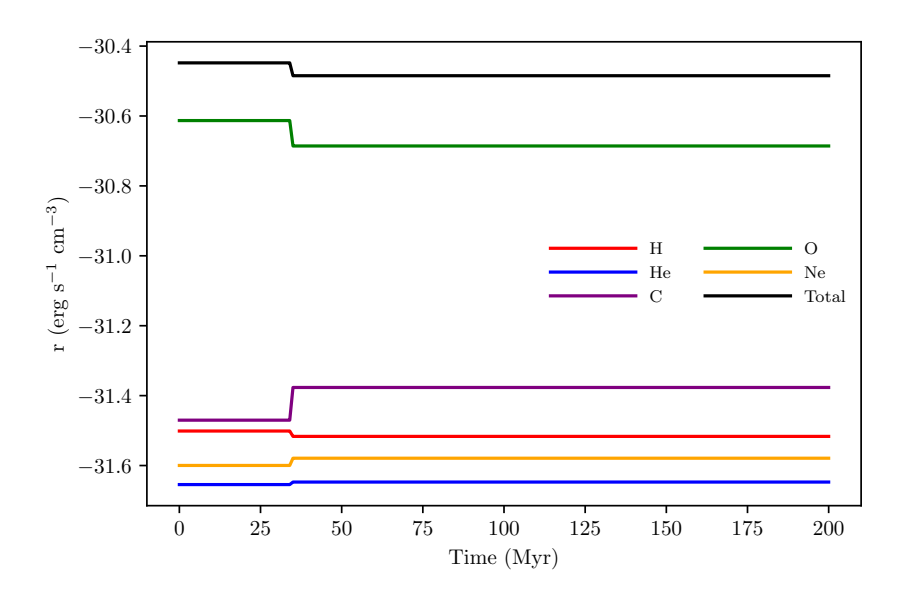


Figure 4.40: Same as Figure 4.37, but for a simulation with an initial temperature of 2×10^6 K.

the cooling curve is in that temperature regime. The cooling caused by nitrogen is smaller than the cooling oxygen, but it can surpass that caused by carbon and neon, especially in the intermediate temperature regime of 2×10^5 K.

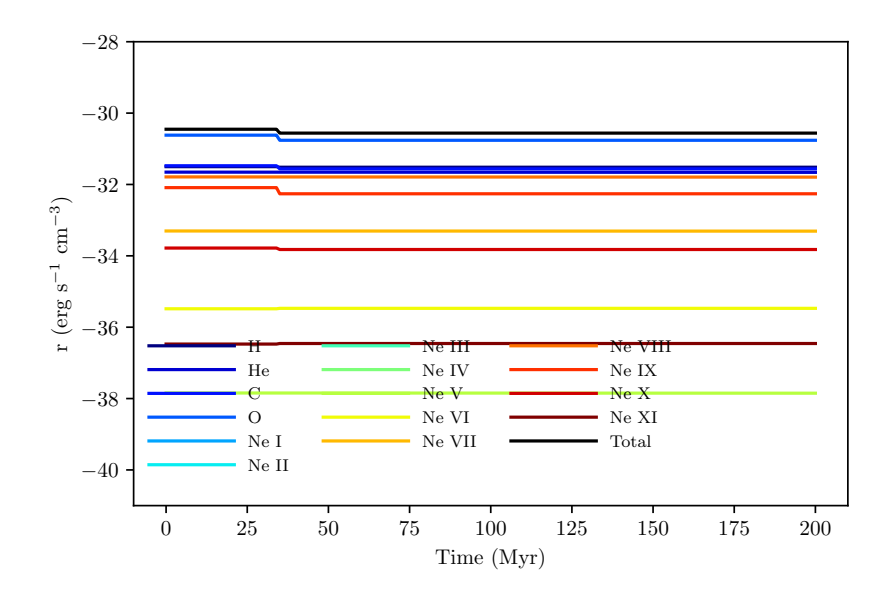


Figure 4.41: Same as Figure 4.38, but for a simulation with an initial temperature of 2×10^6 K. The cooling rates for Ne I through Ne IV are not shown here because their values are too small.

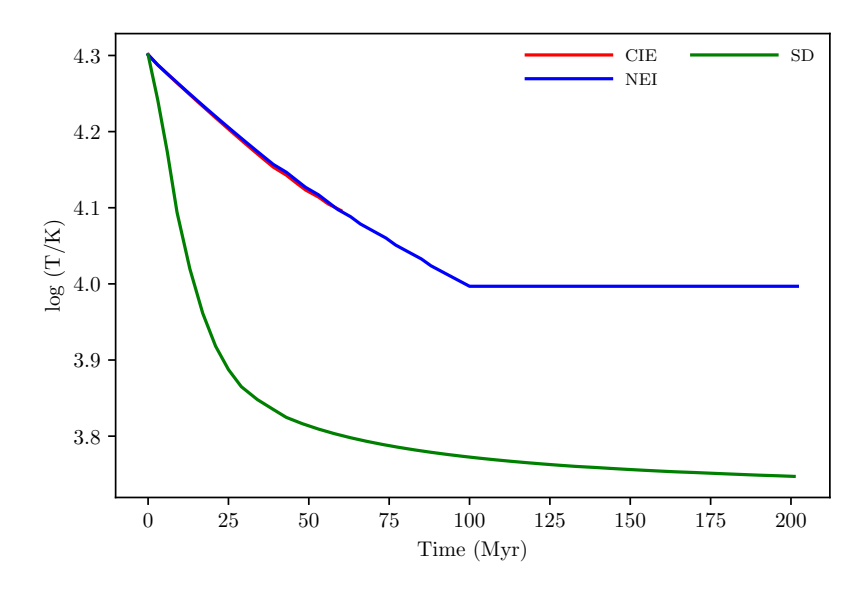


Figure 4.42: Same as Figure 4.36, but for a simulation with an initial temperature of 2×10^4 K.

4.3.2 Effect on High Velocity Clouds

Here, we compare HVC simulations run with the default FLASH radiative cooling algorithm and with our NEI radiative cooling algorithm. Due to the increased computational expense of our NEI cooling

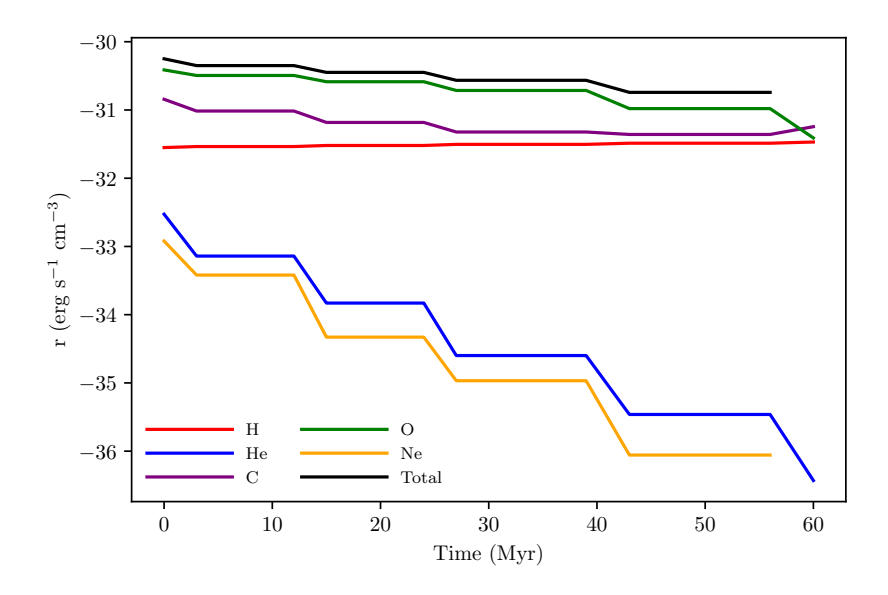


Figure 4.43: Same as Figure 4.37, but for a simulation with an initial temperature of 2×10^4 K.

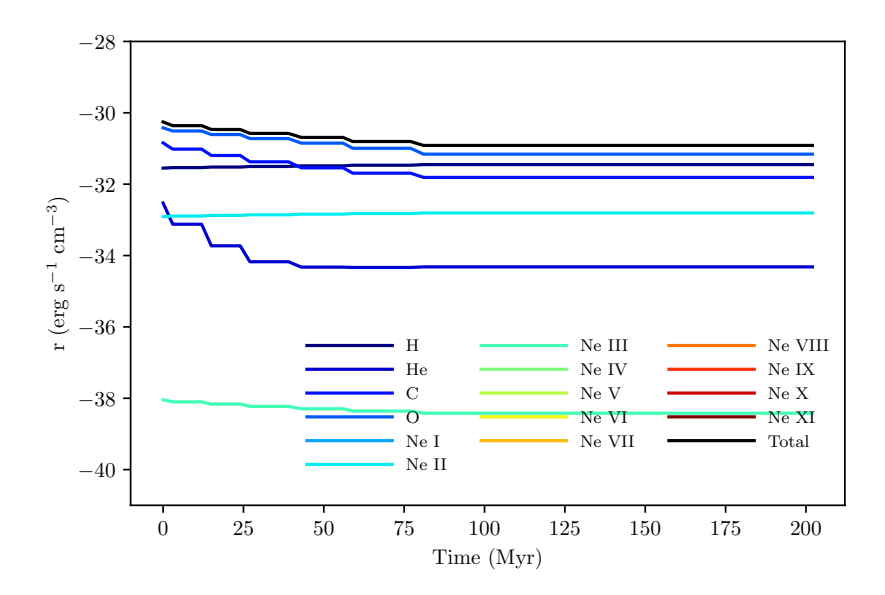


Figure 4.44: Same as Figure 4.38, but for a simulation with an initial temperature of 2×10^4 K. The curves for neon ions above Ne III are not shown here because they are too small to fit on the plot.

algorithm, the simulation using that model was run with a lower maximum refinement level than the simulations described in Goetz et al. (2024). For a more accurate comparison, the simulation using the default FLASH cooling algorithm was rerun with the new refinement. Based on a comparison with the

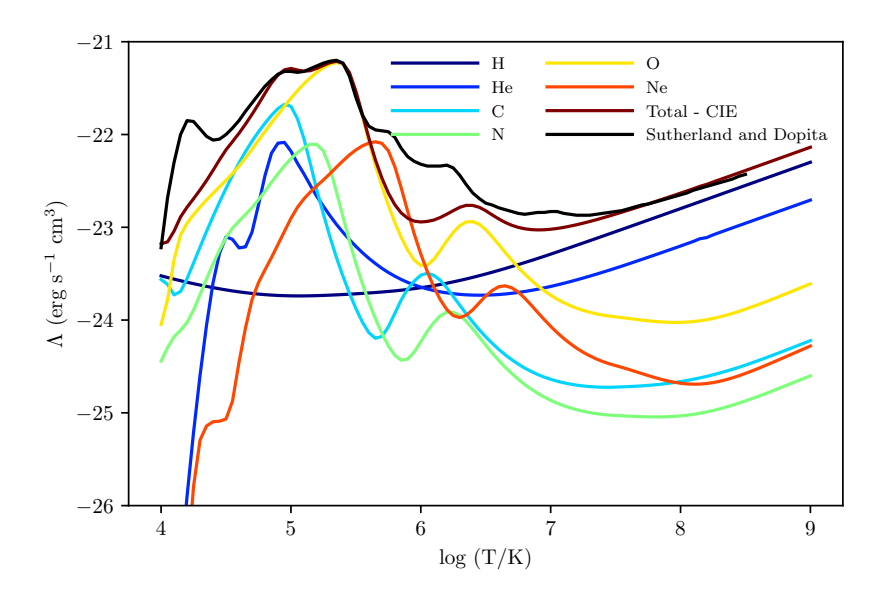


Figure 4.45: Cooling curves for our CIE cooling model and the default FLASH cooling model from Sutherland & Dopita (1993). The black curve is from Sutherland & Dopita (1993) and includes contributions from H, He, and 14 other elements. The dark blue and blue curves are the contributions to our CIE cooling curve from H II and all ions of He, respectively. The aqua, green, yellow, and red lines are the contribution to the CIE cooling curve from all ions of C, N, O, and Ne, respectively. The maroon line is the combination of the CIE H, He, C, N, O, and Ne curves.

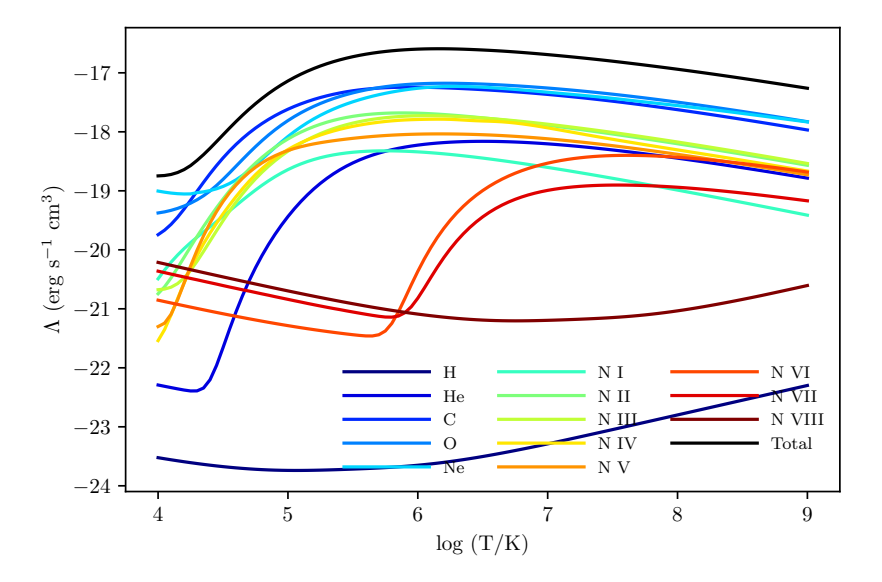


Figure 4.46: Cooling curves for the individual species in our H, He, C, N, O, and Ne simulations. We combine the contributions of the individual ions for He, C, O, and Ne. These curves are shown in different shades of blue. These curves are used in our NEI cooling algorithm.

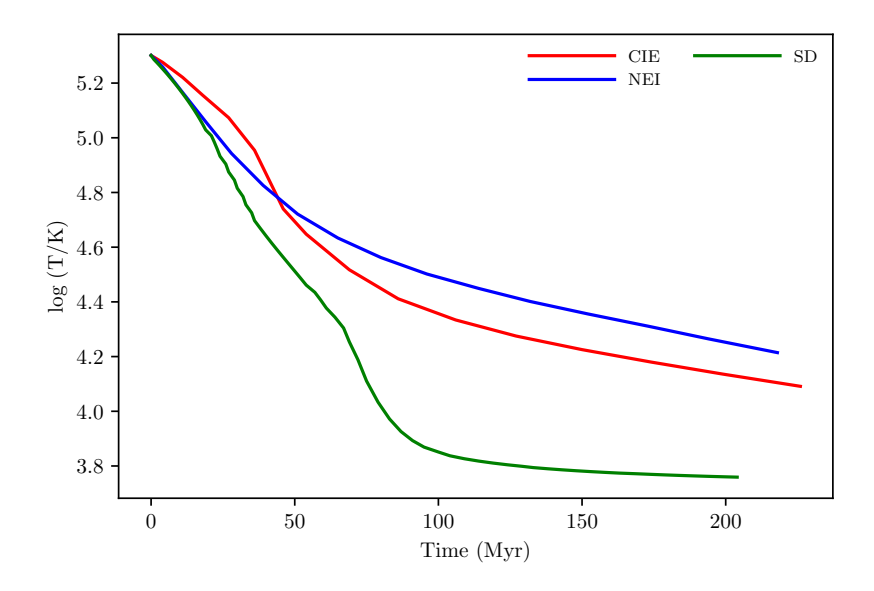


Figure 4.47: Same as Figure 4.3, but our CIE and NEI models shown here include H, He, C, N, O, and Ne. The Sutherland & Dopita (1993) model is the same as in Figure 4.14.

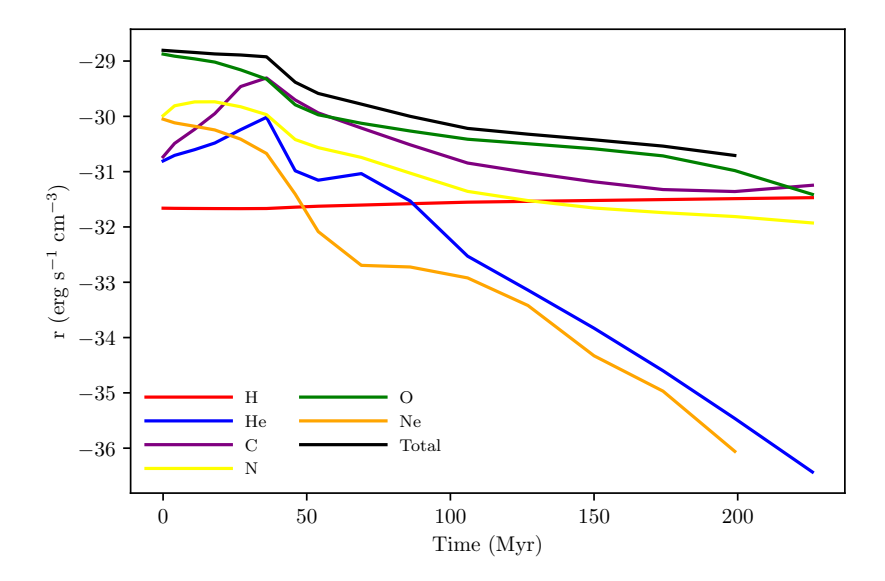


Figure 4.48: Same as Figure 4.4, but for a simulation with H, He, C, N, O, and Ne.

simulations discussed in Goetz et al. (2024), this reduced maximum resolution only has a small effect on the quantities discussed below.

First, we examine the mass-weighted average temperature of the cloud. The evolution of this quantity over time is shown in Figure 4.56. The HVC in the simulation with our NEI model is significantly hotter,

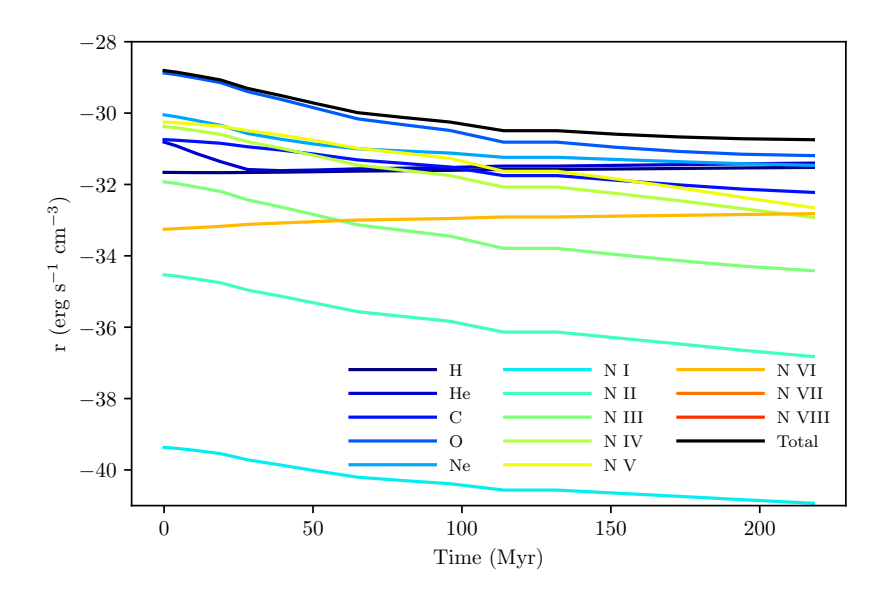


Figure 4.49: Same as Figure 4.5, but for a simulation with H, He, C, N, O, and Ne. The curves for N VII and N VIII are not shown here because they are too low.

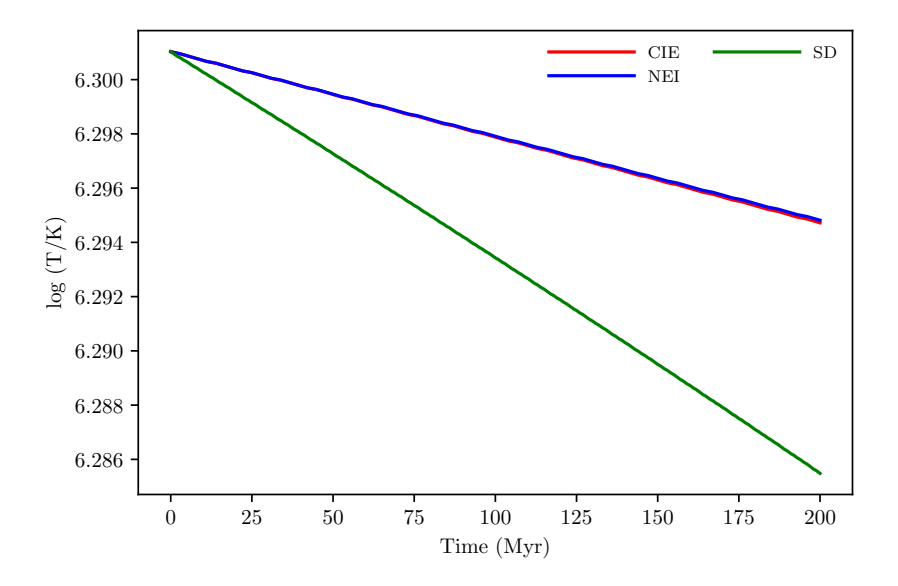


Figure 4.50: Same as Figure 4.6, but our CIE and NEI models shown here include H, He, C, N, O, and Ne. The Sutherland & Dopita (1993) model is the same as in Figure 4.14.

especially in the middle of its evolution. This is because of the reduced cooling resulting from our NEI model compared to the default FLASH radiative cooling algorithm, as discussed in Section 4.3.1. As hot ambient gas is entrained in the HVC, it cannot cool down as quickly because of the reduced cooling rate.

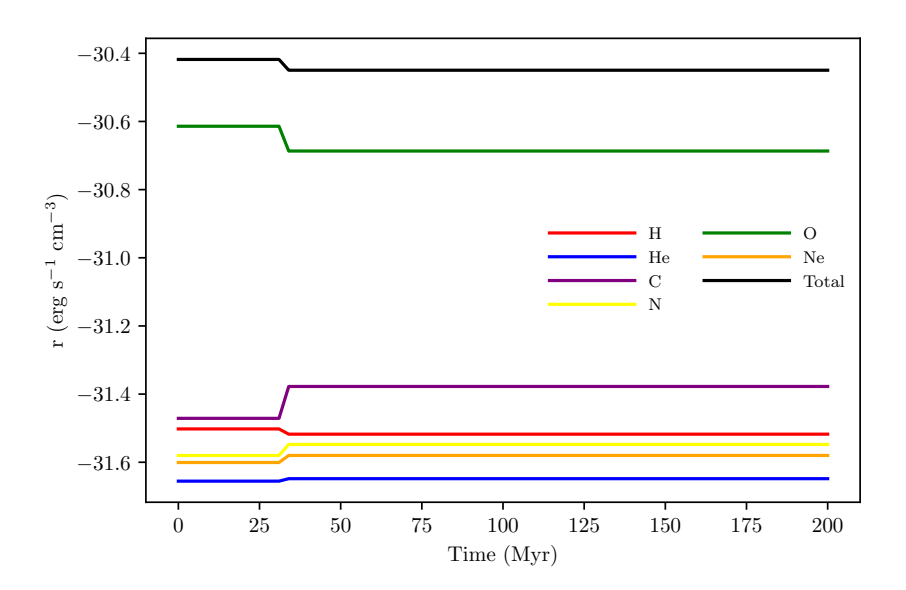


Figure 4.51: Same as Figure 4.7, but for a simulation with H, He, C, N, O, and Ne.

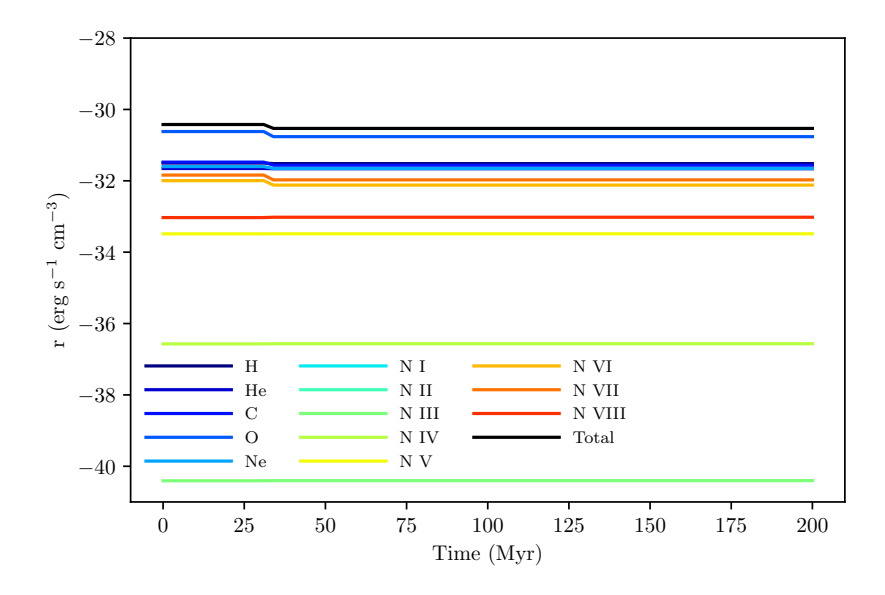


Figure 4.52: Same as Figure 4.8, but for a simulation with H, He, C, N, O, and Ne. The curves for N I and N II are not shown here because they are too low.

The entrained gas begins at a temperature of $1-2\times10^6$ K and is rich in O VII and O VIII. At those temperatures, O VII and O VIII have low cooling rates in our NEI model (see Figure 4.13). The entrained gas is also low density, further reducing the cooling rate. The lower cooling in our NEI model results in an increase in average cloud temperature.

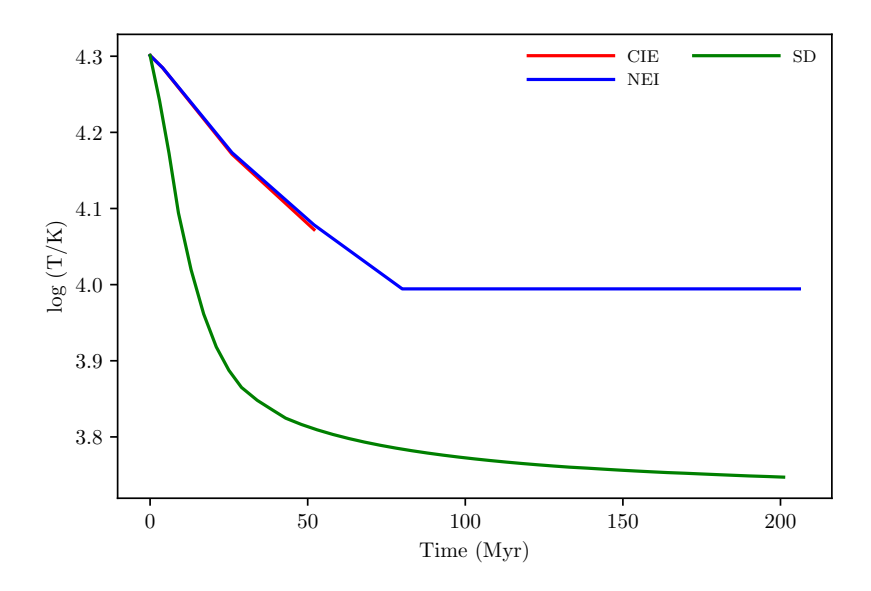


Figure 4.53: Same as Figure 4.9, but our CIE and NEI models shown here include H, He, C, N, O, and Ne. The Sutherland & Dopita (1993) model is the same as in Figure 4.14.

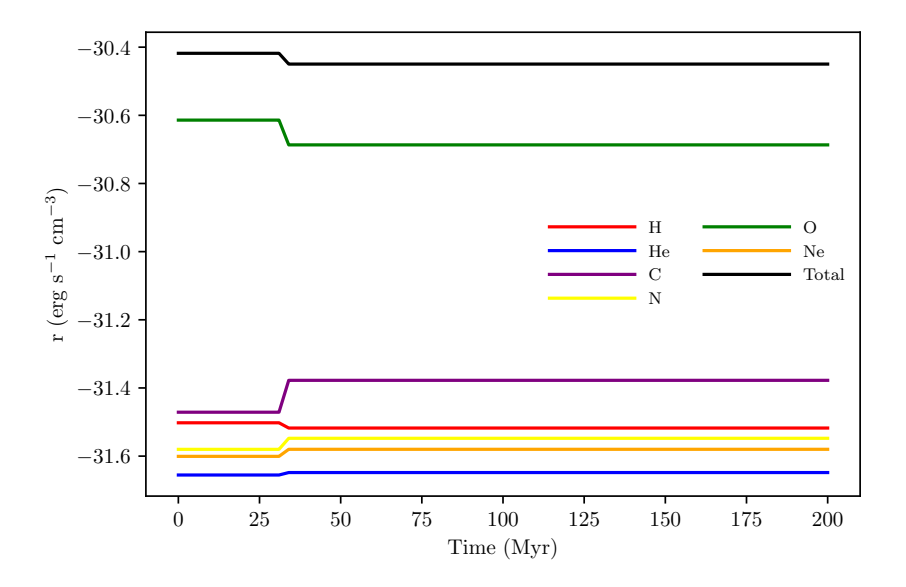


Figure 4.54: Same as Figure 4.10, but for a simulation with H, He, C, N, O, and Ne.

Next, we compare the average ionization fraction of O VI ($f_{\rm OVI}$) across the entire cloud for both simulations. This is shown as a function of time in Figure 4.57. The simulation using our NEI cooling model has significantly less O VI than the simulation using the default FLASH model. This is another consequence of the reduced radiative cooling in our NEI model. Most of the O VI in the HVC comes from

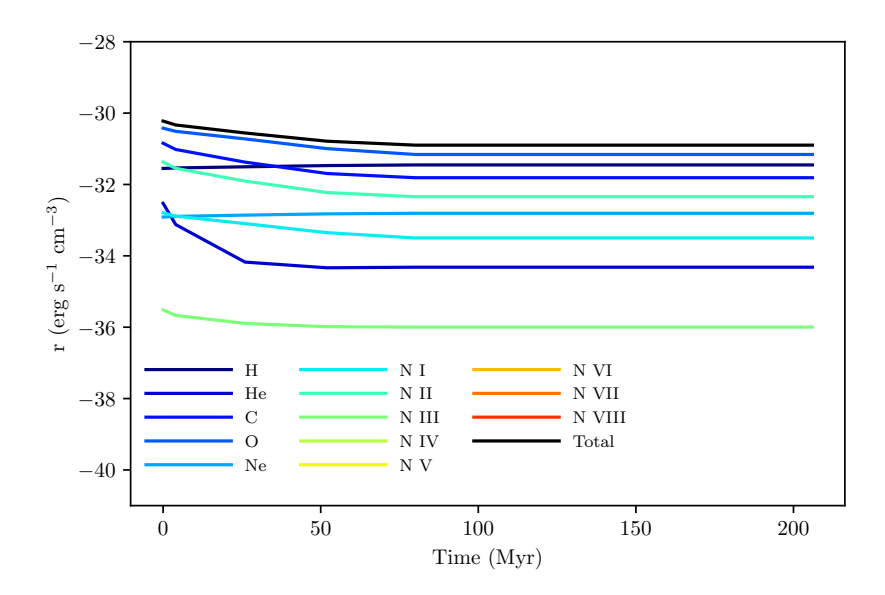


Figure 4.55: Same as Figure 4.11, but for a simulation with H, He, C, N, O, and Ne. The curves for nitrogen ions above N III are not shown here because they are too low.

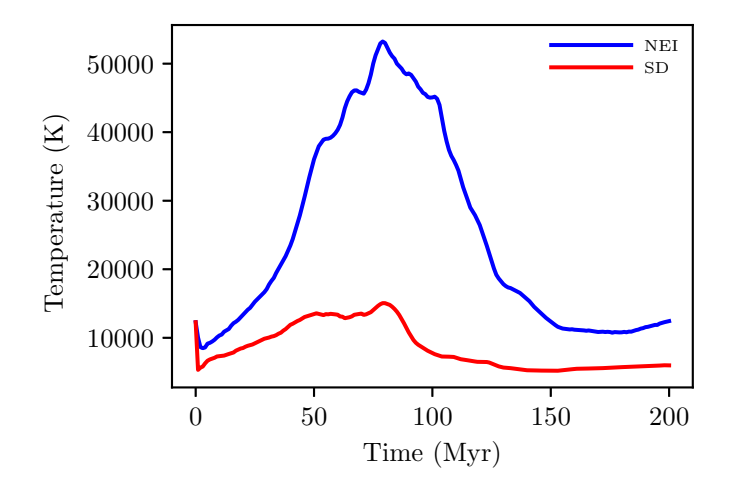


Figure 4.56: Mass-weighted average temperature of the material that is considered to be a part of the HVC, based on the velocity cut described in Section 4.2.2.

hot ambient gas entrained in the cloud. Being rich in high ions such as O VII and O VIII, as the gas cools, those high ions recombine, forming middle ions such as O VI. Due to the reduced cooling occurring in the simulation using our NEI model, cooling and recombination are slower processes, resulting in significantly less O VI.

This has important implications for the masses of HVCs and intergalactic clouds. As discussed in Goetz et al. (2024), the mass of clouds is often calculated using the ionization fraction of ions such as O VI. Since the $f_{\rm OVI}$ is much lower using our NEI model, that would result in significantly more mass in HVCs and other clouds.

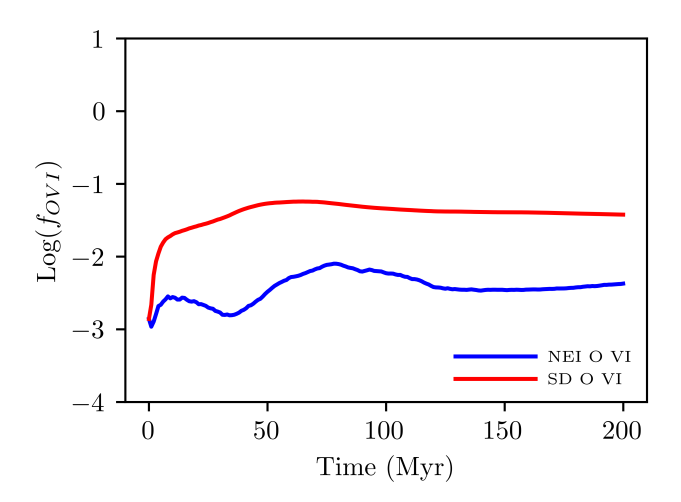


Figure 4.57: Average log O VI ionization fraction as a function of time for both simulations.

Finally, we examine the ratio of H I to O VI. Because FLASH assumes that all of the hydrogen in the simulation is ionized and therefore does not track H I, we calculate the quantity of H I by assuming that its ionization fraction is the same as that of O I. This is a reasonable assumption because H I and O I have similar first ionization potentials (see Goetz et al. (2024) and references therein). This ratio is higher for the simulation using our NEI radiative cooling model. This follows from the discussion of the O VI ionization fraction. Less O VI in the cloud due to a lower cooling rate results in a higher ratio of H I to O VI.

The ratio of H I to O VI is a proxy for the maturation and evolution of the HVC. Due to the reduced cooling in our NEI model, this evolution occurs significantly slower. Goetz et al. (2024) developed a technique, using the ratio of H I to O VI, to identify the epoch in the simulation that best matches observations. Because our H I to O VI ratio is much higher with our NEI cooling model, this implies that the HVCs are much older than thought in Goetz et al. (2024). This resolves an issue with the CIE models in Goetz et al. (2024), which predicted relatively young ages for some clouds.

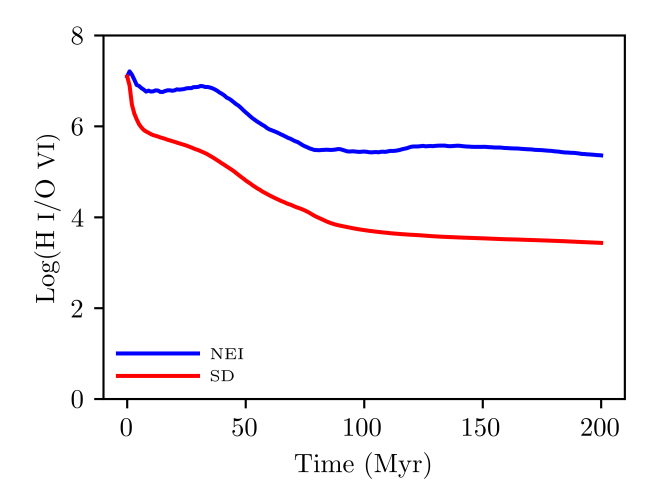


Figure 4.58: Log of the ratio of H I to O VI as a function of time for both simulations.

4.4 Discussion

We find that there can be large differences between NEI and CIE radiative cooling rates, using the algorithms described in this manuscript. These differences depend on the temperature of the gas, as discussed in Section 4.3.1. The differences between our two algorithms are most pronounced in the intermediate temperature regime, i.e., gas with a temperature of $\sim 1-2\times 10^5$ K. This is because in that temperature regime, the total cooling rate per volume of the gas is at its peak. There is also a wider range of ions present in the gas in that temperature regime. Both of these factors increase the likelihood of various ions becoming out of equilibrium, resulting in differences between our NEI and CIE radiative cooling algorithms.

In contrast, in the low temperature regime ($T\sim 2\times 10^4$ K), the gas is already in neutral and low ionization states. Even though significant cooling may still occur at those temperatures, there is less of a chance for ions to be out of equilibrium. This reduces the differences between our NEI and CIE cooling algorithms.

Finally, in the high temperature regime ($T\sim 2\times 10^6$ K), the radiative cooling is significantly reduced. The minimal cooling that occurs at these temperatures similarly reduces the opportunity for non-

equilibrium ionization and recombination to result in ionization fractions different from what would be expected from CIE models. Again, this reduces the difference between our NEI and CIE radiative cooling algorithms.

We also see differences between our two new radiative cooling algorithms and the existing FLASH algorithm. These differences are largely because the existing FLASH algorithm uses a cooling curve from Sutherland & Dopita (1993) that includes the cooling rate contribution from H I. Additionally, with the exception of the table that only includes hydrogen and helium, the other tables from Sutherland & Dopita (1993) include contributions from 16 elements, instead of the three to six (H, He, C, N, O, and Ne) that we include here in our models. The additional elements result in increased radiative cooling, as seen in Section 4.3.1. Finally, another source of differences between our cooling models and the default FLASH model is the source of cooling rates. We get our cooling rates from the latest version of Chianti. There are likely small differences between those rates and those used in Sutherland & Dopita (1993).

We find that the most important elements for radiative cooling, at least in the temperature regimes explored here, are oxygen, carbon, hydrogen, and nitrogen. We find that neon and helium do not contribute much to the overall radiative cooling rate, except in narrow temperature ranges. Therefore, oxygen, carbon, hydrogen, and nitrogen are the most important elements to include in astrophysical simulations.

Using our NEI radiative cooling algorithm instead of the default FLASH radiative cooling algorithm results in substantial changes to the results of HVC simulations. There is significantly less O VI in the simulation using our NEI algorithm. This is due to the reduced cooling rate, slowing the recombination of high ions from the ambient environment entrained in the cloud. As discussed in Goetz et al. (2024), the $f_{\rm OVI}$ and ratio of H I to O VI can be used along with observations to determine the mass of an HVC. Our results here suggest that using a more accurate NEI radiative cooling algorithm results in a smaller simulated $f_{\rm OVI}$ and larger mass per observed O VI ion and therefore a larger cloud mass.

4.5 Author Contributions

The simulations and analysis in this chapter were done by myself. The writing was done by Robin Shelton and myself.

All co-authors agree that the work may be included in this dissertation.

CHAPTER 5

Conclusion

We have explored a number of topics related to HVCs. These topics include the non-equilibrium nature of HVCs, specifically as it relates to the ionization fractions of various ions found in the clouds, as well as the effect on HVCs as they interact with the Galactic halo and disk. Because of the non-equilibrium nature of HVCs, we also developed two new algorithms for implementing radiative cooling in FLASH.

Through the use of hydrodynamic simulations performed with the FLASH simulation software, we have shown that HVCs are significantly out of CIE. The ionization fractions of ions such as O VI in our simulations are much different from those expected from CIE models of static gas. This is because we have considered non-equilibrium ionization and recombination, as well as the dynamic nature of HVCs mixing with the ambient environment.

We have also found O VI at lower temperatures than expected from CIE calculations. This is important because it suggests that the common picture that high ions such as O VI trace hot gas is not exactly accurate. This result has allowed us to reinterpret existing methods of calculating the mass of HVCs. We have introduced a new method for calculating the mass of HVCs which requires minimal observations and provides a firm value instead of a lower bound like previous methods. We have also developed a prescription for observers to follow to utilize our method to determine HVC masses.

We have also examined the result of a collision between an HVC and the Galactic disk. We modeled a baryonic cloud accompanying a dark matter minihalo crashing into the outer regions of the Galactic

disk. We identified the final locations of the original cloud material and found that only a small fraction made it through the disk with the dark matter minihalo. This suggests that HVCs do not survive the passage through the Galactic disk. This has implications for the Smith Cloud, as there is some debate about whether this HVC has previously passed through the disk. Our results indicate that the Smith Cloud is on its first approach to the Galactic disk.

We have also explored the consequences of the collision between an HVC and the Galactic disk. The collision would punch a hole in the disk, the size and longevity of which depend on the initial mass and energy of the HVC and the location of the collision on the disk. We have identified the expected sizes of these holes, which are in line with some existing observations of H I holes in the Galactic disk (and other galaxies' disks).

A collision between an HVC and the Galactic disk also generates a bubble of gas surrounded by a shell. We have determined some characteristics of these shells and bubbles, such as their temperatures, metallicities, and prominent ions that would be expected to be observed in them.

Finally, we have developed two new algorithms that implement radiative cooling in FLASH. We have seen that HVCs can be significantly out of equilibrium. Therefore, we have created an algorithm that takes into account the non-equilibrium nature of HVCs when calculating the total cooling rate in a simulation. Our algorithm uses the actual ionization state populations present in a simulation, as tracked by the non-equilibrium ionization and recombination module in FLASH. This provides a more accurate picture of radiative cooling in an HVC. We compared our algorithm with the existing FLASH radiative cooling module, which determines the total cooling rate based on the CIE ionization fractions at the simulation cell temperature. The existing FLASH radiative cooling module includes the contributions to the overall cooling rate from 16 different elements, many of which are not likely to be tracked in a given FLASH simulation due to computational limitations. Therefore, we have also developed a new radiative cooling algorithm that is based on CIE ionization fractions, but only includes contributions from elements selected to be tracked in the FLASH simulation.

We have compared the results of using each of those three radiative cooling algorithms on simulations of static, isothermal gas. We have found that the differences between the models are largest when the gas

starts in an intermediate temperature regime (2×10^5 K). This is the temperature regime in which the cooling rate is the highest. The enhancement in cooling increases the likelihood that numerous ions will get out of equilibrium, resulting in differences between our NEI and CIE radiative cooling algorithms. Therefore, it is important to consider non-equilibrium effects when doing astrophysical simulations involving that temperature regime.

As an example of this, we have incorporated our new NEI radiative cooling algorithm in our existing HVC simulations and compared the results to the results of similar simulations with the existing FLASH radiative cooling algorithm. We have found substantial differences in numerous cloud quantities predicted from simulations using the two different radiative cooling algorithms. These quantities include the average cloud temperature and the ionization fraction of O VI.

In summary, we have studied HVCs in a multitude of contexts, including their passage through the halo and Galactic disk. We have also implemented new algorithms that can be used to more accurately simulate the dynamic nature of HVCs.

BIBLIOGRAPHY

Alig, C., Hammer, S., Borodatchenkova, N., Dobbs, C. L., & Burkert, A. 2018, , 869, L2, doi: 10.3847/ 2041-8213/aaf1cb

Anders, E., & Grevesse, N. 1989, , 53, 197, doi: 10.1016/0016-7037(89)90286-X

Asplund, M., Grevesse, N., Sauval, A. J., & Scott, P. 2009, , 47, 481, doi: 10.1146/annurev.astro. 46.060407.145222

Bekki, K. 2009, , 398, L36, doi: 10.1111/j.1745-3933.2009.00702.x

Bekki, K., & Chiba, M. 2006, , 637, L97, doi: 10.1086/500304

Bekki, K., Chiba, M., & McClure-Griffiths, N. M. 2008, , 672, L17, doi: 10.1086/526456

Blitz, L., Spergel, D. N., Teuben, P. J., Hartmann, D., & Burton, W. B. 1999, , 514, 818, doi: 10.1086/ 306963

Braun, R., & Burton, W. B. 2000, , 354, 853, doi: 10.48550/arXiv.astro-ph/9912417

Bregman, J. N., & Lloyd-Davies, E. J. 2007, , 669, 990, doi: 10.1086/521321

Burchett, J. N., Tripp, T. M., Prochaska, J. X., et al. 2019, , 877, L20, doi: 10.3847/2041-8213/ab1f7f

Cashman, F. H., Fox, A. J., Wakker, B. P., et al. 2023, 944, 65, doi: 10.3847/1538-4357/acaaa5

Chomiuk, L., & Povich, M. S. 2011, , 142, 197, doi: 10.1088/0004-6256/142/6/197

Collins, J. A., Shull, J. M., & Giroux, M. L. 2007, , 657, 271, doi: 10.1086/510770

Comeron, F., & Torra, J. 1994, , 281, 35

Cox, A. 2000, Allen's astrophysical quantities; 4th ed. (New York, NY: AIP), doi: 10.1007/978-1-4612-1186-0

Del Zanna, G., Dere, K. P., Young, P. R., & Landi, E. 2021, , 909, 38, doi: 10.3847/1538-4357/abd8ce

Dere, K. P., Landi, E., Mason, H. E., Monsignori Fossi, B. C., & Young, P. R. 1997, , 125, 149, doi: 10. 1051/aas:1997368

Drazin, P. G. 2002, Introduction to Hydrodynamic Stability, Cambridge Texts in Applied Mathematics (Cambridge University Press), doi: 10.1017/CB09780511809064

Einasto, J. 1965, Trudy Astrofizicheskogo Instituta Alma-Ata, 5, 87

Ferland, G. J., Chatzikos, M., Guzmán, F., et al. 2017, , 53, 385, doi: 10.48550/arXiv.1705.10877

Field, G. B., & Steigman, G. 1971, , 166, 59, doi: 10.1086/150941

Fox, A. J., Cashman, F. H., Kriss, G. A., et al. 2023, , 946, L48, doi: 10.3847/2041-8213/acc640

Fox, A. J., Richter, P., Wakker, B. P., et al. 2013a, , 772, 110, doi: 10.1088/0004-637X/772/2/110

—. 2013b, The Messenger, 153, 28

Fox, A. J., Savage, B. D., & Wakker, B. P. 2006, 165, 229, doi: 10.1086/504800

Fox, A. J., Wakker, B. P., Savage, B. D., et al. 2005, , 630, 332, doi: 10.1086/431915

Fox, A. J., Wakker, B. P., Smoker, J. V., et al. 2010, , 718, 1046, doi: 10.1088/0004-637X/718/2/1046

Fox, A. J., Lehner, N., Lockman, F. J., et al. 2016, , 816, L11, doi: 10.3847/2041-8205/816/1/L11

Fryxell, B., Olson, K., Ricker, P., et al. 2000, 131, 273, doi: 10.1086/317361

Fukugita, M., Hogan, C. J., & Peebles, P. J. E. 1998, 503, 518, doi: 10.1086/306025

Fukugita, M., & Kawasaki, M. 2003, , 340, L7, doi: 10.1046/j.1365-8711.2003.06507.x

Gaensler, B. M., Madsen, G. J., Chatterjee, S., & Mao, S. A. 2008, , 25, 184, doi: 10.1071/AS08004

Galyardt, J., & Shelton, R. L. 2016, , 816, L18, doi: 10.3847/2041-8205/816/1/L18

Ganguly, R., Sembach, K. R., Tripp, T. M., & Savage, B. D. 2005, , 157, 251, doi: 10.1086/428350

Gnat, O., & Sternberg, A. 2007, , 168, 213, doi: 10.1086/509786

Goetz, E., Wang, C., & Shelton, R. L. 2024, , 960, 66, doi: 10.3847/1538-4357/ad0df7

Gritton, J. A., Shelton, R. L., & Galyardt, J. E. 2017, , 842, 102, doi: 10.3847/1538-4357/aa756d

Gritton, J. A., Shelton, R. L., & Kwak, K. 2014, , 795, 99, doi: 10.1088/0004-637X/795/1/99

Grønnow, A., Tepper-García, T., Bland-Hawthorn, J., & McClure-Griffiths, N. M. 2017, , 845, 69, doi: 10.3847/1538-4357/aa7ed2

Heiles, C. 1984, , 55, 585, doi: 10.1086/190970

Henley, D. B., Gritton, J. A., & Shelton, R. L. 2017, , 837, 82, doi: 10.3847/1538-4357/aa5df7

Henley, D. B., Kwak, K., & Shelton, R. L. 2012, , 753, 58, doi: 10.1088/0004-637X/753/1/58

Henley, D. B., & Shelton, R. L. 2015, , 808, 22, doi: 10.1088/0004-637X/808/1/22

Henley, D. B., Shelton, R. L., Kwak, K., Joung, M. R., & Mac Low, M.-M. 2010, , 723, 935, doi: 10. 1088/0004-637X/723/1/935

Hill, A. S., Haffner, L. M., & Reynolds, R. J. 2009, , 703, 1832, doi: 10.1088/0004-637X/703/2/1832

Holweger, H. 2001, in American Institute of Physics Conference Series, Vol. 598, Joint SOHO/ACE workshop "Solar and Galactic Composition", ed. R. F. Wimmer-Schweingruber, 23–30, doi: 10. 1063/1.1433974

Howk, J. C., Wotta, C. B., Berg, M. A., et al. 2017, , 846, 141, doi: 10.3847/1538-4357/aa87b4

Izumi, N., Kobayashi, N., Yasui, C., et al. 2014, 795, 66, doi: 10.1088/0004-637X/795/1/66

Jansson, R., & Farrar, G. R. 2012a, , 757, 14, doi: 10.1088/0004-637X/757/1/14

—. 2012b, , 761, L11, doi: 10.1088/2041-8205/761/1/L11

Kannan, R., Macciò, A. V., Pasquali, A., Moster, B. P., & Walter, F. 2012, , 746, 10, doi: 10.1088/0004-637X/746/1/10

Kwak, K., Henley, D. B., & Shelton, R. L. 2011, , 739, 30, doi: 10.1088/0004-637X/739/1/30

Kwak, K., & Shelton, R. L. 2010, , 719, 523, doi: 10.1088/0004-637X/719/1/523

Kwak, K., Shelton, R. L., & Henley, D. B. 2015, , 812, 111, doi: 10.1088/0004-637X/812/2/111

Lehner, N., Howk, J. C., Thom, C., et al. 2012, , 424, 2896, doi: 10.1111/j.1365-2966.2012.21428.

Lockman, F. J., Benjamin, R. A., Heroux, A. J., & Langston, G. I. 2008, , 679, L21, doi: 10.1086/588838

Lockman, F. J., Benjamin, R. A., Pichette, N., & Thibodeau, C. 2023, , 943, 55, doi: 10.3847/1538-4357/aca764

McCallum, L., Wood, K., Benjamin, R., et al. 2024, , 530, 2548, doi: 10.1093/mnras/stae988

McClure-Griffiths, N. M., Staveley-Smith, L., Lockman, F. J., et al. 2008, , 673, L143, doi: 10.1086/528683

McMillan, P. J., Petersson, J., Tepper-Garcia, T., et al. 2022, , 516, 4988, doi: 10.1093/mnras/stac2571

Merritt, D., Graham, A. W., Moore, B., Diemand, J., & Terzić, B. 2006, , 132, 2685, doi: 10.1086/508988

Miller, M. J., & Bregman, J. N. 2013, 770, 118, doi: 10.1088/0004-637X/770/2/118

—. 2015, , 800, 14, doi: 10.1088/0004-637X/800/1/14

Miller, M. J., Hodges-Kluck, E. J., & Bregman, J. N. 2016, , 818, 112, doi: 10.3847/0004-637X/818/2/

Mirabel, I. F. 1982, , 256, 120, doi: 10.1086/159888

Morton, D. C. 1991, , 77, 119, doi: 10.1086/191601

Muller, C. A., Oort, J. H., & Raimond, E. 1963, Academie des Sciences Paris Comptes Rendus, 257, 1661

Navarro, J. F., Frenk, C. S., & White, S. D. M. 1996, , 462, 563, doi: 10.1086/177173

Nichols, M., & Bland-Hawthorn, J. 2009, , 707, 1642, doi: 10.1088/0004-637X/707/2/1642

Nichols, M., Mirabal, N., Agertz, O., Lockman, F. J., & Bland-Hawthorn, J. 2014, , 442, 2883, doi: 10. 1093/mnras/stu1028

Oort, J. H. 1966, , 18, 421

Park, G., Koo, B.-C., Kang, J.-h., et al. 2016, , 827, L27, doi: 10.3847/2041-8205/827/2/L27

Plöckinger, S., & Hensler, G. 2012, , 547, A43, doi: 10.1051/0004-6361/201218767

Pokhrel, N. R., Simpson, C. E., & Bagetakos, I. 2020, , 160, 66, doi: 10.3847/1538-3881/ab9bfa

Powell, L. C., Slyz, A., & Devriendt, J. 2011, , 414, 3671, doi: 10.1111/j.1365-2966.2011.18668.x

Putman, M. E., Peek, J. E. G., & Joung, M. R. 2012, , 50, 491, doi: 10.1146/annurev-astro-081811-125612

Ramsøy, M., Slyz, A., Devriendt, J., Laigle, C., & Dubois, Y. 2021, , 502, 351, doi: 10.1093/mnras/stab015

Richter, P. 2017, in Astrophysics and Space Science Library, Vol. 430, Gas Accretion onto Galaxies, ed. A. Fox & R. Davé, 15, doi: 10.1007/978-3-319-52512-9_2

Richter, P., Savage, B. D., Sembach, K. R., & Tripp, T. M. 2006, , 445, 827, doi: 10.1051/0004-6361: 20053636

Richter, P., Sembach, K. R., Wakker, B. P., et al. 2001, , 559, 318, doi: 10.1086/322401

Robitaille, T. P., & Whitney, B. A. 2010, , 710, L11, doi: 10.1088/2041-8205/710/1/L11

Sander, B., & Hensler, G. 2021, , 501, 5330, doi: 10.1093/mnras/staa3952

Savage, B. D., Kim, T. S., Wakker, B. P., et al. 2014, , 212, 8, doi: 10.1088/0067-0049/212/1/8

Sembach, K. R., Howk, J. C., Savage, B. D., & Shull, J. M. 2001, , 121, 992, doi: 10.1086/318777

Sembach, K. R., Tripp, T. M., Savage, B. D., & Richter, P. 2004, , 155, 351, doi: 10.1086/425037

Sembach, K. R., Wakker, B. P., Savage, B. D., et al. 2003, , 146, 165, doi: 10.1086/346231

Shah, M., Bekki, K., Vinsen, K., & Foster, S. 2019, , 482, 4188, doi: 10.1093/mnras/sty2897

Shelton, R. L., Goetz, E. H., & Galyardt, J. E. 2024, , 975, 96, doi: 10.3847/1538-4357/ad75fc

Shull, J. M., Smith, B. D., & Danforth, C. W. 2012, , 759, 23, doi: 10.1088/0004-637X/759/1/23

Shull, J. M., Stevans, M., Danforth, C., et al. 2011, , 739, 105, doi: 10.1088/0004-637X/739/2/105

Simon, J. D., Blitz, L., Cole, A. A., Weinberg, M. D., & Cohen, M. 2006, , 640, 270, doi: 10.1086/

Summers, H. P. 1974, , 169, 663, doi: 10.1093/mnras/169.3.663

Sutherland, R. S., & Dopita, M. A. 1993, , 88, 253, doi: 10.1086/191823

Tenorio-Tagle, G. 1980, , 88, 61

—. 1981, , 94, 338

499914

Tenorio-Tagle, G., Bodenheimer, P., Rozyczka, M., & Franco, J. 1986, , 170, 107

Tenorio-Tagle, G., Franco, J., Bodenheimer, P., & Rozyczka, M. 1987, , 179, 219

Tepper-García, T., & Bland-Hawthorn, J. 2018, , 473, 5514, doi: 10.1093/mnras/stx2680

Teyssier, R. 2002, , 385, 337, doi: 10.1051/0004-6361:20011817

Tripp, T. M. 2022, , 511, 1714, doi: 10.1093/mnras/stac044

Tripp, T. M., & Savage, B. D. 2000, , 542, 42, doi: 10.1086/309506

Tripp, T. M., Savage, B. D., & Jenkins, E. B. 2000, , 534, Li, doi: 10.1086/312644

Tripp, T. M., Sembach, K. R., Bowen, D. V., et al. 2008, , 177, 39, doi: 10.1086/587486

Tripp, T. M., Wakker, B. P., Jenkins, E. B., et al. 2003, , 125, 3122, doi: 10.1086/374995

Troitsky, S. 2017, 468, L36, doi: 10.1093/mnrasl/slx022

Turk, M. J., Smith, B. D., Oishi, J. S., et al. 2011, The Astrophysical Journal Supplement Series, 192, 9, doi: 10.1088/0067-0049/192/1/9

Vorobyov, E. I., & Basu, S. 2005, , 431, 451, doi: 10.1051/0004-6361:20041324

Wagner-Kaiser, R., De Maio, T., Sarajedini, A., & Chakrabarti, S. 2014, , 443, 3260, doi: 10.1093/mnras/stu1327

Wakker, B. P., & van Woerden, H. 1997, , 35, 217, doi: 10.1146/annurev.astro.35.1.217

Wakker, B. P., Howk, J. C., Savage, B. D., et al. 1999, , 402, 388, doi: 10.1038/46498

Wakker, B. P., Savage, B. D., Sembach, K. R., et al. 2003, , 146, 1, doi: 10.1086/346230

Yao, Y., Shull, J. M., & Danforth, C. W. 2011, , 728, L16, doi: 10.1088/2041-8205/728/1/L16